The branching fraction and CP asymmetry of $B^{\pm} \to \psi\pi^{\pm}$ and $B^{\pm} \to \pi^{\pm}\mu^{+}\mu^{-}$ decays

Sophie Redford

St Anne's College, University of Oxford

Thesis submitted for the degree of Doctor of Philosophy at the University of Oxford

Michaelmas Term, 2012

CERN-THESIS-2012-369
18/03/2013

Abstract

Two analyses are performed using data collected by the LHCb experiment during 2011. Both consider decays of charged B mesons reconstructed in the $\pi^{\pm}\mu^{+}\mu^{-}$ final state. Decays involving dimuons provide an experimentally clean signature, even in the high-background environment of the $\sqrt{s} = 7\,\text{TeV}$ proton-proton collisions at the LHC. The first analysis measures the *CP* asymmetry of $B^{\pm} \to \psi\pi^{\pm}$ decays using $0.37\,\text{fb}^{-1}$ of data, where the dimuon decays of two resonances are considered, $J/\psi \to \mu^{+}\mu^{-}$ and $\psi(2S) \to \mu^{+}\mu^{-}$. The branching fraction is measured relative to the Cabibbo favoured $B^{\pm} \to \psi K^{\pm}$ mode. The second analysis uses $1\,\text{fb}^{-1}$ of data to make the first observation of the non-resonant $B^{\pm} \to \pi^{\pm}\mu^{+}\mu^{-}$ decay. The branching fraction is measured relative to that of $B^{\pm} \to K^{\pm}\mu^{+}\mu^{-}$, and measurements of the *CP* asymmetry and the ratio of CKM matrix elements $|V_{td}/V_{ts}|$ are obtained.
The branching fractions of the decays of interest are found to be

$$\begin{aligned}
\mathcal{B}(B^{\pm} \to J/\psi\,\pi^{\pm}) &= (3.88 \pm 0.11 \pm 0.15) \times 10^{-5}\,, \\
\mathcal{B}(B^{\pm} \to \psi(2S)\pi^{\pm}) &= (2.52 \pm 0.26 \pm 0.15) \times 10^{-5} \text{ and} \\
\mathcal{B}(B^{\pm} \to \pi^{\pm}\mu^{+}\mu^{-}) &= (2.48 \pm^{0.57}_{0.52} \pm 0.17) \times 10^{-8}\,,
\end{aligned}$$

where the first uncertainty is related to the statistical size of the sample and the second quantifies systematic effects. The measured *CP* asymmetries in these modes are

$$\begin{aligned}
A_{CP}^{J/\psi\,\pi} &= 0.005 \pm 0.027 \pm 0.011\,, \\
A_{CP}^{\psi(2S)\pi} &= 0.048 \pm 0.090 \pm 0.011 \text{ and} \\
A_{CP}^{\mu\mu\pi} &= -0.045 \pm 0.220 \pm 0.066\,,
\end{aligned}$$

with no evidence of direct *CP* violation seen. The ratio of matrix elements is measured as

$$\frac{|V_{td}|}{|V_{ts}|} = 0.274 \pm^{0.031}_{0.028} \pm 0.008\,,$$

which is in agreement with previous results.

Contents

Acknowledgements

Thanks to Malcolm John, for giving me my first experience of particle physics research at CERN and then encouraging me to apply to the University of Oxford. I would not be where I am today without your superb support and guidance. Thanks for your time and patience in our many discussions, I hope that under your direction I have become a better scientist.

Thanks to all the members of the Oxford LHCb group, for your friendship, support and advice. It has been a pleasure to work with all of you.

Thanks to the LHCb VELO group, especially Paula Collins and Chris Parkes. It has been a privilege to contribute to the detector's operation and performance, thank you for this opportunity. Also thanks for the invite to VERTEX 2010... I may have already attended the nicest conference of my career.

Thanks to Jaap Panman and the LHCb Luminosity group, for introducing me to beam-gas collisions. Our discussions have given me a greater understanding of the LHC, and an appreciation for the collisions on which we depend.

Thanks to Terry Wyatt for keeping in touch and continuing to give advice. I'm fortunate to have you as a mentor.

Thanks to Mark Foster and Martin Griffiths, for supporting my fellowship with the Parliamentary Office of Science and Technology. My three months in London were a fascinating insight into policy and the world of Westminster.

Finally thanks to the STFC, for their financial support throughout my DPhil, including funding my accommodation in Geneva, my summer school in Fermilab and my POST fellowship.

Glossary

Decay angle The angle between the track of a daughter particle and the mother particle's direction of flight, defined in the rest frame of the mother. A daughter particle which has decay angle of 0° has a track which is collinear with the mother particle's track.

$\Delta \log \mathcal{L}(\mathbf{h} - \pi)$ A variable which describes the likely identity of a particle, using information from the RICH and other subdetectors. The default hypothesis is pion. Four hypotheses are compared; kaon, proton, electron and muon.

Impact parameter The perpendicular distance between a track (at its point of closest approach to the primary vertex) and the primary vertex. If the track has originated from the primary vertex, its impact parameter should be small. For tracks coming from secondary vertices, the impact parameter can be larger, although the distribution of events will still peak at an impact parameter of zero.

Impact parameter χ^2 The difference between the χ^2 of the primary vertex reconstructed with and without the considered track.

isMuon A boolean value which is one for particles whose tracks are associated with at least one hit in a number of muon stations, where that number is determined by the momentum of the particle. Particles with no muon chamber hits have an isMuon of zero.

Pointing angle The angle between the momentum vector of a mother particle and the sum of the momentum vectors of the daughter particles. For a perfectly reconstructed decay, this angle is 0°.

Stripping The process of organising recorded data for use in analyses. Stripping can be thought of as a preselection stage, or a series of loose cuts which reduce the total amount of recorded data to those events which are of interest to individual analyses.

Track χ^2/ndf The χ^2 per number of degrees of freedom of a track, obtained by comparing the measured positions of the clusters with the extrapolated positions of the track's intersection with the sensors.

Vertex separation χ^2 The distance χ^2 with which one vertex is separated from another. For instance, a B particle which has flown some way before decaying should have a vertex which is separated from the primary vertex.

Preface

This thesis documents two analyses performed with data collected by the LHCb experiment during 2011. The first analysis studies $B^{\pm} \to \psi\pi^{\pm}$ decays, where $\psi = J/\psi$ or $\psi(2S)$ is reconstructed in the $\mu^+\mu^-$ final state. The second analysis describes the observation of non-resonant $B^{\pm} \to \pi^{\pm}\mu^+\mu^-$ decays. The document is arranged into the following chapters: Chapter 1 provides theoretical motivation for these analyses, describes the observables measured and gives a summary of the state of their determination prior to this work. Chapter 2 provides an overview of the LHCb detector and its performance during 2011. Particular focus is given to the vertex resolution of LHCb, the quality of which provides a measure of the performance of the detector. Both beam-beam and beam-gas vertex resolutions are presented and their application to an absolute luminosity measurement is discussed. Chapter 3 describes the branching fraction and *CP* asymmetry analysis of the resonant $B^{\pm} \to \psi\pi^{\pm}$ decay. Chapter 4 documents the successful search for the rare, non-resonant $B^{\pm} \to \pi^{\pm}\mu^+\mu^-$ decay, the measurement of its *CP* asymmetry and an extraction of the ratio of CKM matrix elements $|V_{td}/V_{ts}|$.

The majority of these analyses are whole work. The vertex resolution analysis documented in Chapter 2 has been presented at conferences and published [1], [2]. The analysis of resonant $B^{\pm} \to \psi\pi^{\pm}$ decays described in Chapter 3 is published [3]. The non-resonant $B^{\pm} \to \pi^{\pm}\mu^+\mu^-$ analysis was done in collaboration for the publication [4]. Chapter 4 is entirely the author's work and as such differs modestly from the LHCb analysis. The final result presented here is compatible with the published result.

Chapter 1

Theoretical background

This chapter introduces some concepts of particle physics theory which motivate this research. The Standard Model (SM) of particles and forces is sketched-out, including some known problems. Specific aspects of the SM, the electroweak interaction, the CKM mechanism and *CP* violation are explored in more detail.

1.1 Fundamental particles and forces

Particle physics is the field of science concerned with understanding the smallest building blocks of nature and the forces which govern their behaviour. The Standard Model (SM) is the theory which currently best describes these particles and forces. A principle idea of the SM is that every fermionic matter particle has an antimatter equivalent, which has the same mass but opposite electric charge. For example, the antiparticle partner of the electron (e^-) is the positron (e^+). The positron was predicted by Dirac [5] and was first observed by Anderson, see Figure 1.1. This discovery predicated the entire field of particle physics which has established experimentally the effective validity of the SM.

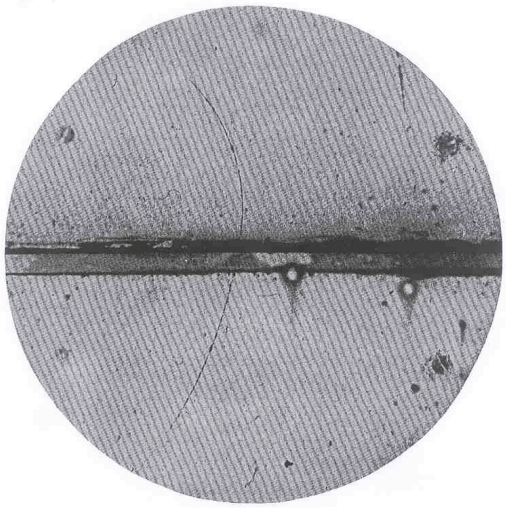

Figure 1.1: Cloud chamber photograph, showing the discovery of the positron by Anderson [6].

At its most basic level, the SM comprises the following fundamental constituents:

- **Quarks**

  There are three generations of quarks:

$$\begin{pmatrix} u \\ d \end{pmatrix}, \quad \begin{pmatrix} c \\ s \end{pmatrix}, \quad \begin{pmatrix} t \\ b \end{pmatrix}, \tag{1.1}$$

  where these letters indicate the quark flavours: up, down, charm, strange, top and bottom. Quarks are fermions with spin $\frac{1}{2}$. They have $+\frac{2}{3}$ or $-\frac{1}{3}$ unit electrical charge. Quarks carry colour charge, and their dominant interaction is via the strong force. Due to colour confinement, quarks can not exist singly on timescales larger than 1 fs and combine into groups of two or three to form colourless mesons and baryons. Quarks are generically denoted q.

- **Leptons**

  The leptons are also arranged into three generations:

$$\begin{pmatrix} e \\ \nu_e \end{pmatrix}, \quad \begin{pmatrix} \mu \\ \nu_\mu \end{pmatrix}, \quad \begin{pmatrix} \tau \\ \nu_\tau \end{pmatrix}. \tag{1.2}$$

  The electron (e), muon (μ) and tau particle (τ) are collectively denoted ℓ. They carry ± 1 unit of electric charge, and interact via the electromagnetic and weak forces. The

neutrinos (ν_ℓ) are electrically neutral, meaning they interact via the weak force only. Leptons are fermions, but unlike quarks they do not carry colour charge.

- **Gauge bosons**

  Gauge bosons are the force carriers which mediate the three forces described by the SM. They have integer spin. Photons (γ) mediate the electromagnetic force between electromagnetically charged particles. They are massless and electrically neutral. The $W^{\pm}$ and Z^0 bosons mediate the weak interaction, which affects all quarks and leptons. Finally, eight gluons (g) mediate the strong force between the quarks. Gluons are massless and electrically neutral, but carry colour charge and so self-interact.

- **Higgs boson**

  The Higgs boson is a massive particle which has spin 0. Interaction with the Higgs boson gives other fundamental particles their mass. A candidate Higgs boson particle was observed at the LHC with a mass of $125\,\mathrm{GeV}/c^2$ [7] [8], although the spin and other properties of this particle must be measured in many production and decay modes before its identity is confirmed.

When forces can be described by the same theory, they are said to be 'unified'. The electromagnetic force is the result of Maxwell's unified description of the electric and magnetic forces [9]. Glashow [10], Weinberg [11], and Salam [12] proved that the electromagnetic force can be unified with the weak force in electroweak theory. Unification of QCD, the theory that describes the strong force, and the electroweak theory remains a distant hope.

The SM has been extremely successful in describing the behaviour of particles in experiments. Furthermore charm, bottom and top quarks, the $W^{\pm}$ and Z^0 bosons, not to mention the Higgs boson, were all proposed before their experimental discovery.

1.2 The state of the Universe

Despite its success, it is acknowledged that the SM cannot be a complete description of the Universe due to its failure to describe all physical phenomena and its dependency on an

apparently arbitrary parameter set. It misses the gravitational force, which is the weakest of the forces but which dominates the behaviour of the Universe at large scales due to its accumulating strength. As there is no 'negative gravity', nothing shields this purely attractive force. Detecting a wave-like nature of gravity would be the first step to developing a quantised description of gravity. An analysis using a worldwide network of kilometre-scale interferometers recently placed a limit on the rate of transient gravitational wave bursts of 1.3 events per year, after observing no significant effect during 207 days of data taking [13].

Various astronomical observations are at odds with predictions of the SM. Measurements of galactic rotation curves [14] and the gravitational lensing of galactic clusters [15] indicate there is much more matter in the Universe than can be detected with electromagnetic radiation. The ΛCDM model of the Universe postulates Cold Dark Matter (CDM) particles, which are weakly interacting so as to explain their hither-to lack of detection. Dark matter is thought to make up 22% the mass of the Universe, compared with 4% which is accounted for by the baryonic matter and electromagnetic radiation of the SM. Attempts to detect dark matter directly have so far been inconclusive and somewhat controversial. The DAMA/LIBRA collaborations have observed the annual modulation of a dark matter 'wind' over a 13 year period with 8.6σ significance [16], but other experiments cannot reproduce the result. The CDMS II experiment observed three dark matter candidates, claiming 11% chance of a background fluctuation, although their background rejection is questioned [17].

Another astronomical observation which challenges the SM involves measurements of Type 1a supernovae, which show that the expansion of the Universe is accelerating [18]. Something unknown must be driving this acceleration. One possibility is a 'vacuum energy' or cosmological constant, which is the Λ of ΛCDM. The nature of this 'dark energy' is entirely unknown, but analysis of the cosmic microwave background suggests that the geometry of space is flat and therefore the total mass-energy of the Universe must equal a critical density. From this, it is calculated that dark energy contributes $\sim 74\%$ of the mass-energy of the Universe [19].

A further issue of the SM is that it does not describe enough *CP* violation to account for the amount of matter in the Universe. The inflationary model of the Universe predicts that

the Big Bang created matter and antimatter in equal amount. Without *CP* violation, this would have led to the total annihilation of matter and antimatter as the Universe cooled. Sakharov set out the three conditions which must have held in the early Universe for an imbalance to have arisen [20]:

- Baryon number violation, which is not explained within the SM and has not been observed by experiment.

- *C* and *CP* symmetry violation. The *CP* violation in the SM is many orders of magnitude away from being able to explain the matter dominance across the observable Universe [21].

- Interactions occurring out of thermal equilibrium. This ensures that any imbalance does not equalise back as it would in a state of equilibrium.

In addition to the cosmological inconsistencies, the SM is known to have theoretical limitations. The most pressing concern is the Hierarchy problem, or why the Higgs self-coupling does not drive its mass to the Planck scale. A supersymmetric (SUSY) extension to the SM resolves this difficulty by postulating that existing bosons have fermion partners and vice versa [22]. If the symmetry were exact, the partners would have equal mass, which is not observed. Therefore the symmetry must be broken, and given that the Higgs is at the weak scale, some SUSY particles should have masses below $1\,\mathrm{TeV}/c^2$. The Hierarchy problem is resolved by the fermionic partner of the Higgs, the Higgsino, which cancels out the quantum corrections up to the Planck scale. However, there is currently no experimental evidence for SUSY despite many searches at the LHC [23], [24].

A further advantage of SUSY is that it presents a possible Dark Matter particle. R-parity is a conservation law which prevents a single SUSY particle from decaying into only SM particles. This avoids SUSY predicting the decay of the proton [25], which is observed to be a stable particle with lifetime $> 2 \times 10^{29}$ years (90% CL) [26]. A consequence of R-parity is that the lightest SUSY particle is unable to decay to lighter SM particles, and thus becomes a stable particle and a Dark Matter candidate [27].

1.3 Development of the weak interaction

The necessity of a weak nuclear interaction was long apparent because of radioactive β decay. This process involves changing the flavour of a quark within the nucleus of an atom, which is only possible by the weak interaction. Yukawa postulated that if the bosons mediating this interaction were massive, then the range of the force would be inversely proportional to their mass [28]. This naturally makes the force 'weak'. Furthermore, as the mass difference between a proton and neutron is small, β decay involves a virtual (off mass shell) $W^{\pm}$ boson which reduces the probability of the process occurring.

The weak force is the only force described by the SM which violates P symmetry. (Symmetries are summarised in Appendix A.) It was initially taken for granted that the weak force would conserve parity, as the other forces did. The idea of P violation in weak decays was first proposed by Lee and Yang to solve the '$\tau - \theta$' problem [29]. The τ and θ were two particles, with identical mass and lifetime but which decayed to two final states of opposite parity. The decay $\tau \rightarrow \pi\pi\pi$ has parity -1, whereas $\theta \rightarrow \pi\pi$ has parity $+1$. Lee and Yang's suggestion was that if parity was not conserved, these two particles could in fact be the same. Parity violation in weak decays was verified experimentally by Wu in an experiment studying β decay in ultra-cold cobalt-60 [30], and simultaneously by Lederman working with polarised muons [31].

These experiments used the property that P inversion does not alter the direction of a particle's spin. As angular momentum, spin is defined as the cross product of a space vector and a momentum vector, $\vec{L} = \vec{r} \times \vec{p}$. Applying parity transformation $\mathcal{P}(\vec{r} \times \vec{p}) = -\vec{r} \times -\vec{p} = \vec{r} \times \vec{p}$ and the direction of spin is unchanged. Therefore, finding a process which produces a spatially asymmetric distribution with respect to the direction of spin shows that the interaction is not symmetric under parity inversion (changing parity changes probability, even though the spin is unchanged). In the cobalt-60 experiment, a magnetic field was used to align the directions of spin of the cold nuclei. Wu found that the β rays (electrons) were emitted in a preferred direction, thus violating parity. Inverting the magnetic field reversed the spin alignment, and also the preferred direction (see Figure 1.2(a)).

Lederman used a cyclotron to test parity conservation in weak decays. The cyclotron

produced pions from proton-proton collisions, and the positive pions were selected by a magnetic field. These decayed in flight to muons: $\pi^+ \rightarrow \mu^+\nu_\mu$. The muons were stopped in a carbon target, where a second magnetic field caused them to precess. The precessing muons decay: $\mu^+ \rightarrow e^+\nu_e\bar{\nu}_\mu$, from which the positron is detected at a fixed angle with respect to the incident muon beam. Lederman found that the positron intensity depends on the magnetic field strength (see Figure 1.2(b)) and hence the precession frequency; i.e the positron emission has a preferred direction with respect to the spin of the muon. This non-zero polarisation proved parity violation in the weak decay of the pion and in the decay of the muon.

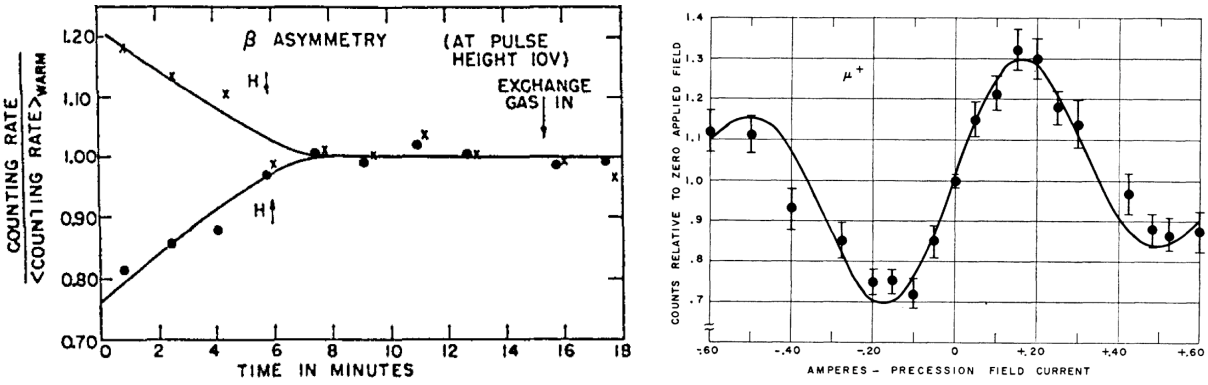

(a) (b)

Figure 1.2: a) β emission in cobalt-60 decays shows a preferred direction with respect to a polarising field pointing up or down. Over time temperature rises and thermal excitations overcome the polarisation of the decaying nuclei. Reprinted figure with permission from [30]. b) Asymmetry in the direction of positrons emitted from decaying polarised muons, showing count for various B fields. Reprinted figure with permission from [31].

Glashow [10], Weinberg [11] and Salam [12] unified the electromagnetic and weak forces into the electroweak theory. This describes how the weak $W^\pm$ and Z^0 bosons couple only to left-handed matter states (meaning that right-handed neutrinos, if they exist, have no SM couplings). Such coupling to only left-handed states explains the maximal violation of parity in weak decays.

Thus far, only charged weak processes have been discussed. A weak neutral current was predicted as a consequence of electroweak unification, and a neutral boson was postulated to mediate it. Weak neutral currents were discovered by the Gargamelle bubble chamber at

CERN, by detecting the isolated electron recoiling from the interaction with an incoming muon neutrino, $\bar{\nu_\mu} e^- \rightarrow \bar{\nu_\mu} e^-$ [32] (the use of a muon neutrino beam is critical as the electron may then only feel a neutral current). Weak neutral currents were also seen by detecting hadrons produced by neutral particles, without an accompanying muon or electron [33]. Both these observations indicate neutrinos can exert an electrically neutral force.

The $W^\pm$ and Z^0 bosons were produced directly for the first time at the SPS collider, and their decay detected by the UA1 and UA2 experiments [34] [35] [36] [37]. Their masses are now measured as $M_{Z^0} = 91.1876 \pm 0.0021\,\mathrm{GeV}/c^2$, $M_{W^\pm} = 80.385 \pm 0.015\,\mathrm{GeV}/c^2$ [38].

In addition to P violation, charged weak decays of quarks also exhibit some CP violation; the only source of CP violation present in the SM. CP violation was first seen in neutral kaon decays by Cronin and Fitch [39]. In their experiment, K_2^0 mesons were produced at the Brookhaven AGS. The neutral beam was achieved by using a magnetic field to remove charged particles, and a lead shield to remove γ rays. It was expected that the K_2^0 state was a pure $CP-$ state, and would decay into $\pi^+\pi^-\pi^0$, as opposed to the K_1^0 state, which being a $CP+$ state decays to $\pi^+\pi^-$. As the triple-pion decay is only just possible energetically, it is long-lived so at the end of a long decay tube one expects to have a pure K_2^0 beam. The experiment detected the charged pions and calculated the angle θ between the vector sum of their two momenta and the K_2^0 beam. This angle is zero for two body decays, and in general not zero for three body decays. A peak of events was discovered with $\theta = 0$, leading to the conclusion that the K_2^0 mesons had decayed into two pions, violating CP symmetry. The long lived neutral kaon is therefore not a pure eigenstate of CP and was renamed the K_L^0.

1.4 *CP* violation in the SM Lagrangian

CP violation is only observed in processes involving the charged weak interaction of some hadrons. It has never been seen in leptons, nor in any electromagnetic or strong interaction[1], nor even via the neutral weak current. One of the great successes of the SM is that CP violation naturally arises in the SM Lagrangian as it describes the action of *massive* left-

[1]Despite no CP violation having been observed in strong decays, there is no known reason for QCD to conserve CP symmetry. This apparent fine-tuning is known as the strong CP problem.

handed fermions coupling to the *charged* gauge field. This mechanism is summarised in this section to elucidate the fundamental importance that the study of (quark) flavour physics and *CP* violation holds. This summary has three parts. First the SM Lagrangian of the electroweak interaction on the left-handed fermion doublets is defined. Then the Higgs mechanism is used to relate the [physical] mass eigenstates to the electroweak interaction basis. Finally, it is noted that if the fermions have mass, an arbitrary rotation matrix arises in the theory. This rotation matrix 'connects' quarks of different generation and, assuming it is non-trivial, germinates the rich pattern of inter-quark phenomenon that is classified as flavour physics. For a more thorough treatment see [40], [41] or [42].

Leaving QCD to one side, the SM Lagrangian can be divided into three parts:

$$\mathcal{L}_{SM} = \mathcal{L}_{kinematic} + \mathcal{L}_{Higgs} + \mathcal{L}_{Yukawa}\,. \tag{1.3}$$

The kinematic term describes the interaction of the spinor fields ψ (the three fermion generations shown in Eqs. 1.1 and 1.2) with the gauge bosons, the Higgs term describes the Higgs scalar field and potential, and the Yukawa term describes the interaction between the Higgs and the fermions.

The dynamics of the spinor fields ψ is given by:

$$\mathcal{L}_{kinematic} = i\bar{\psi}(\partial^{\mu}\gamma_{\mu})\psi\,. \tag{1.4}$$

Within the spinors ψ the representations for the quarks can be denoted [41]:

$$Q^{I}_{Li}(2)\,, \quad u^{I}_{Ri}(1)\,, \quad d^{I}_{Ri}(1)\,, \tag{1.5}$$

where I shows that interaction (flavour) eigenstates are used, not mass eigenstates. The left handed quarks Q^{I}_{Li} are doublets of $SU(2)_L$. q^{I}_{Ri} are the right handed singlets ($q = u, d$). Lepton representations have been omitted. The index $i \in \{1, 2, 3\}$ runs over the quark generations.

To maintain gauge invariance, the partial derivative in Equation 1.4 is replaced with a

covariant derivative appropriate for the electroweak interaction of left handed quarks [42]:

$$\partial^\mu \rightarrow D^\mu = \partial^\mu + igW_b^\mu T_b + ig'B^\mu Y \,. \tag{1.6}$$

Here W_b^μ are the three weak interaction bosons and B^μ is the single weak hypercharge boson[2]. T_b are the $SU(2)_L$ generators (2×2 Pauli matrices) and Y are the $U(1)_Y$ charges.

Remembering that the focus is on the charged weak interaction, the hypercharge field is dropped as it only forms part of the γ and Z^0 fields. This leaves the weak interaction on the left handed quarks:

$$\mathcal{L}_{kinematic,weak}(Q_L) = i\overline{Q_{Li}^I}\gamma_\mu igW_b^\mu T_b Q_{Li}^I \,. \tag{1.7}$$

The $SU(2)_L$ quark doublet can be decomposed into its component quarks:

$$Q_{Li}^I = \begin{pmatrix} u \\ d \end{pmatrix}_{Li}^I \,, \tag{1.8}$$

and T_b can be replaced with the Pauli matrices $\sigma_b/2$ such that:

$$\begin{aligned} W_b^\mu T_b &= \frac{1}{2} W_b^\mu \sigma_b \\ &= \frac{1}{2}\left[W_1^\mu \begin{pmatrix} 0 & 1 \\ 1 & 0 \end{pmatrix} + W_2^\mu \begin{pmatrix} 0 & -i \\ i & 0 \end{pmatrix} + W_3^\mu \begin{pmatrix} 1 & 0 \\ 0 & -1 \end{pmatrix} \right] \\ &= \frac{1}{2} \begin{pmatrix} W_3^\mu & W_1^\mu - iW_2^\mu \\ W_1^\mu + iW_2^\mu & -W_3^\mu \end{pmatrix} . \end{aligned} \tag{1.9}$$

Then:

$$\mathcal{L}_{kinematic,weak}(Q_L) = -\overline{\begin{pmatrix} u & d \end{pmatrix}_{Li}^I} \gamma_\mu g \frac{1}{2} \begin{pmatrix} W_3^\mu & W_1^\mu - iW_2^\mu \\ W_1^\mu + iW_2^\mu & -W_3^\mu \end{pmatrix} \begin{pmatrix} u \\ d \end{pmatrix}_{Li}^I . \tag{1.10}$$

[2]Weak hypercharge is a conserved quantum number defined as $Y_W = 2(Q - T_3)$, where Q is the electric charge and T_3 the third component of weak isospin.

So:

$$\mathcal{L}_{kinematic,cc}(Q_L) = -\frac{g}{2}\overline{u^I_{Li}}\gamma_\mu(W^\mu_1 - iW^\mu_2)d^I_{Li} - \frac{g}{2}\overline{d^I_{Li}}\gamma_\mu(W^\mu_1 + iW^\mu_2)u^I_{Li}\,, \tag{1.11}$$

where the terms involving W^μ_3 have been omitted, again just for clarity, as they combine with the weak hypercharge boson B^μ to form the neutral Z^0 boson and photon. The mass eigenstates of the charged $W^{\pm\mu}$ bosons, defined as $W^{\pm\mu} = \frac{1}{\sqrt{2}}(W^\mu_1 \mp iW^\mu_2)$, are now apparent. The kinetic term associated with the weak charged current becomes:

$$\mathcal{L}_{kinetic,cc} = -\frac{g}{\sqrt{2}}\overline{u^I_{Li}}\gamma_\mu W^{+\mu}d^I_{Li} - \frac{g}{\sqrt{2}}\overline{d^I_{Li}}\gamma_\mu W^{-\mu}u^I_{Li}\,. \tag{1.12}$$

To move towards observables of the Lagrangian, this expression needs rewriting in terms of the fermion mass eigenstates rather than the (weak) interaction eigenstates. The masses of the fermions generated by the Yukawa couplings between the Higgs and fermion fields are described by the third term in Equation 1.3:

$$\mathcal{L}_{Yukawa} = -Y_{ij}\overline{\psi_{Li}}\phi\psi_{Rj} + hc\,, \tag{1.13}$$

where *hc* means Hermitian conjugate. There is a single scalar representation, ϕ, called the Higgs field [41]. The quark representations shown in Equation 1.5 are used again, so that the quarks' Yukawa interactions are given by:

$$\mathcal{L}^{quarks}_{Yukawa} = -Y^d_{ij}\overline{Q^I_{Li}}\phi d^I_{Rj} - Y^u_{ij}\overline{Q^I_{Li}}\tilde{\phi}u^I_{Rj} + hc\,. \tag{1.14}$$

The matrices Y^d_{ij} and Y^u_{ij} are arbitrary complex matrices which operate in flavour space, giving rise to the couplings between different families. The scalar assumes a vacuum expectation value [43]:

$$\phi(x) = \begin{pmatrix}\phi^+\\ \phi^0\end{pmatrix} = \frac{1}{\sqrt{2}}\begin{pmatrix}0\\ v + h(x)\end{pmatrix}\,, \tag{1.15}$$

which generates the down-type quarks' masses. Up-type quarks' masses are generated by

the modified Higgs doublet [40]:

$$\tilde{\phi} = i\sigma_2\phi^* = \begin{pmatrix} \overline{\phi^0} \\ -\phi^- \end{pmatrix} = \frac{1}{\sqrt{2}} \begin{pmatrix} v + h(x) \\ 0 \end{pmatrix} . \tag{1.16}$$

Inserting the decomposed quark and scalar representations into Equation 1.14 gives rise to the mass terms:

$$\begin{aligned} \mathcal{L}^{quarks}_{Yukawa} &= -Y^d_{ij}\overline{\begin{pmatrix} u & d \end{pmatrix}^I_{Li}} \frac{1}{\sqrt{2}} \begin{pmatrix} 0 \\ v + h(x) \end{pmatrix} d^I_{Rj} - Y^u_{ij}\overline{\begin{pmatrix} u & d \end{pmatrix}^I_{Li}} \frac{1}{\sqrt{2}} \begin{pmatrix} v + h(x) \\ 0 \end{pmatrix} u^I_{Rj} + hc \\ &= -Y^d_{ij}\overline{d^I_{Li}} \frac{v}{\sqrt{2}} d^I_{Rj} - Y^u_{ij}\overline{u^I_{Li}} \frac{v}{\sqrt{2}} u^I_{Rj} + hc + \text{interaction terms} \\ &= -M^d_{ij}\overline{d^I_{Li}} d^I_{Rj} - M^u_{ij}\overline{u^I_{Li}} u^I_{Rj} + hc + \text{interaction terms} , \end{aligned} \tag{1.17}$$

where $M^q_{ij} = \frac{v}{\sqrt{2}} Y^q_{ij}$, $q = u, d$.

To obtain the mass terms, the matrices M^q must be diagonalised. Unitary matrices V^q_L and V^q_R can be defined such that M^q_{diag} are real and diagonal [41]:

$$M^q_{diag} = V^q_L M^q V^{q\dagger}_R . \tag{1.18}$$

The quark mass eigenstates are then defined as:

$$q_{Li} = (V^q_L)_{ij} q^I_{Lj}, \quad q_{Ri} = (V^q_R)_{ij} q^I_{Rj} . \tag{1.19}$$

The quarks' weak interaction (flavour) and mass eigenstates are now related through the unitary matrices V.

Equation 1.12 can be reexpressed in terms of the quarks' mass eigenstates (instead of their flavour eigenstates) by substituting the definitions in Equation 1.19:

$$\mathcal{L}_{kinetic,cc}(Q_L) = -\frac{g}{\sqrt{2}} \overline{u_{Li}} (V^u_L V^{d\dagger}_L)_{ij} \gamma_\mu W^{+\mu} d_{Lj} - \frac{g}{\sqrt{2}} \overline{d_{Li}} (V^d_L V^{u\dagger}_L)_{ij} \gamma_\mu W^{-\mu} u_{Lj} , \tag{1.20}$$

where:

$$(V_L^u V_L^{d\dagger})_{ij} = V_{CKM}\,. \tag{1.21}$$

The form of the Cabibbo-Kobayashi-Maskawa (CKM) matrix V_{CKM} is not unique, as there is rotational freedom in defining V. By convention, the interaction eigenstates and mass eigenstates of up-type quarks are chosen to be equal. Down-type quarks are then rotated between mass and interaction eigenstates:

$$u_i^I = u_j \tag{1.22}$$

$$d_i^I = V_{CKM} d_j\,, \tag{1.23}$$

and therefore:

$$\begin{pmatrix} d^I \\ s^I \\ b^I \end{pmatrix} = \begin{pmatrix} V_{ud} & V_{us} & V_{ub} \\ V_{cd} & V_{cs} & V_{cb} \\ V_{td} & V_{ts} & V_{tb} \end{pmatrix} \begin{pmatrix} d \\ s \\ b \end{pmatrix}\,. \tag{1.24}$$

So, for example, the transition from a down-type quark to an up-type quark is described by V_{ud} (see Figure 1.3).

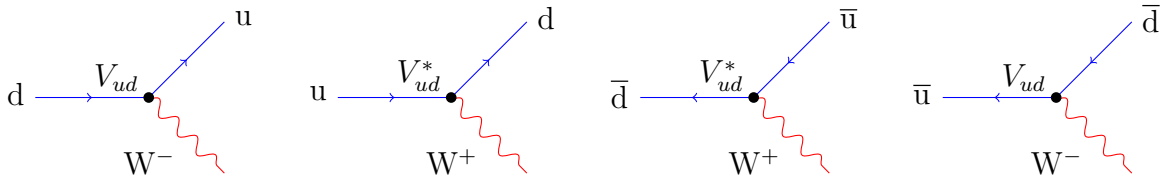

Figure 1.3: The definition of V_{ij} and V_{ij}^*.

A matrix can include as many phases as there are matrix elements. However, in a 2×2 matrix all phases can be removed by rotation. For instance, the Cabibbo angle rotates the 2-generation quark mixing matrix in such a way that no phases remain. In a 3×3 matrix, one phase will remain regardless of rotation. For this reason, the observation of *CP* violation in the SM requires the existence of at least 3 quark generations. The single phase of the CKM matrix is called the Kobayashi-Maskawa phase δ_{KM}. It is the only source of *CP* violation in the quark sector of the SM. Additionally, V_{CKM} is not diagonal, so the $W^{\pm}$ bosons couple

to the quark mass eigenstates of different generations. This is the only source of flavour changing quark interaction in the SM.

1.5 Parameterisation of the CKM matrix

As a 3×3 unitarity matrix, the CKM matrix is parametrised by four parameters, although there is freedom in how these parameters are defined. The CKM matrix parametrisation used by the Particle Data Group consists of three mixing angles $\theta_{12}, \theta_{23}, \theta_{13}$ and a *CP* violating phase δ [38];

$$V_{CKM} = \begin{pmatrix} c_{12}c_{13} & s_{12}c_{13} & s_{13}e^{-i\delta} \\ -s_{12}c_{23} - c_{12}s_{23}s_{13}e^{i\delta} & c_{12}c_{23} - s_{12}s_{23}s_{13}e^{i\delta} & s_{23}c_{13} \\ s_{12}s_{23} - c_{12}c_{23}s_{13}e^{i\delta} & -c_{12}s_{23} - s_{12}c_{23}s_{13}e^{i\delta} & c_{23}c_{13} \end{pmatrix}, \tag{1.25}$$

where $s_{ij} = \sin\theta_{ij}$ and $c_{ij} = \cos\theta_{ij}$. It is known experimentally that $\theta_{12} = 13.04°, \theta_{13} = 0.2°, \theta_{23} = 2.38°$. Therefore $s_{13} \ll s_{23} \ll s_{12} \ll 1$, and $c_{13} \approx c_{23} \approx c_{12} \approx 1$.

The magnitudes of the CKM matrix elements are determined in a global fit [38] to be:

$$V_{CKM} = \begin{pmatrix} 0.97428 & 0.2253 & 0.00347 \\ 0.2252 & 0.97345 & 0.0410 \\ 0.00862 & 0.0403 & 0.999152 \end{pmatrix} \pm \begin{pmatrix} 0.00015 & 0.0007 & 0.00016 \\ 0.0007 & 0.00016 & 0.0011 \\ 0.00026 & 0.0011 & 0.000045 \end{pmatrix}. \tag{1.26}$$

Note that the diagonal elements are close to 1, so transitions are most likely within a quark generation. Transitions can change a generation, but this is less likely. This hierarchy prompted Wolfenstein to parametrise the CKM matrix in powers of the Cabibbo angle λ:

$$|V_{CKM}| \sim \begin{pmatrix} 1 & \lambda & \lambda^3 \\ \lambda & 1 & \lambda^2 \\ \lambda^3 & \lambda^2 & 1 \end{pmatrix}, \tag{1.27}$$

with:

$$\lambda = \sin\theta_{12} \tag{1.28}$$

$$A\lambda^2 = \sin\theta_{23} \tag{1.29}$$

$$A\lambda^3(\rho - i\eta) = \sin\theta_{13}e^{i\delta_{13}}\,, \tag{1.30}$$

where A, ρ, η are numbers of order 1. The Wolfenstein parametrisation of the CKM matrix to λ^3 is:

$$V_{CKM} = \begin{pmatrix} 1-\frac{1}{2}\lambda^2 & \lambda & A\lambda^3(\rho - i\eta) \\ -\lambda & 1-\frac{1}{2}\lambda^2 & A\lambda^2 \\ A\lambda^3(1-\rho-i\eta) & -A\lambda^2 & 1 \end{pmatrix} + \delta V\,, \tag{1.31}$$

where the phases in V_{td} and V_{ub} are apparent. The phase in V_{ts} enters at λ^4:

$$\delta V = \begin{pmatrix} -\frac{1}{8}\lambda^4 & 0 & 0 \\ \frac{1}{2}A^2\lambda^5(1-2(\rho+i\eta)) & -\frac{1}{8}\lambda^4(1+4A^2) & 0 \\ \frac{1}{2}A\lambda^5(\rho+i\eta) & \frac{1}{2}A\lambda^4(1-2(\rho+i\eta)) & -\frac{1}{2}A^2\lambda^4 \end{pmatrix} + \mathcal{O}(\lambda^6)\,, \tag{1.32}$$

and other phases enter at the level λ^5. By defining the angles:

$$\beta = \arg\left[-\frac{V_{cd}V_{cb}^*}{V_{td}V_{tb}^*}\right]\,, \quad \gamma = \arg\left[-\frac{V_{ud}V_{ub}^*}{V_{cd}V_{cb}^*}\right]\,, \quad \beta_s = \arg\left[-\frac{V_{ts}V_{tb}^*}{V_{cs}V_{cb}^*}\right]\,, \tag{1.33}$$

the Wolfenstein phase convention can be shown as:

$$V_{CKM} = \begin{pmatrix} |V_{ud}| & |V_{us}| & |V_{ub}|e^{i\gamma} \\ -|V_{cd}| & |V_{cs}| & |V_{cb}| \\ |V_{td}|e^{-i\beta} & -|V_{ts}|e^{i\beta_s} & |V_{tb}| \end{pmatrix} + \mathcal{O}(\lambda^5)\,. \tag{1.34}$$

The complex phases β, β_s, γ therefore quantify the largest *CP* violation present in the CKM matrix.

1.6 How to test for new physics

Searches for physics beyond the SM can take two forms; direct and indirect searches. Direct searches involve trying to create and detect new particles, by colliding partons with sufficient energy to form a particle on mass shell whose decay is reconstructed. The search for the Z' boson at the LHC is an example of a direct search. The general purpose detectors search for this hypothetical particle by reconstructing high energy lepton pairs. A possible Feynman diagram is shown in Figure 1.4. The current mass limit for a Z' is $1.83\,\mathrm{TeV}/c^2$ at 95% confidence level [44].

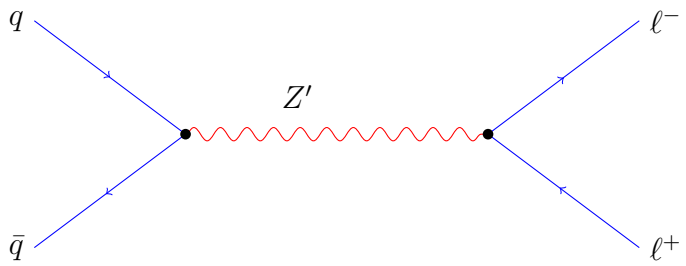

Figure 1.4: Drell-Yan production of the hypothetical Z' boson, which might subsequently decay to two leptons [45].

An alternative, complementary approach is to search for new particles indirectly, taking advantage of Heisenberg's uncertainty principle to detect 'virtual' particles, off mass shell, at energies below those needed to produce a 'real' particle. Virtual particles can exist in loops, where the presence of new particles can affect the amplitude of the process. A good SM example is the first measurement of the oscillation frequency of B^0 mesons (see Figure 1.5) [46], which gave the first indication that the mass of the top quark should be high. It was many years before the top quark mass was confirmed by direct observation at the Tevatron [47] [48].

The indirect approach is used throughout heavy flavour physics, studying the transitions between quark flavours. New physics may be detected by its effect on CP violation in these transitions, or by modifications to the rate at which rare processes occur.

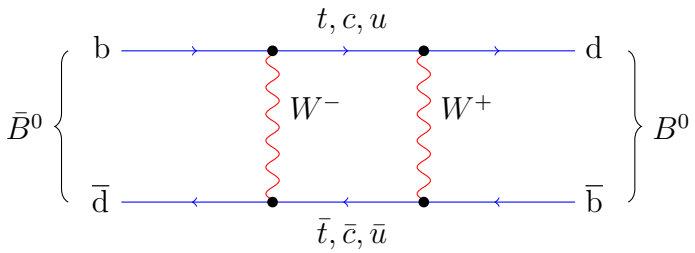

Figure 1.5: B^0 meson mixing. Properties of the top quark running in the loop may be inferred from the oscillation frequency.

1.6.1 *CP* violation

CP violation can be split into three kinds:

- **Direct *CP* violation**

  This occurs as a difference in the decay rates of two *CP* conjugate decays:

  $$\mathcal{B}(B^0 \to f) \neq \mathcal{B}(\bar{B}^0 \to \bar{f})\,. \tag{1.35}$$

  Direct *CP* violation is time independent, in the sense that it occurs at the point of decay. Both neutral and charged B mesons can display direct *CP* violation.

- ***CP* violation in mixing**

  CP violation in mixing occurs when the oscillation from meson to antimeson is different from the reverse oscillation:

  $$\mathrm{Prob}(B^0 \to \bar{B}^0) \neq \mathrm{Prob}(\bar{B}^0 \to B^0)\,. \tag{1.36}$$

  CP violation in mixing occurs during the mixing of neutral states, as was seen in K^0_L decays to *CP*+ final states. It requires that the *CP* eigenstate of the system is not equal to the mass eigenstate. *CP* violation in mixing is time dependent.

- ***CP* violation in interference between a decay with and without mixing**

  CP violation can occur in the interference between a decay with and without mixing. For example: $B^0 \to f$ may interfere with the mixing of $B^0 \to \bar{B}^0 \to f$. This type of *CP*

violation depends on the neutral meson mixing frequency, and so is time dependent. Only neutral mesons may exhibit *CP* violation in interference.

The decays analysed in this thesis are of charged B mesons, so only direct *CP* violation is considered further.

A direct *CP* asymmetry in charged B mesons is defined as:

$$A_{CP} = \frac{\mathcal{B}(B^- \to \bar{f}) - \mathcal{B}(B^+ \to f)}{\mathcal{B}(B^- \to \bar{f}) + \mathcal{B}(B^+ \to f)} \,. \tag{1.37}$$

Direct *CP* violation requires two interfering amplitudes, i.e. two Feynman diagrams for the same initial and final states. These two amplitudes must have different weak and strong phases. For two amplitudes A_1 and A_2 with relative weak phase ϕ and relative strong phase δ, the decay branching ratios are:

$$\begin{aligned} \mathcal{B}(B \to f) &\propto |A_1 + A_2 e^{i\phi} e^{i\delta}|^2 \\ \mathcal{B}(\bar{B} \to \bar{f}) &\propto |A_1 + A_2 e^{-i\phi} e^{i\delta}|^2 \,, \end{aligned} \tag{1.38}$$

where the charge conjugate decay has taken the complex conjugate of the weak phase. Therefore from Equation 1.37:

$$\begin{aligned} A_{CP} &= \frac{|A_1 + A_2 e^{-i\phi} e^{i\delta}|^2 - |A_1 + A_2 e^{i\phi} e^{i\delta}|^2}{|A_1 + A_2 e^{-i\phi} e^{i\delta}|^2 + |A_1 + A_2 e^{i\phi} e^{i\delta}|^2} \\ &= \frac{2A_1 A_2 \sin\phi \sin\delta}{A_1^2 + A_2^2 + 2A_1 A_2 \cos\phi \cos\delta} \,, \end{aligned} \tag{1.39}$$

where Euler's formula $e^{ix} = \cos x + i \sin x$ has been used. For a *CP* asymmetry to exist, neither ϕ nor δ can be 0 or π, and the amplitudes of the two decays must be similar or else the interference with the suppressed amplitude is too small to be observed.

Imagining A_1 to be a tree level process, and A_2 a loop level process between the same initial and final states, it is clear how an alteration of amplitude A_2, or of the relative weak phase ϕ, by new physics could affect the measured *CP* asymmetry.

1.6.2 Flavour changing neutral currents

Flavour changing neutral currents (FCNC) are forbidden at tree level in the SM, and must occur at loop-level. Figure 1.6 shows possible FCNC penguin and box diagrams. From the initial b quark, two FCNC transitions are possible, $b \to s$ or the suppressed $b \to d$ transition. The dilepton final state is chosen as this gives the cleanest signal experimentally. Additionally, the non-resonant dilepton final states can only have occurred through the FCNC transition.

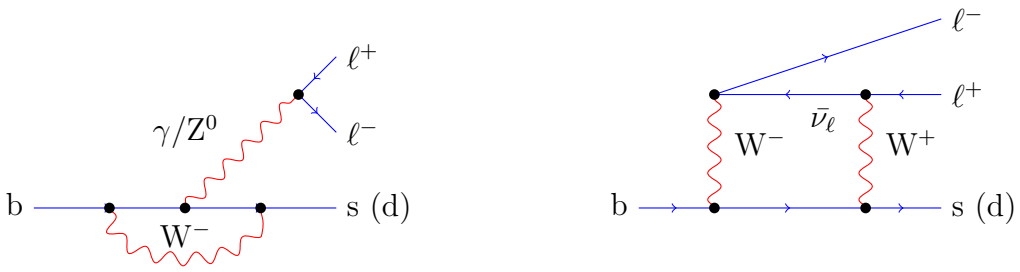

Figure 1.6: Feynman diagrams showing the FCNC transition $b \to q\ell^+\ell^-$, where $q = s, d$. Left: the electromagnetic and Z^0 penguin diagram. Right: the electroweak box diagram.

FCNC decays are a good place to test the SM. These modes are suppressed by $2-3$ orders of magnitude in comparison to the tree-level processes giving the same final states. New physics may enter in the FCNC loop and affect the amplitude and other characteristics of these decays. The $b \to q\ell^+\ell^-$ decay has two leading order contributions: an electroweak penguin and a W^+W^- box diagram (see Figure 1.6). The similar $b \to q\gamma$ decay only proceeds through an electromagnetic penguin (see Figure 1.7). Therefore, comparison between $b \to q\gamma$ and $b \to q\ell^+\ell^-$ processes can potentially yield insight into non-SM effects (e.g. right-handed currents) in the loop.

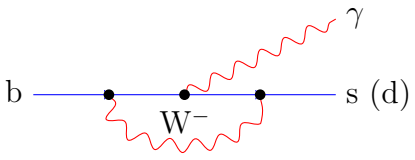

Figure 1.7: Radiative $b \to q\gamma$ decay ($q = s, d$), an electromagnetic penguin decay.

1.7 Exclusive B meson decays to charmonium

Weak $b \to c$ transitions account for the majority of B decays, because the CKM matrix element V_{cb} is large in comparison to V_{ub} and FCNC are rare. The resulting $W^{\pm}$ boson decays to quarks 68% of the time (and to $\ell\nu_\ell$ 32% of the time) [49]. Depending on the topology of the Feynman diagrams, two cases can be described as 'internal' or 'external', see Figure 1.8.

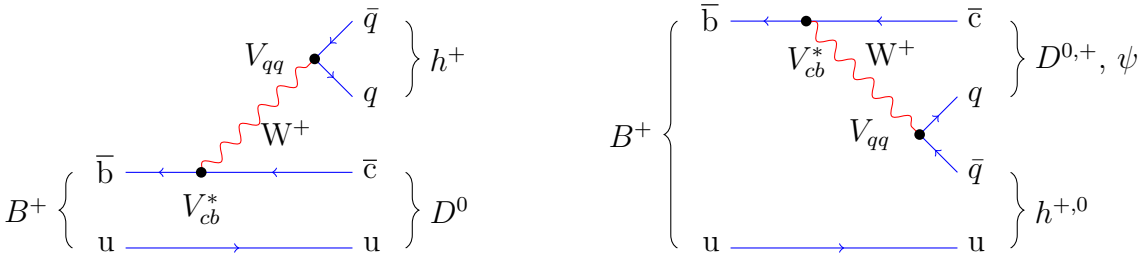

Figure 1.8: Left: External, colour-allowed diagram for $B^{\pm} \to D^0 h^{\pm}$. Right: Internal, colour-suppressed diagram for $B^{\pm} \to X_c h$. This is the only way to get a ψ in the final state at tree level.

For internal decays, the $W^{\pm}$ is restricted in its decay. As the final state mesons must be colour-neutral, the colour of the $W^{\pm}$ decay fragments must match that of the B decay fragments. This reduces the likelihood of the internal decay by a colour factor of $f_{col} \sim 3$, called 'colour-suppression'. This is the only way to produce a ψ resonance from tree level B decays.

Cabibbo suppression can be measured by comparing similar decays which differ by a CKM factor. For example, Figure 1.9 shows $B^{\pm} \to \psi K^{\pm}$ and $B^{\pm} \to \psi \pi^{\pm}$ decays, which differ in the W^+ decay factor V_{cs} and V_{cd}. The expected ratio of branching fractions is $R \sim |V_{cd}|^2/|V_{cs}|^2$. Using values shown in Equation 1.26, one expects $R \sim 5\%$.

By comparing two decays experimentally, a measure of Cabibbo suppression can be made. In the case of $B^{\pm} \to \psi h^{\pm}$ decays, the ratio of branching fractions is defined as:

$$R^{\psi} = \frac{\mathcal{B}(B^{\pm} \to \psi \pi^{\pm})}{\mathcal{B}(B^{\pm} \to \psi K^{\pm})} \,. \tag{1.40}$$

The PDG [49] average for $R^{J/\psi}$ prior to this thesis was $(5.2 \pm 0.4)\%$. This is based on four

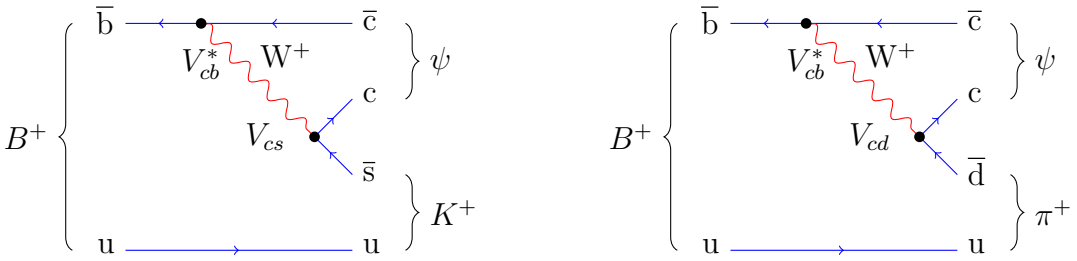

Figure 1.9: $B^\pm \to \psi h^\pm$ decays where $h = K$ (left) and $h = \pi$ (right). The two decays vary in the CKM matrix element at the $W^\pm$ decay vertex.

measurements made by the CDF (Run I and Run II), BABAR and CLEO II collaborations. The BABAR measurement of $R^{J/\psi} = (5.37 \pm 0.45 \pm 0.11)\%$ is the most precise single result [50]. For the $\psi(2S)$ system there is just one result from Belle using 85% of their final dataset, of $R^{\psi(2S)} = (3.99 \pm 0.36 \pm 0.17)\%$ [51].

The ratio of branching fractions has also been measured in neutral B decays [38]:

$$\begin{aligned} \frac{\mathcal{B}(B^0 \to J/\psi\,\pi^0)}{\mathcal{B}(B^0 \to J/\psi\,K^0)} &= \frac{(1.76 \pm 0.16) \times 10^{-5}}{(8.74 \pm 0.32) \times 10^{-4}} \\ &\approx (2.0 \pm 0.2)\%\,. \end{aligned} \tag{1.41}$$

This ratio is lower than the expected 5% due to isospin. Typically $\pi^0 = \frac{u\bar{u}-d\bar{d}}{\sqrt{2}}$, however, combining with the spectator quark (d) restricts the π^0 state and lowers the transition probability by about a factor of 2. The $B^0 \to \psi(2S)\pi^0$ mode has not yet been observed.

The situation for $B \to Dh$ decays is slightly different, as both colour suppressed and allowed diagrams contribute (see Figure 1.8), and cannot be distinguished between in the final state. LHCb recently measured Cabibbo suppression in $B^\pm \to D^0 h^\pm$ decays [52]:

$$\frac{\mathcal{B}(B^\pm \to D^0 K^\pm)}{\mathcal{B}(B^\pm \to D^0 \pi^\pm)} = (7.74 \pm 0.12 \pm 0.19)\%\,. \tag{1.42}$$

In neutral $B \to Dh$ decays [38]:

$$\begin{aligned} \frac{\mathcal{B}(B^0 \to D^\pm K^\mp)}{\mathcal{B}(B^0 \to D^\pm \pi^\mp)} &= \frac{(1.97 \pm 0.21) \times 10^{-4}}{(2.68 \pm 0.13) \times 10^{-3}} \\ &\approx (7.35 \pm 0.86)\%\,. \end{aligned} \tag{1.43}$$

The variation in all these measurements is due to differing hadronic factors. In addition to giving access to the ratio of CKM matrix elements, the ratio of branching fractions R gives information on the variation between the QCD form factors of different light mesons. This can be used as input to models based on the hadronisation factorisation hypothesis [53].

CP asymmetry in $B^{\pm} \to \psi h^{\pm}$ decays is caused by interference between processes involving identical initial and final states. From Equation 1.37, the direct *CP* asymmetry in $B^{\pm} \to \psi h^{\pm}$ decays is defined as:

$$A_{CP}^{\psi h} = \frac{\mathcal{B}(B^- \to \psi h^-) - \mathcal{B}(B^+ \to \psi h^+)}{\mathcal{B}(B^- \to \psi h^-) + \mathcal{B}(B^+ \to \psi h^+)} \,. \tag{1.44}$$

Four contributing processes are considered in Table 1.1. The dominant amplitude in $B^{\pm} \to \psi h^{\pm}$ decays comes from the tree level, colour suppressed $b \to c\bar{c}q$ transition. The penguin diagram for the $b \to c\bar{c}q$ transition is also shown to represent loop level processes (box and penguin). For the Cabibbo-favoured $B^{\pm} \to \psi K^{\pm}$ decay, the tree and penguin amplitudes have a small relative weak phase, so a small A_{CP} is predicted by the SM in this mode. This is confirmed by experiment, the PDG average of $A_{CP}^{J/\psi K}$ is $(0.1 \pm 0.7)\%$ [49]. The *CP* asymmetry in the $\psi(2S)K$ mode, averaged from three measurements by the PDG, is also consistent with zero: $A_{CP}^{\psi(2S)K} = (-2.5 \pm 2.4)\%$.

$B^{\pm} \to \psi\pi^{\pm}$ decays have a significant relative weak phase between tree and penguin diagrams. Considering Equation 1.39, one can hypothesise that the loop level amplitude A_2 is approximately 3% that of the colour suppressed tree level amplitude A_1. In the best case scenario the relative strong phase of the decays will give $\sin\delta = 1$. The relative weak phase $\sin\phi = \sin\beta = 0.36$, as the CKM matrix element under consideration is V_{td} (see Table 1.1). This yields a *CP* asymmetry estimate of:

$$\begin{aligned} A_{CP}^{\psi\pi} &= 2\frac{A_2}{A_1}\sin\delta\sin\phi \\ &= 2 \times 0.03 \times 1 \times 0.36 \\ &= 2\% \,. \end{aligned} \tag{1.45}$$

The interpretation of any charge asymmetry is complicated by long-distance rescattering [54]. Long range rescattering occurs for the transition $B^{\pm} \to i \to \psi h^{\pm}$, where i is an

Feynman diagram	V_{CKM}	ψK	$\psi\pi$	Notes
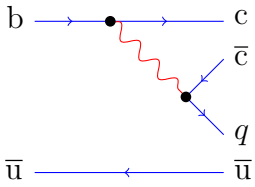	$V_{cb}^* V_{cq}$	$\lambda^2 A_{tree} f_{col}$	$\lambda^3 A_{tree} f_{col}$	Tree level $b \to q\bar{c}c$ transition
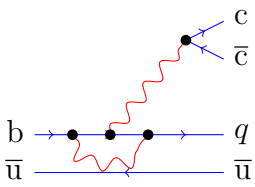	$V_{tb}^* V_{tq}$	$\lambda^2 A_{loop} e^{i\beta_s}$	$\lambda^3 A_{loop} e^{i\beta}$	Penguin level $b \to q\bar{c}c$ transition
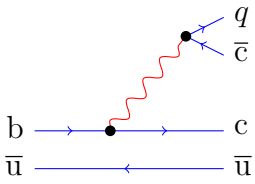	$V_{cb}^* V_{cq}$	$\lambda^2 A_{Rescat}$	$\lambda^3 A_{Rescat}$	Rescattering via $c\bar{c}q$ state.
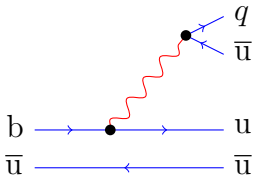	$V_{ub}^* V_{uq}$	$\lambda^4 A_{OZI} e^{i\gamma}$	$\lambda^3 A_{OZI} e^{i\gamma}$	Rescattering via $u\bar{u}q$ state.

Table 1.1: Contributing Feynman diagrams to the $B^\pm \to \psi h^\pm$ decay. λ is the Wolfenstein parameter, β, β_s, γ are CKM angles. $q = d, s$.

intermediate state with quark content $d\bar{u}u\bar{u}$ or $d\bar{c}c\bar{u}$, as shown in Table 1.1. The intermediate quarks rescatter off each other before recombining to the final state, for example, $B^{\pm} \to D^0 D^{\pm} \to J/\psi\pi^{\pm}$. A *CP* asymmetry may occur if there is interference between the tree level amplitude and the amplitude of the rescattered decay [54].

The scattering transition $b \to d\bar{u}u \to \psi d$ is OZI suppressed, as shown in Figure 1.10. Therefore, the contribution of this rescattering process to the *CP* asymmetry is small, 10^{-3}.

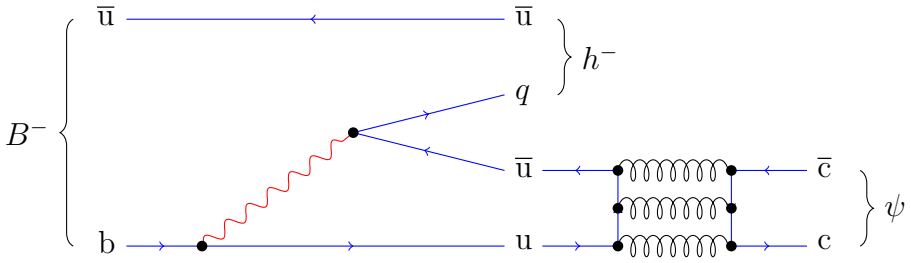

Figure 1.10: Feynman diagram showing OZI suppression in the transition $b \to d\bar{u}u \to d\bar{c}c$.

However, the $b \to d\bar{c}c$ transition is not suppressed. Wolfenstein showed that intermediate states with the same quark content can contribute to the *CP* asymmetry [55]. Detailed calculations suggest that rescattering through this transition could lead to a *CP* asymmetry of up to 1% in the $B^{\pm} \to J/\psi\,\pi^{\pm}$ channel [54].

$A_{CP}^{J/\psi\,\pi}$ has been measured to less than 10% accuracy by both BABAR and DØ though the two results differ by around one standard deviation, see Figure 1.11 [49]. The world average prior to this thesis was $A_{CP}^{J/\psi\,\pi} = (1 \pm 7)\%$, where the large uncertainty reflects the differences in experimental results. The statistical error on the most precise single measurement (by BABAR [50]) is 8.5%. Only one measurement in the $\psi(2S)\pi$ mode has been made, by Belle, $A_{CP}^{\psi(2S)\pi} = (2.2 \pm 8.5 \pm 1.6)\%$ [51]. It is therefore interesting to measure $A_{CP}^{\psi\pi}$ down to the percent level to test whether an unexpectedly large contribution from the penguin decay is present.

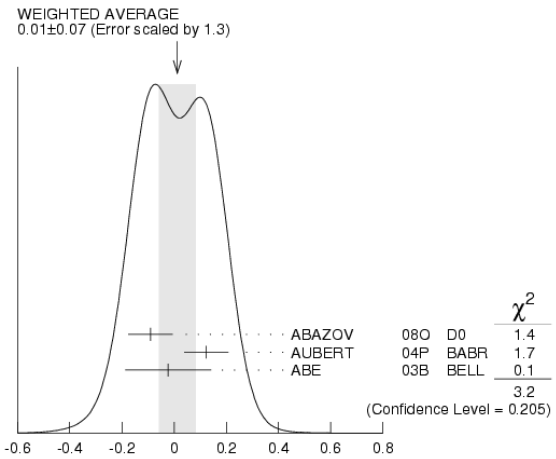

Figure 1.11: The PDG average of $A_{CP}^{J/\psi\pi}$ prior to this thesis [49].

1.8 Rare B decays

The B meson can also decay via a flavour changing neutral current (FCNC) decay. As discussed in Section 1.6.2, rare decays are sensitive to new physics, and their various branching fractions and asymmetries are being probed extensively by the B factories and LHCb. The dimuon final state is often chosen as this gives the cleanest detector signal, and so allows the most sensitive measurements.

The $b \to s$ transition in the FCNC $B \to K\mu^+\mu^-$ decay was seen for the first time at Belle [56], and was complementary to the observation of the radiative penguin $B \to X_s\gamma$ decay made at CLEO [57]. It has subsequently also been observed by BABAR [58]. LHCb recently measured $\mathcal{B}(B^\pm \to K^\pm\mu^+\mu^-) = (4.36\pm0.15\pm0.18)\times10^{-7}$ [59] which is in agreement with the previous world average result of $(4.8 \pm 0.4) \times 10^{-7}$ [38].

The $b \to d$ FCNC transition is suppressed by a Cabibbo factor in comparison to $b \to s$ transitions (see Figure 1.12). The predicted branching fraction of the $B^\pm \to \pi^\pm\mu^+\mu^-$ decay is $2.03 \pm 0.23 \times 10^{-8}$ [60]. This decay has not been seen at the B factories Belle and BABAR. The best experimental limit for this decay mode is from the Belle collaboration, who published $B^\pm \to \pi^\pm\ell^+\ell^- < 4.9 \times 10^{-8}$ [61]. BABAR has a similar result of $B^\pm \to \pi^\pm\ell^+\ell^- < 1.2 \times 10^{-7}$ [62], where both results are at 90% confidence level.

Various new physics models predict enhancement in $B^\pm \to h^\pm\mu^+\mu^-$ decays, including Higgs doublet models [63], R-parity violating supersymmetry [60], R-parity conserving su-

persymmetry [64] and fourth generation quarks [65]. Variations in the predicted branching fraction of $B^{\pm} \to \pi^{\pm}\mu^{+}\mu^{-}$ decays from these new physics models range from $\sim 10\%$ [63] to an order of magnitude [60] [65].

1.8.1 Ratio of CKM elements

The ratio of CKM elements $|V_{td}/V_{ts}|$ has been determined from the oscillation frequencies of neutral B and B_s mesons in mixing processes [66]:

$$\frac{|V_{td}|}{|V_{ts}|} = \xi \sqrt{\frac{\Delta m_d}{\Delta m_s}\frac{m(B_s^0)}{m(B^0)}} = 0.2110 \pm 0.0009 \pm 0.0055\,, \tag{1.46}$$

where ξ is the SU(3) flavour-symmetry breaking factor. It has also been measured at the B factories using the ratio of branching fractions of the radiative FCNC decays (see Figure 1.7). These measurements are consistent within their uncertainties:

$$\begin{aligned} \text{Belle}: \quad & \frac{|V_{td}|}{|V_{ts}|} = 0.199\, {}^{+0.026}_{-0.025}\,(exp.)\, {}^{+0.018}_{-0.015}\,(theo.)\ [67] \\ \text{BABAR}: \quad & \frac{|V_{td}|}{|V_{ts}|} = 0.199 \pm 0.022(stat.) \pm 0.024(syst.) \pm 0.002(th.)\ [68]\,. \end{aligned} \tag{1.47}$$

The $b \to s\ell^{+}\ell^{-}$ and $b \to d\ell^{+}\ell^{-}$ transitions offer an additional way to measure this quantity. Moreover, these transitions are possibly sensitive to different new physical processes contributing to the loop.

Measuring the ratio of branching fractions $R^{\mu\mu}$ gives access to the ratio of CKM matrix elements via a scaling factor:

$$R^{\mu\mu} = f^2 \frac{|V_{td}|^2}{|V_{ts}|^2}\,, \tag{1.48}$$

where f is the ratio of the relevant form factors and Wilson coefficients, integrated over the available phase space. This calculation was performed for $b \to (s,d)\ell^{+}\ell^{-}$ transitions by modifying the EvtGen package [69] to take into account recent updates to the Wilson coefficients and power corrections [70], improved modelling of the q^2 dependence of these coefficients [71], [72], and updated form factors ([73] - "set II"). From this it was calculated that $f = 0.87$.

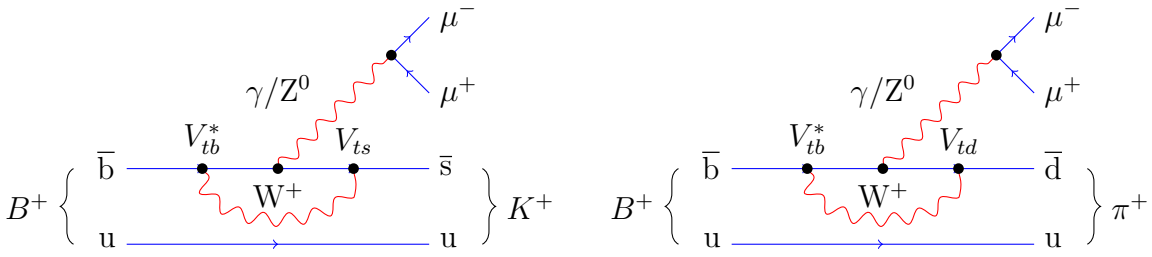

Figure 1.12: $B^{\pm} \to h^{\pm}\mu^+\mu^-$ decays where $h = K$ (left) and $h = \pi$ (right). The two decays vary in the CKM matrix element at the end of the $W^{\pm}$ loop.

1.8.2 *CP* asymmetry

In the Cabibbo favoured $b \to s$ transition the *CP* asymmetry is suppressed in the SM [74]. Models with extensions to the SM predict that this negligible *CP* asymmetry can be enhanced up to 4.5% [75]. The *CP* asymmetry in this mode has been measured by the Belle collaboration to be $A_{CP}^{\mu\mu K} = (-5 \pm 13 \pm 3)\%$ [76], so this is not yet experimentally tested.

In the SM, $b \to d$ transitions are expected to show larger *CP* violating effects. The charge asymmetry in the decay $B^{\pm} \to \pi^{\pm}e^+e^-$ has been calculated to be -5% [77]. The measurement of $A_{CP}^{\mu\mu\pi}$ made in Chapter 4 using LHCb data is the first of its kind.

Chapter 2

The LHCb detector

The data analysed in this thesis were recorded in 2011 by the LHCb experiment at CERN. This chapter describes the experimental apparatus, its operation and performance.

2.1 The LHC

The Large Hadron Collider (LHC) is an approximately circular particle accelerator of 27 km circumference, located 100 m underground at CERN in Geneva, Switzerland [78]. Two beams of protons circulate in opposite directions, and are brought into collision at four experimental sites.

The LHC is the final component in a chain of accelerators that takes protons from hydrogen and accelerates them to multi-TeV energies (see Figure 2.1). In 2011, the LHC accelerated each beam of protons from its injection energy of 450 GeV to 3.5 TeV[1], so providing a centre of mass energy of $\sqrt{s} = 7$ TeV. The protons in each beam are separated into bunches, each of approximately 10^{11} particles.

Acceleration and bunch separation are achieved using radio frequency (RF) cavities. Eight cavities act on each beam with an accelerating gradient of 5 MV m^{-1}. The frequency of the field is 400 MHz; for 25 ns spacing every tenth wave is filled with a particle bunch to deliver collisions at 40 MHz. The maximum voltage of the cavities is 16 MV, this provides a bunch length of 7.5 cm. During the 20 minute ramp, each cavity provides 32 kW to increase

[1] 450 GeV in 2009, 3.5 TeV in 2010, 4 TeV in 2012

the beam energy [79].

The beams are bent by super-conducting dipole magnets, which operate at 1.9 K and produce a bending field of 8.4 T. A range of additional quadrupole and sextupole magnets are used to focus and adjust the beams. Some of these magnets also operate at super-conducting temperatures (1.9 K, 4.5 K), others are normal-conducting ($< 65°$C).

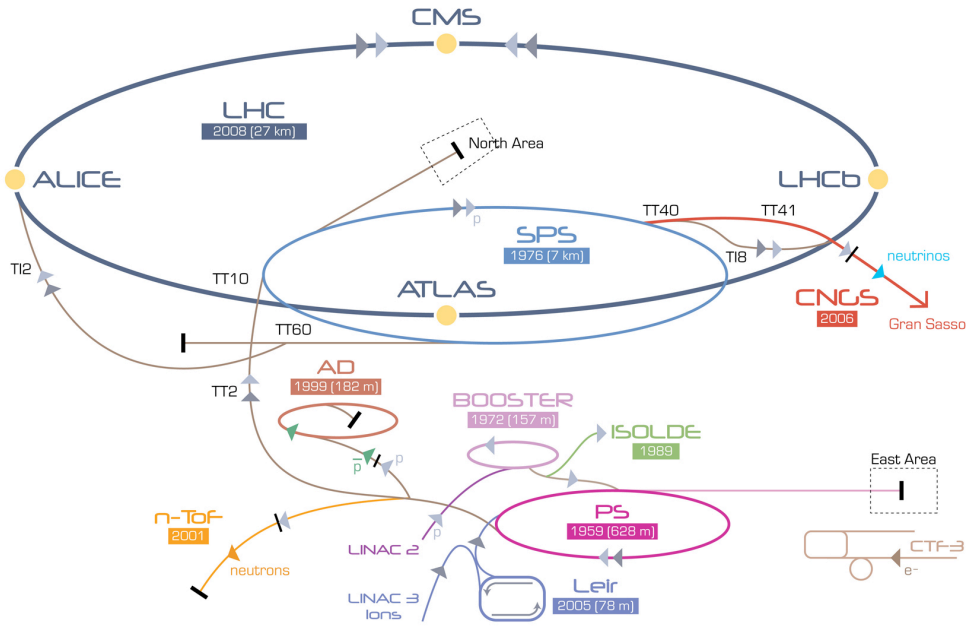

Figure 2.1: The CERN accelerator complex, showing the injection system leading to the LHC: LINAC2, BOOSTER, PS, SPS, LHC.

In 2011, the maximum number of bunches in the LHC was 1380, with a minimum bunch spacing of 50 ns. At 25 ns the maximum number of bunches is 2808. This does not correspond to a full ring, in order to allow the kicker magnets enough time to ramp during a beam dump.

2.2 LHCb overview

LHCb is a spectrometer which instruments the forward region of the proton-proton (pp) collisions using a variety of detector technologies (see Figure 2.2) [80]. This asymmetric shape takes advantage of the forward bias in $b\bar{b}$ production in the multi-TeV energies - b quarks are light in comparison to the collision energy and so highly boosted along the beam

axis. The detector is located at LHC Interaction Point 8 (IP8)[2].

The basic components of a spectrometer are a magnet and particle tracking system. The trajectory of a particle which traverses the magnetic field is deflected by an amount inversely proportional to the particle's momentum, and in a direction according to the particle's charge. In LHCb, tracking stations before and after the magnet are used to determine the direction and curvature of a particle's trajectory through the field, and hence the particle's charge and momentum.

The detector is synchronised with the accelerator but a trigger is required to fire to read out data. The electronic and hadronic calorimeters and the muon chambers can quickly assess the 'activity' present in the detector from each bunch crossing. They provide the first hardware layer of the trigger. Selected events are passed to a software trigger for further filtering.

In order to perform B physics analyses, a precision vertex detector is vital to distinguish between primary pp interaction vertices and secondary B meson decay vertices. Ring imaging Cherenkov detectors provide dedicated hadron identification which is critical to distinguish kinematically similar final states of B decays.

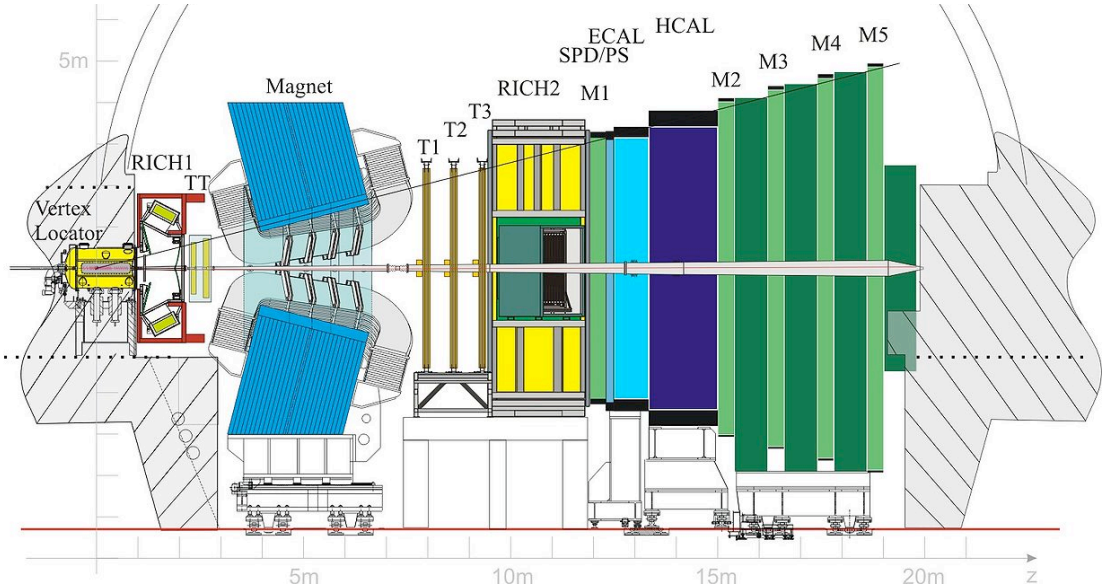

Figure 2.2: The LHCb detector shown from the side (non-bending plane). RICH1-2 are ring imaging Cherenkov detectors. TT and T1-3 are tracking stations. M1-5 are muon stations. The SPD/PS, ECAL and HCAL are part of the calorimeter system.

[2]IP1: ATLAS, IP2: ALICE, IP5: CMS, IP8: LHCb

LHCb uses a right-handed Cartesian coordinate system. The origin is defined as the interaction point, situated within the Vertex Locator (see Figure 2.2). The z axis follows the beam-pipe, and is positive through LHCb. The plane of the LHC is defined by the tunnel, which slopes at 1.42% with respect to the horizontal [81]. x lies in this plane and points positively toward the centre of the ring. y points approximately vertically upwards.

2.2.1 Running conditions in 2011

Due to the development of the LHC, the LHCb trigger strategy altered from the original plan of maintaining a low number of interactions per bunch crossing (~ 0.7). Challenges with the injector system meant that luminosity targets were easier to achieve with fewer, higher intensity bunches than expected. Vetoing events with more than one visible pp interaction would have severely reduced the recorded luminosity. Therefore, for most of 2011, LHCb ran at 150% of design instantaneous luminosity, with only 35% of the foreseen number of bunches. There were generally $1.5 - 2.5$ visible interactions per event, see Figure 2.3(a).

In order to control the number of interactions per event, LHCb makes use of luminosity levelling. This is achieved by moving the beams apart, so reducing the colliding area. As the number of protons in the bunch decreases, the beams are gradually moved together to create a constant rate of collisions. This is shown in Figure 2.3(b). The two general purpose detectors, ATLAS and CMS, receive much higher instantaneous luminosity than LHCb, but this falls away over time. The LHCb luminosity is level throughout the fill.

2.3 Magnet

The dipole magnet of LHCb consists of two sets of saddle shaped aluminium coils and a steel yoke, see Figure 2.4(a) [82]. In total it weighs ~ 1600 tons. The magnet draws 5.8 kA of current during operation and is water cooled, operating at 50°C. A warm magnet was chosen for mechanical simplicity and the ability to quickly ramp and easily reverse the field. The polarity of the magnet is periodically reversed during data taking, which simplifies the systematic studies in asymmetry measurements.

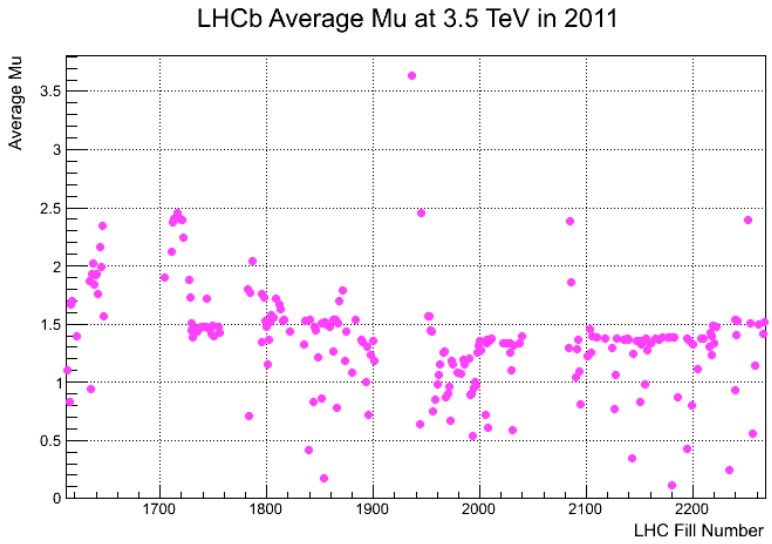

(a)

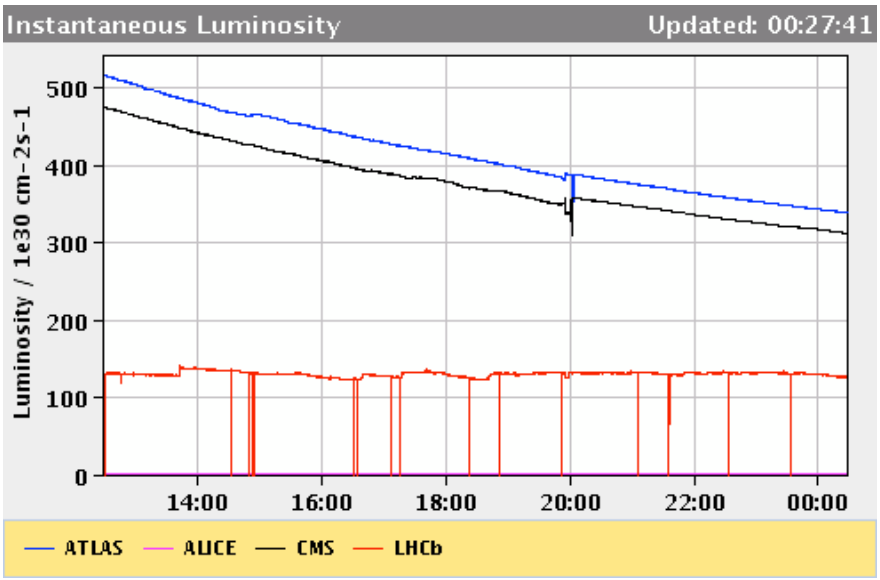

(b)

Figure 2.3: a) Average number of visible pp interactions per event ("Mu") in 2011 data. This is determined by counting, at 40 MHz, the number of beam-beam crossings with no visible interaction in the calorimeter. Mu is the negative logarithm of the fraction of empty beam-beam crossings. b) Demonstration of the luminosity levelling used by LHCb. The red undulating line around $100 \times 10^{30}\,\mathrm{cm}^{-2}\mathrm{s}^{-1}$ is the instantaneous luminosity delivered to LHCb.

The magnetic field strength is at maximum 1.1 T (Figure 2.4(b)). A particle going from the interaction point through the centre of the magnet experiences a field integral of $\int B\mathrm{dl} = 4.2\,\mathrm{Tm}$. This varies by up to $\pm 6\%$ for tracks which go through different regions of the acceptance.

The poles of the magnet are shaped to follow the acceptance of LHCb, see Figure 2.2. This has the advantage of reducing the electrical requirements of the magnet, whilst retaining the same bendng power. In spite of this, the magnet is the most power hungry component of LHCb. Of the 8 MW available to LHCb, 6 is reserved for the magnet and 2 for the detector electronics and computing. The actual power consumption of the magnet is 4.2 MW.

Tilting the poles has the effect of producing a stronger field at the magnet's entrance. It is considered necessary that the field close to the collision region is small, to allow fast, straight track reconstruction to be used in the trigger. Furthermore, components of the ring imaging Cherenkov detectors are sensitive to magnetic fields. Therefore, the sub-detectors upstream of the magnet are protected from fringe fields by two iron shielding plates.

The magnetic field was measured in 2005 and again before the start of data taking in 2011 [83]. The updated field map was used for the reconstruction of data used in this thesis.

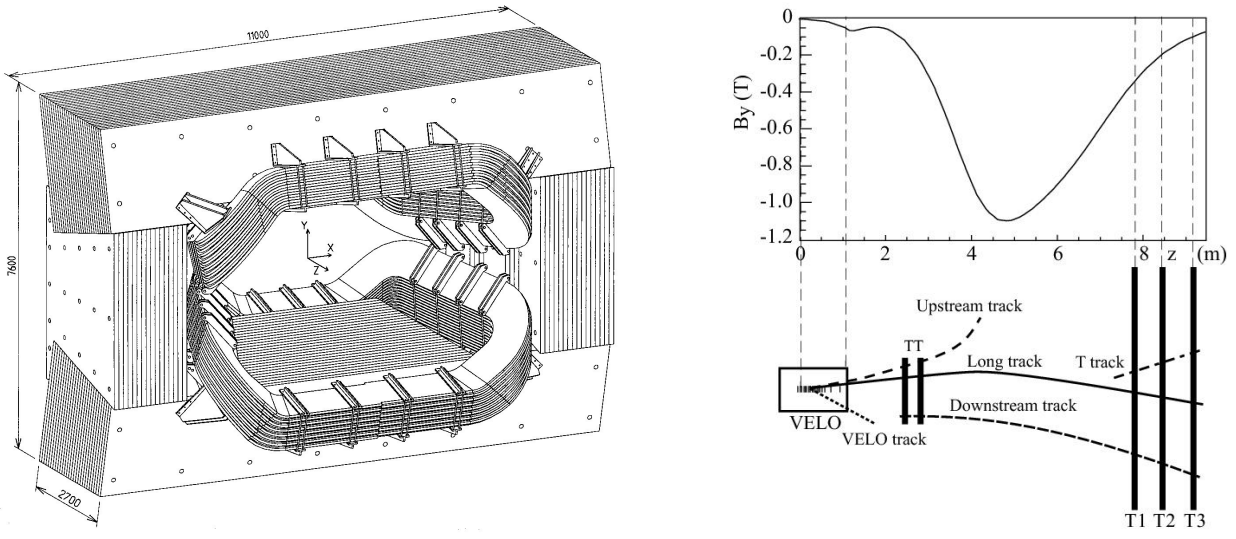

(a) (b)

Figure 2.4: a) The LHCb magnet viewed from the larger aperture side. b) The B_y field experienced by particles as they traverse the tracking detectors (seen above). The track types (seen below) are defined by the tracking stations which a track passes through.

2.4 Tracking

The tracking system of LHCb comprises five stations, two upstream of the magnet and three downstream, see Figure 2.5. These are labelled in Figure 2.2 as the TT (two stations), T1, T2 and T3. The three stations after the magnet make use of two different tracking technologies, depending on the distance from the beam-pipe. These sub-detectors are called the inner and outer trackers. The overall tracking efficiency was measured in 2011 data using the tag and probe method on $J/\psi \to \mu^+\mu^-$ decays. For the momentum spectrum and track multiplicity of the J/ψ decay products the efficiency was found to be above 96% [84].

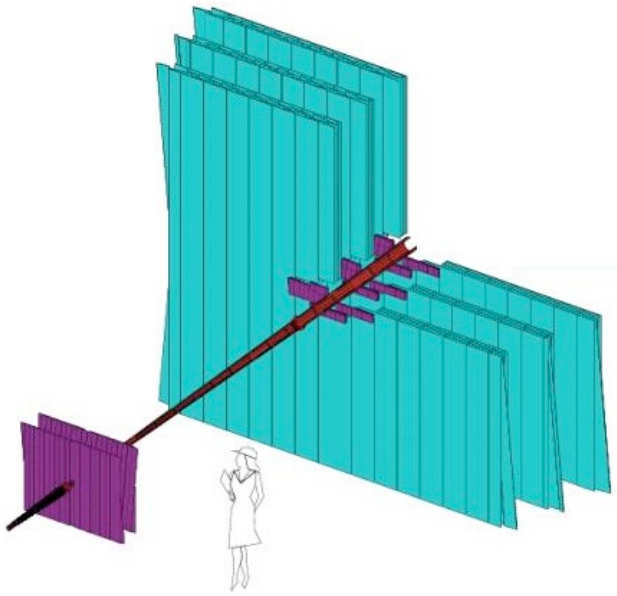

Figure 2.5: The LHCb tracking system. On the left are the two stations of the TT. Back right are the T1, T2 and T3 stations, each of which is made up of two detector technologies. In purple are the silicon microstrip Inner Tracker detectors. In blue are the straw tube Outer Tracker detectors.

2.4.1 TT

The TT is located upstream of the magnet and provides track position and direction information before the magnetic field. It therefore provides vital information on low momentum particles which are deflected out of LHCb before reaching the downstream tracking stations. The TT also aides locating the decay vertices of long lived particles like the K^0_S which, due to the high collision energy and therefore high boost, usually decay outside the vertex detector.

The TT is a silicon microstrip tracker with strips up to 38 cm in length and with 200 µm pitch. It consists of 4 layers which are arranged in pairs with $\sim$ 30 cm between them, see Figure 2.6. The first and last layers have vertical silicon strips, and are called x layers because they measure the horizontal position. The second and third layers have strips which are inclined at $\pm 5^\circ$ to the vertical, denoted u and v layers. The inclined angle provides positional information in the vertical direction. The predominantly vertical orientation of the strips gives best resolution in the horizontal plane (the bending plane of the magnet) to ensure an accurate momentum estimation.

The measured hit efficiency in the TT is 99.3%. This is calculated from data by extrapolating tracks with momentum greater than 10 GeV/c through active material, and counting how often a hit has been detected where one is expected. The single hit resolution is determined by considering the residual between the measured hit position and the extrapolated track position. The hit resolution of the TT is 62 µm.

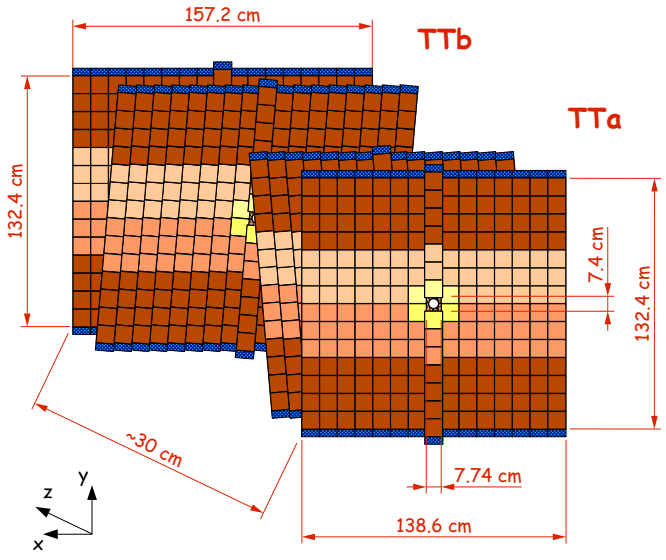

Figure 2.6: The TT, which makes up the first two tracking stations. The $x-u-v-x$ arrangement is shown. Strips (not visible) are oriented vertically, or at $\pm 5^\circ$ to the vertical to give excellent horizontal resolution. The inclined strips provide information on the vertical position of tracks.

2.4.2 Inner tracker

The Inner Tracker (IT) comprises three tracking stations, and occupies the area closest to the beam pipe, see Figure 2.5. This area receives the highest flux of particles, and so must have better resolution than the outer regions in order to distinguish individual tracks. Each station forms a cross around the beam pipe (see Figure 2.7) and consists of four layers of silicon microstrip detector. Strips are 11 or 22 cm in length and have pitch 200 µm. The layers have the same $x-u-v-x$ arrangement as the TT, with two layers of vertical strips and two layers of strips at $\pm 5°$. The total active area is about $4\,\mathrm{m}^2$, which accounts for 1.3% of the T1-T3 area. However, 20% of tracks within the LHCb acceptance go through the IT. In a similar way to TT, the hit efficiency can be measured. The IT was determined to be 99.8% efficient for single hits. The measured hit resolution of the IT is 58 µm.

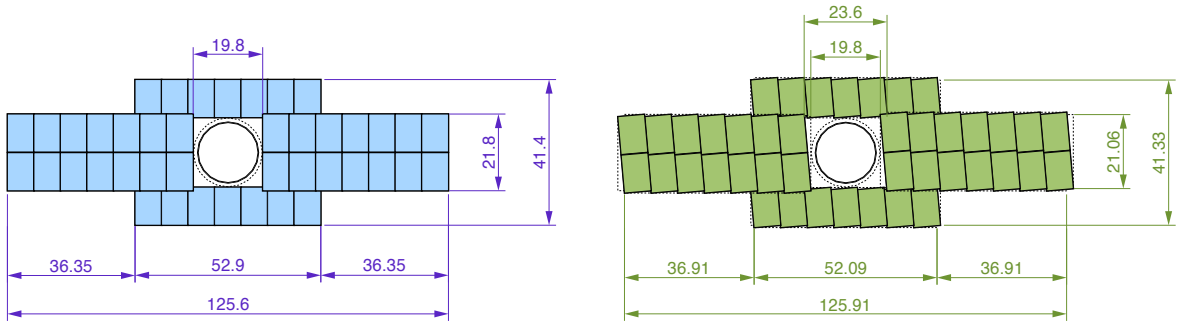

(a) (b)

Figure 2.7: The LHCb IT station layout. Dimensions are in cm. a) A layer with vertical strips, denoted x layer. b) A u or v layer, with strips inclined at 5° to the vertical.

2.4.3 Outer tracker

The Outer Tracker (OT) makes up the remainder of the three T1-T3 tracking stations, as it surrounds each of the Inner Tracker detectors (see Figure 2.5). As the particle flux is less at greater distance from the beam pipe, this detector utilises gaseous straw tubes. The area of the largest of the three stations is $6\,\mathrm{m} \times 4.9\,\mathrm{m}$. Each of the three stations contains four layers of detector, arranged in the same $x-u-v-x$ configuration as the TT and IT. Each x, u or v layer contains a double layer of straw tubes, see Figure 2.8.

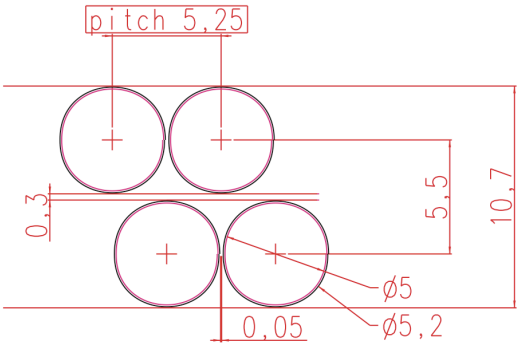

Figure 2.8: The LHCb OT tube layout. Dimensions are in mm.

The tubes have a 4.9 mm inner diameter, and are filled with 70% argon and 30% carbon dioxide gas. When a charged particle passes through the tube, it ionises the gas particles and produces electrons. These drift toward the anode wire in the centre of the tube, and the time this takes gives information on the position of the track, see Figure 2.9(a). In 2011 the LHC operated with both 75 ns and 50 ns bunch crossing. The contribution from earlier and later bunch crossings in these two regimes is visible in the drift time spectrum, see Figure 2.9(b).

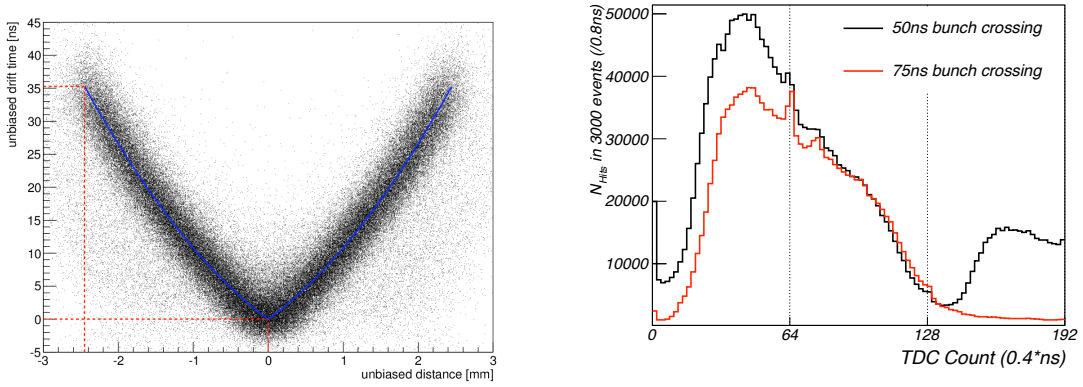

(a) (b)

Figure 2.9: a) Drift time versus distance from anode. The drift time from the outer wall to the anode is 35 ns. b) Drift time spectrum in the 50 ns and 75 ns bunch crossing regimes.

A scan of the hit efficiency was performed on 2011 data, see Figure 2.10(a). The average single cell efficiency for tracks closer than 1.25 mm from the center of the straw was measured to be 99.2%. The hit resolution is determined for tracks with a momentum larger than 10 GeV/c. The distribution of hit residuals is shown in Figure 2.10(b) resulting in a single hit resolution of 211 µm, close to the design value of 200 µm.

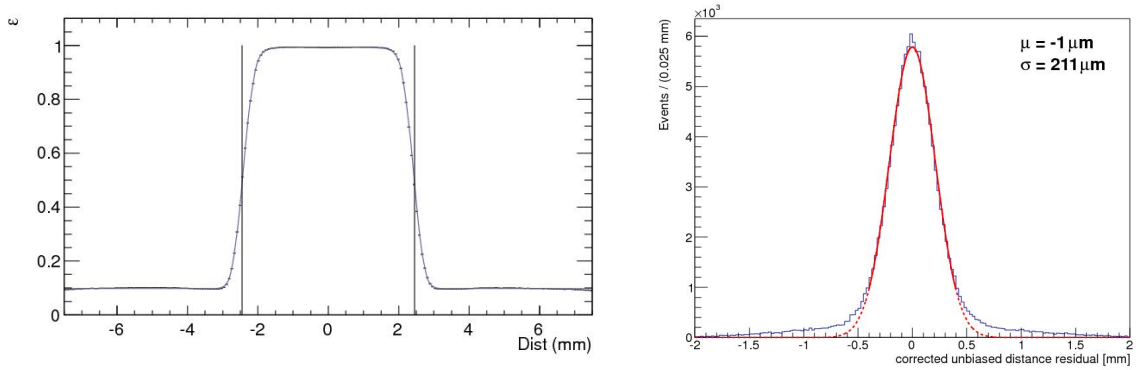

(a) (b)

Figure 2.10: a) Hit efficiency profile across a straw. The vertical bars represent the edges of the straw. The efficiency drops near the edge due to the lower probability of ionisation for a short path, and the smearing from track resolution. b) OT single hit resolution. The fitted resolution function (red) has a width of 211 μm.

In 2009 it was discovered that the OT suffers from gain loss after irradiation, due to the build up of an insulating layer on the anode wire [85]. Tests showed that the contamination was caused by the outgassing of a glue used in construction. The problem is mitigated by flushing out the contamination, adding 1% oxygen to the gas mixture, and cleaning the anode wires by occasionally applying high voltage. This does not significantly affect the physics performance of the detector.

The relative momentum resolution of tracks passing through all tracking stations was measured using $J/\psi \rightarrow \mu^+\mu^-$ decays in data, see Figure 2.11. The relative momentum resolution is $\sim 5 \times 10^{-3}$ for particles below 20 GeV/c and $\sim 9 \times 10^{-3}$ for particles with momentum 100 GeV/c.

2.5 Calorimeter

The calorimeter system of LHCb is used to measure the positions and energies of hadrons, electrons and photons. This information is of primary importance in the trigger and for particle identification. Scintillator is used as the active material throughout the calorimeter. This creates photons when an ionising particle traverses it. The photon energy is removed from the scintillator by wavelength shifting fibres, which decrease the self-absorption of the

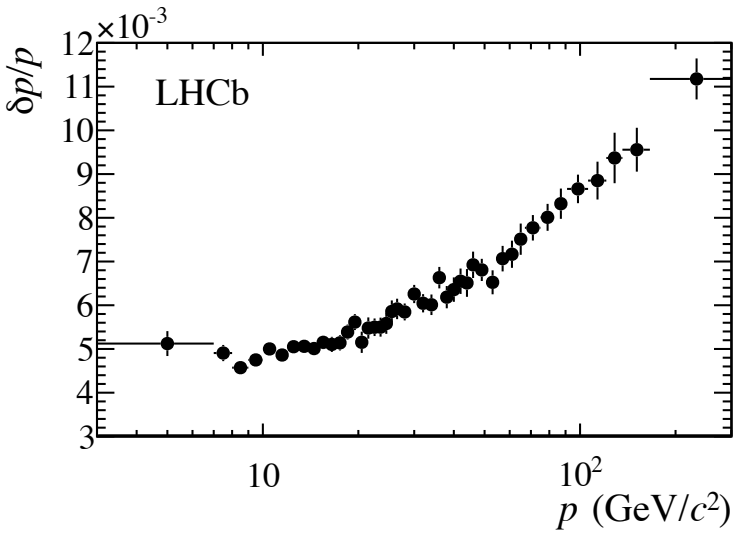

Figure 2.11: Relative momentum resolution ($\delta p/p$) of tracks which have passed through all tracking stations, as a function of momentum. Tracks are taken from $J/\psi \to \mu^+\mu^-$ decays in data.

scintillator and match the absorption spectrum of the photomultiplier tubes used to collect the signal. The calorimeter comprises four components (see Figure 2.12):

- **SPD**

  A Scintillating Pad Detector (SPD) forms the first layer of the calorimeter. This is used to reject high E_T neutral pions in the trigger, which can mimic electrons as no track requirement is made. Charged particles interact in the scintillator material, neutral particles do not.

- **PS**

  A 15 mm (2.5 radiation lengths) thick layer of lead provides the longitudinal segmentation required to identify electrons from the high background of charged pions. The PreShower (PS) detector picks up particle showers originating in the lead. As electrons have a shorter interaction length than hadrons, the electrons will begin to shower in the lead converter. Combined with information from the ECAL, this helps to reject charged pions from the electron selection.

- **ECAL**

  The electromagnetic calorimeter (ECAL) is a sampling calorimeter composed of scintillator and lead. Layers of alternating 2 mm lead, 120 µm white paper and 4 mm

scintillator form a stack 42 cm long, corresponding to 25 radiation lengths. This fully contains high energy photons and electrons, giving good energy resolution. The hit density varies by two orders of magnitude across the face of the detector, so variable lateral segmentation is used in the inner, middle and outer regions (Figure 2.13(a)). Square modules are divided into $9, 4$ or 1 readout cells, with transverse lengths $4.04, 6.06$ and 12.12 cm. The Molière radius is 3.5 cm, so a shower will usually be contained within 4 modules.

The electron identification performance was measured in 2011 data using the tag and probe method on $B^{\pm} \to J/\psi\,(\to e^+e^-)K^{\pm}$ decays. The average efficiency is $92.8 \pm 1.2\%$ for a misidentification rate of $1.01 \pm 0.01\%$, after requiring $\Delta \log \mathcal{L}(e-h) > 4$ [86].

- **HCAL**

  The hadronic calorimeter (HCAL) weighs 500 tons and is composed of scintillator and lead tiles which are oriented lengthways along z. There are two sizes of cell, see Figure 2.13(b). The thickness of the HCAL is only 5.6 interaction lengths, as the trigger does not require full hadronic shower containment. The energy resolution was determined in a test beam to be:

$$\frac{\sigma_E}{E} = \frac{(69 \pm 5)\%}{\sqrt{E}} \oplus (9 \pm 2)\%\,, \tag{2.1}$$

  (E in GeV), where the first term is due to the stochastic nature of shower development, and the second constant term is due to energy independent contributions such as instrumental effects.

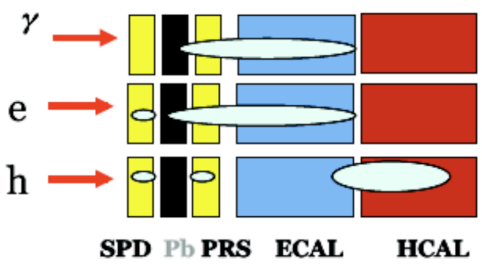

Figure 2.12: The response of the calorimeter layers to photons, electrons and hadrons.

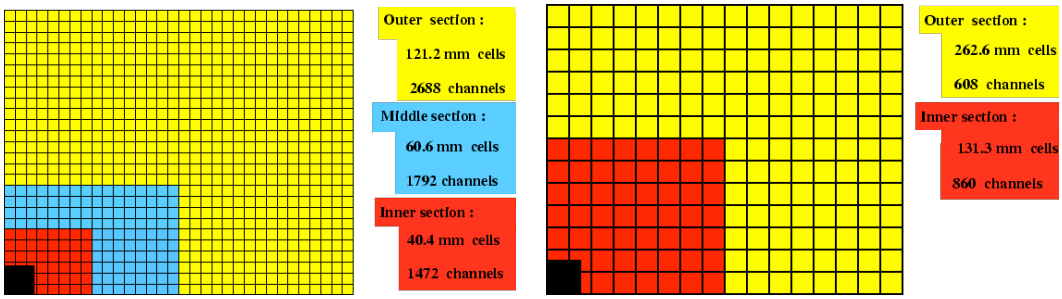

(a) (b)

Figure 2.13: Calorimeter cell arrangement. One quarter of the face is shown. a) ECAL. b) HCAL.

2.6 Muon detector

Efficient detection of muons in LHCb is crucial for both the trigger and the offline muon identification. Muons are present in the final states of many B decays of interest, and so are vital to the physics programme of LHCb. There are five muon stations, marked M1 - M5 in Figure 2.2. M1 is located before the calorimeter, to improve the p_T measurement in the trigger. The remaining four stations are downstream of the calorimeter, and are layered with 80 cm thick iron absorbers to reduce the hadronic background (Figure 2.14(a)). M1 - M3 have high x spatial resolution, to accurately calculate p_T. M4 - M5 have limited spatial resolution, and are used primarily to confirm the penetration of the particles.

The muon stations cover a total area of 435 m^2, and are predominantly multi-wire proportional chambers. The only exception is the inner region of M1, which is a triple-GEM (gas electron multiplier) detector due to the higher flux it experiences. The trigger requires coincidence between all five stations, so a fast gas mixture of Ar, CO_2 and CF_4 (40 : 55 : 5) is used to read out the avalanche signal in under 25 ns.

The muon selection efficiency was measured in 2011 data with $J/\psi \rightarrow \mu^+\mu^-$ decays, see Figure 2.14(b). The efficiency depends on p_T, and is found to be greater than 97% for $p_T > 1700\,\mathrm{MeV}/c$, and greater than 92% for $800 < p_T < 1700\,\mathrm{MeV}/c$. These efficiencies correspond to misidentification rates of $1 - 2\%$ from protons, pions and kaons. Protons are misidentified as muons when noise or a true muon signal in the muon chambers aligns with a proton signal in the calorimeters. Decay in flight is the most common cause of pion and kaon misidentification.

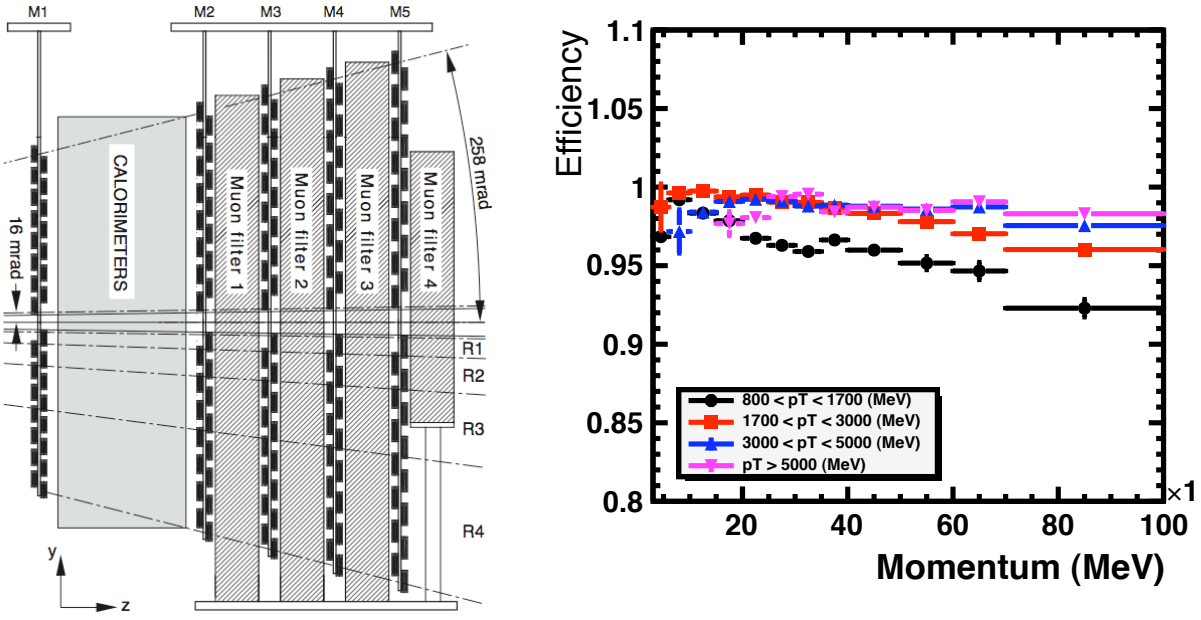

(a) (b)

Figure 2.14: a) Side view of muon system. b) Efficiency of the muon selection, as a function of momentum ($\times 10^3$ has been cropped from the right side of the image). The various colours correspond to different p_T ranges.

2.7 Vertex detector

The LHCb vertex locator (VELO) surrounds the collision point at IP8. Given the focus on forward physics, a telescopic design with detector modules perpendicular to the beam is chosen. The VELO consists of two arrays of semi-circular silicon strip detectors mounted on two movable base plates. This allows for retraction during unstable beam periods, like LHC beam injection, but closure (and so full acceptance in ϕ) during data taking, see Figure 2.15. When closed, the VELO has active material 8.2 mm from the beam axis, with the inner shield just 5 mm from the collisions.

The silicon detectors are in a volume contained by aluminium boxes, which protect the modules from pick-up from the passing beams of charged particles (Figure 2.16(b)). The aluminium foil is 300 µm thick, which is designed to introduce the least amount of material possible into the particle's path. It has a corrugated shape, contouring around the VELO modules. This allows the modules to slightly overlap when closed, guaranteeing full acceptance and aiding detector alignment. The thinness of the foil requires that the VELO

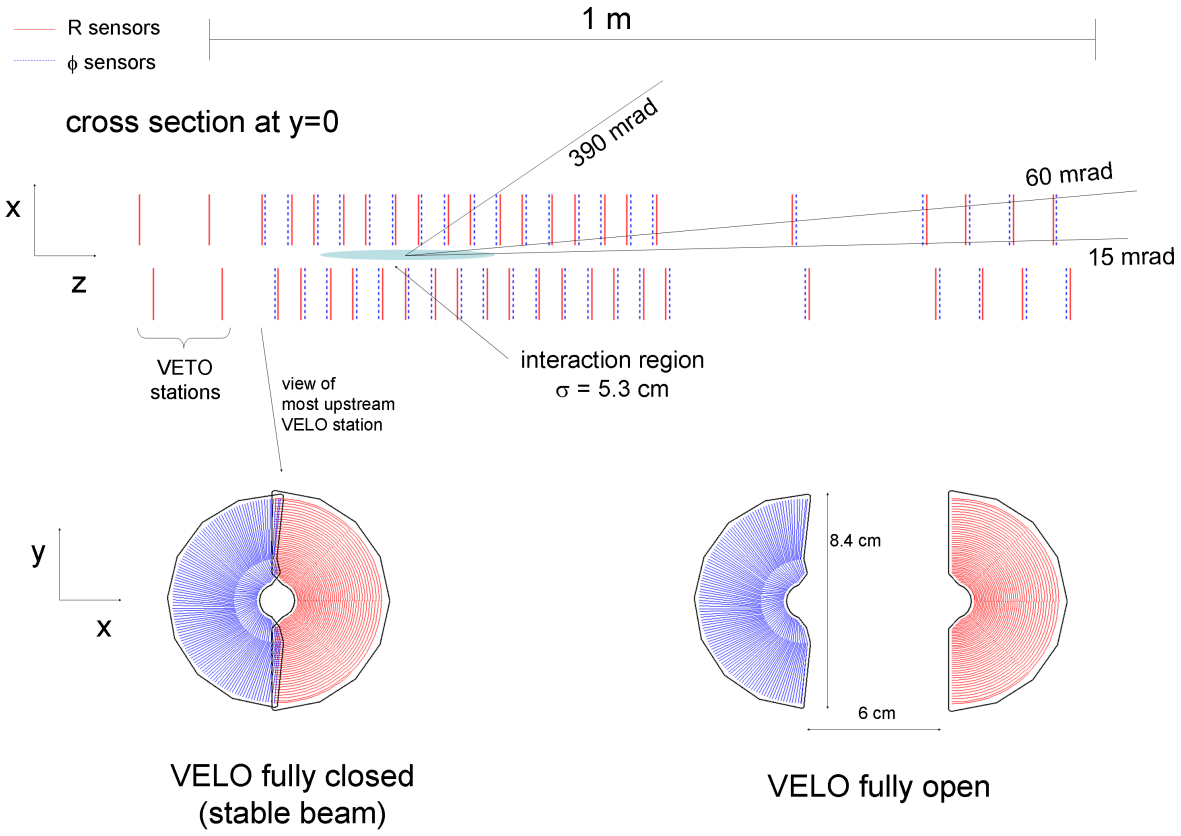

Figure 2.15: Schematic of the VELO. Top: view of the two halves of the VELO, each with 21 full modules plus the two additional pile-up veto modules. Bottom: sensors in the closed and open positions, showing the overlap when fully closed. R sensor shown in red, ϕ sensor in blue.

operates in a vacuum of pressure similar to that of the primary beam vacuum (10^{-8} mbar).

Each module consists of an R and a ϕ sensor (so called because of the co-ordinate which they measure), which are glued back to back onto a supporting PCB that also houses the front-end electronics and cooling (Figure 2.16(a)). Each VELO half has 21 modules, with an additional two modules which measure only R. These modules were designed to veto pile-up events, but in 2011 were used primarily to trigger beam-gas events.

(a) (b)

Figure 2.16: a) VELO modules. b) Interior of the RF foil, viewed in the open position.

2.7.1 Analysis of the primary vertex resolution

LHCb has been designed to study *CP* violation and rare decays of heavy mesons. This requires the accurate measurement of lifetimes and impact parameters, both for triggering and background rejection. Precise vertex reconstruction is therefore of critical importance in order to resolve production and decay vertices.

The analysis to measure the primary vertex resolution is performed on an event by event basis. The principle is to reconstruct the same vertex twice, and to consider the residual difference between these two positions. This is achieved by randomly splitting the track sample of each event into two, and reconstructing a vertex from each independent set of tracks. The two vertices are 'matched' if the difference in their z position is less than 2 mm.

The vertex resolution is strongly dependent on the number of tracks used to reconstruct a vertex (track multiplicity). If the number of tracks in each of the matched vertices is the

same, the residual is calculated. Repeating for many events, a series of residual histograms is populated with the distance between the vertices in x, y, z, for varying track multiplicity. Each residual histogram is fitted with a Gaussian of width σ. The vertex resolution is $\sigma/\sqrt{2}$ as two uncorrelated distance measurements contribute to each residual measurement.

The resolution as a function of track multiplicity (N) is shown in Figure 2.17. It is fitted with a function:

$$\sigma_{PV} = \frac{A}{N^B} + C\,, \tag{2.2}$$

where A, B and C are fit parameters. C can be thought of as the best resolution possible, given multiple scattering.

With 2011 data, it was found that a 25 track vertex has a resolution in the transverse plane of 13 µm. In z the resolution is 71 µm. The same track split method was applied to simulation, see Figure 2.18. In the transverse plane, the vertex resolution in simulation is approximately 2 µm better than in data. The track split method was verified in simulation using truth information, no significant bias was seen.

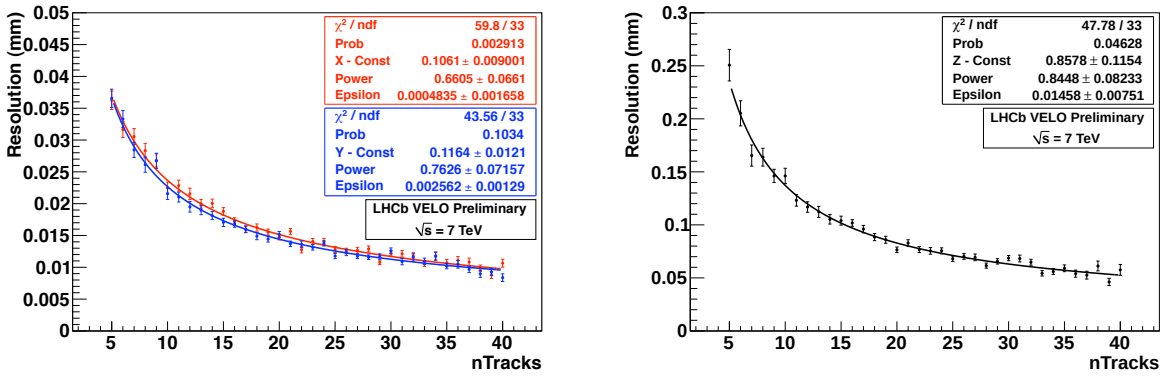

(a) (b)

Figure 2.17: Resolution in 2011 data, as a function of track multiplicity. a) x (red) and y (blue) resolution. b) z resolution.

2.7.2 Analysis of the vertex resolution using beam-gas collisions

It has been suggested in [87] that a precise luminosity measurement is possible if the beam currents and the shapes of the colliding beams are known. This method requires that the positions and transverse widths of the two LHC beams are measured, in order to calculate

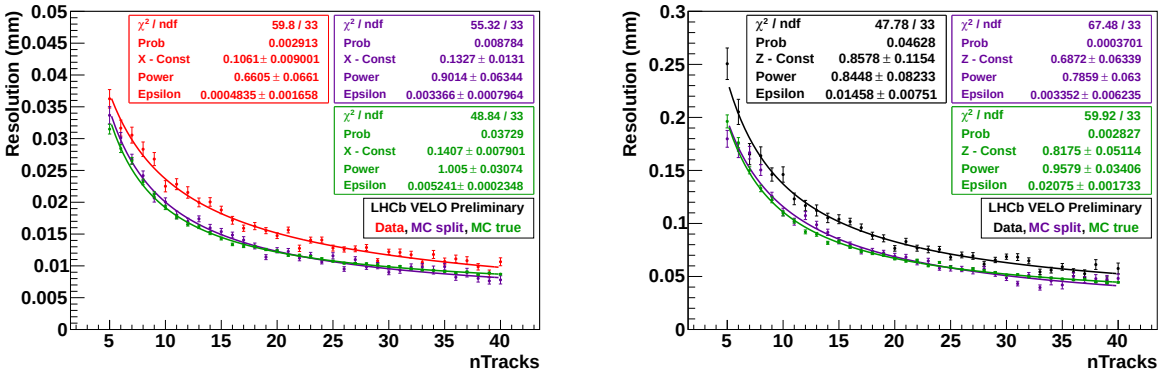

(a) (b)

Figure 2.18: Resolution as a function of track multiplicity. Data is compared with simulation (labelled MC) using the track split method (purple) and truth (green). a) x. b) z.

the effective area of the collisions. Beam-gas vertices (vertices from the collisions of one beam and the residual gas in the vacuum of the beam pipe) are used to ascertain the position and spatial extent of each beam. However, the measured beam width is a convolution of the true width of each beam and the resolution function of the detector. Since the resolution is comparable to the bare beam size (approximately 50 µm), it is crucial to understand this effect, and to be able to unfold it from the measured values.

The beam-gas vertex resolution depends on the multiplicity of the vertex (as with beam-beam vertices) and also on the z position of the interaction. Due to the high quality of the LHC vacuum, beam-gas events are rather rare so the analysis is split into two steps. Beam-beam events are used to measure precisely the resolution's dependence on track multiplicity (described in the previous section) at $z = 0$. Subsequently, beam-gas vertices are used to measure the dependence on z.

Beam-gas events are selected from bunch crossings which the LHC global timing system declares as 'beam-empty'. As with the beam-beam analysis, the total track sample is randomly split into two. However, the residual is calculated independently of how many tracks created the two vertices. The contribution to the resolution from the track multiplicity can be taken into account:

$$F_c = \frac{x_1 - x_2}{\sqrt{\sigma^2_{PV_1} + \sigma^2_{PV_2}}}, \tag{2.3}$$

where $1, 2$ signifies the two vertices. In this way, every beam-gas event which yields two ver-

tices can be used in the analysis, without requiring that the two vertices were reconstructed with an equal number of tracks.

Accounting for the resolution due to track multiplicity means that a correction factor F_c is calculated, as a function of z position. This is the factor by which the beam-beam resolution at $z = 0$ must be multiplied to find the true resolution for an event with a particular number of tracks, at a certain position in z. The correction factors are plotted in Figure 2.19.

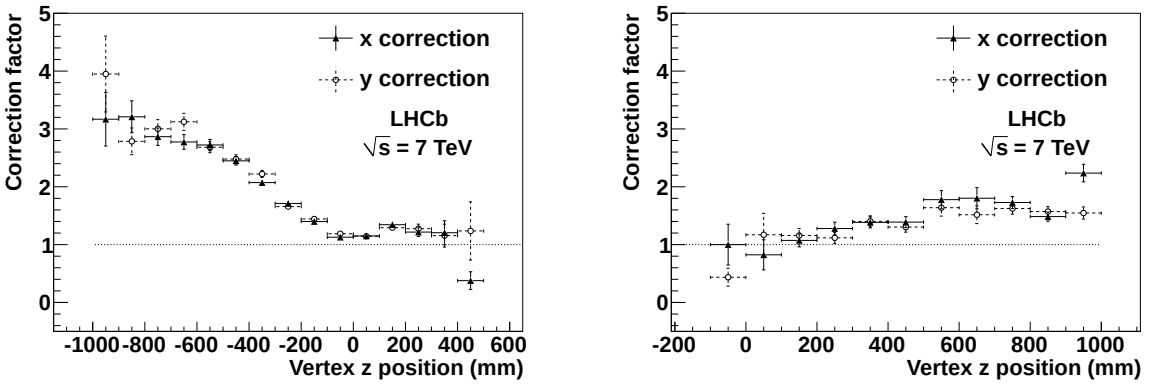

(a) (b)

Figure 2.19: 2011 resolution corrections as a function of location in z for a) Beam 1, b) Beam 2.

The resolution is seen to increase for beam-gas vertices away from $z = 0$ by up to a factor 3 for vertices reconstructed 1000 mm from the interaction point. The accurate reconstruction of vertices up to 1 m away from the default interaction region exemplifies the good performance of the VELO.

The vertex resolution is small enough and calculated with sufficient precision so that it may be unfolded from the reconstructed beam widths to give the true effective area of collisions. Knowledge of the positions and spatial extents of the two beams, in addition to the number of protons per bunch, is used to calculate the collision luminosity. In 2010 data, this method was used in conjunction with a more established technique (a Van der Meer scan) to measure a total cross section of $58.8\,\mu\text{b} \pm 3.5\%$ [2]. During data collection, the number of interactions is counted, and used as a normalisation factor to calculate the luminosity relative to calibration samples. The 2010 dataset was measured to be $35\,\text{pb}^{-1}$, 2011 data $1.024\,\text{fb}^{-1}$.

2.8 Particle identification

LHCb has two Ring Imaging Cherenkov (RICH) detectors to distinguish between different species of charged particles. This is important for background rejection but crucial for separating the Cabibbo favoured and suppressed modes detailed later in this thesis. Cherenkov photons are produced when particles travel through a dielectric medium faster than the local speed of light. Cherenkov photons are emitted at an angle which depends on the particle's speed. By detecting these photons, the angle can be measured and, combining with the momentum measurement, the mass (and therefore identity) of the particle can be deduced.

Three radiators of different refractive indices are used to cover the momentum range of interest. RICH1, located upstream of the LHCb dipole magnet, consists of two radiators. A 5 cm thick layer of aerogel was intended to provide separation for slow particles in the $1 - 8\,\mathrm{GeV}/c$ momentum range, and C_4F_{10} gas is used for particles with $p < 60\,\mathrm{GeV}/c$. RICH2, downstream of the magnet, uses CF_4 gas to identify high momentum particles (up to $100\,\mathrm{GeV}/c$). Spherical and flat mirrors with 90% reflectivity are used to divert the Cherenkov photons out of the LHCb acceptance, to where they are detected using Hybrid Photon Detectors [88], see Figure 2.20.

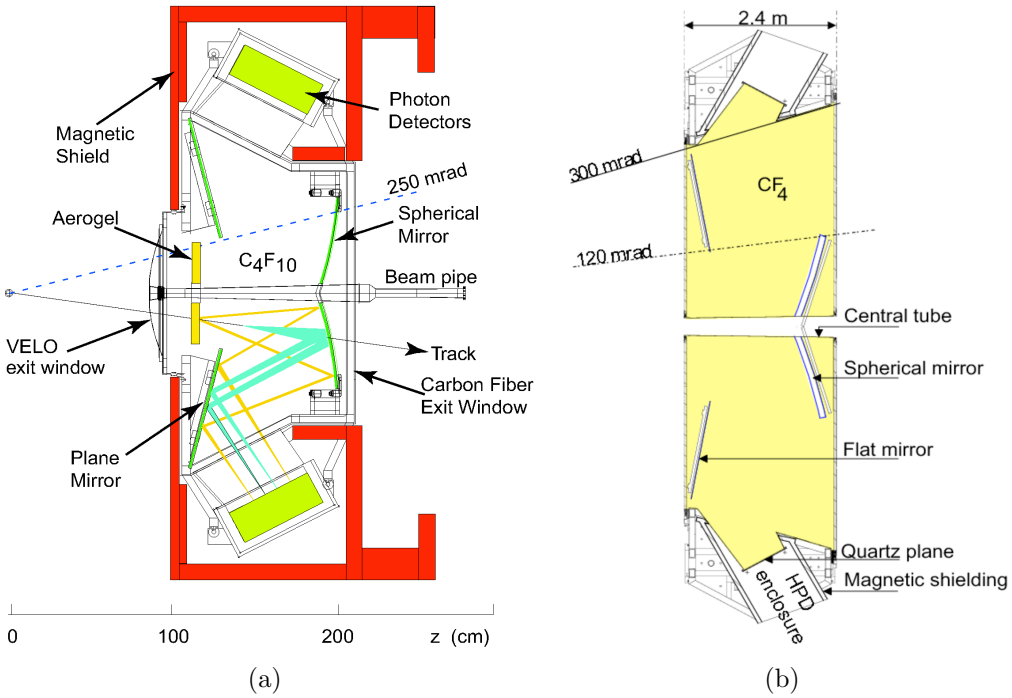

(a) (b)

Figure 2.20: RICH detector cross sections. a) RICH1. b) RICH2.

The RICH detectors are especially important as the LHCb HCAL does not provide a full energy measurement for hadrons. It is therefore necessary to create a mass 'hypothesis' for each particle, based on information from the RICH detectors, calorimeters and muon stations. The identity of particles is described by using log likelihood differences, $\Delta \log \mathcal{L}(h-\pi)$, which compare the calculated likelihoods between two mass hypotheses. The default hypothesis is pion. Four comparisons are made: with kaon, proton, electron and muon hypotheses (h). Depending on the detector response to the particle, the $\Delta \log \mathcal{L}$ variable will reflect how likely each mass hypothesis is.

The performance of the RICH detectors was measured in 2011 data [89]. Figure 2.21 shows the Cherenkov angle of isolated tracks, as a function of the particle momentum. The data falls into bands, according to the particle type. The particle identification efficiencies and misidentification rates are measured using high statistics samples of $K^0_S \to \pi^+\pi^-$, $\Lambda^0 \to p^+\pi^-$ and $D^0 \to K^+\pi^-$ decays. Results are shown in Figure 2.22 as a function of momentum. Two distinguishing selections are used, based on a loose and tight $\Delta \log \mathcal{L}$ requirement.

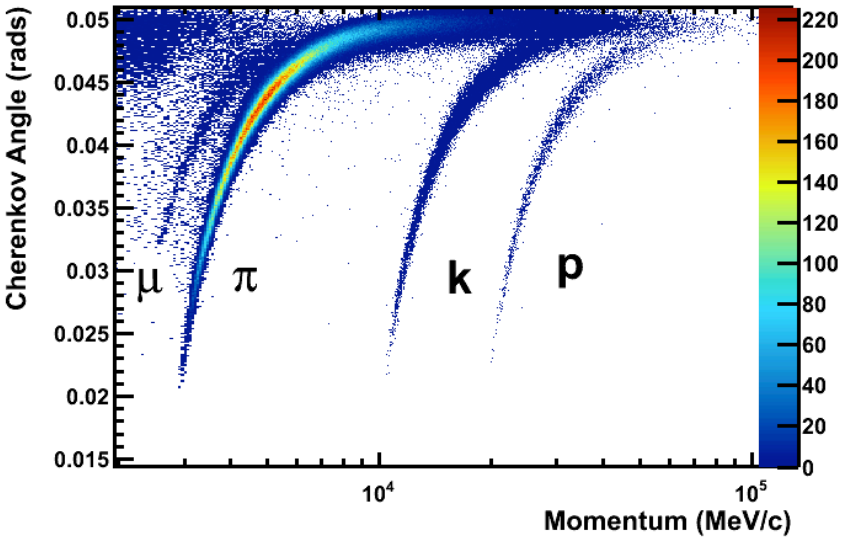

Figure 2.21: Cherenkov angle as a function of momentum for isolated tracks measured in C_4F_{10} from 2011 data. The curved bands correspond to different types of particle.

The single photoelectron resolution of the aerogel was measured in 2010, and was found to be significantly worse than expected. This was caused by the porous aerogel absorbing the C_4F_{10} surrounding it, which altered its optical properties [90]. An air-tight enclosure has been manufactured, and was installed before the 2012 data taking.

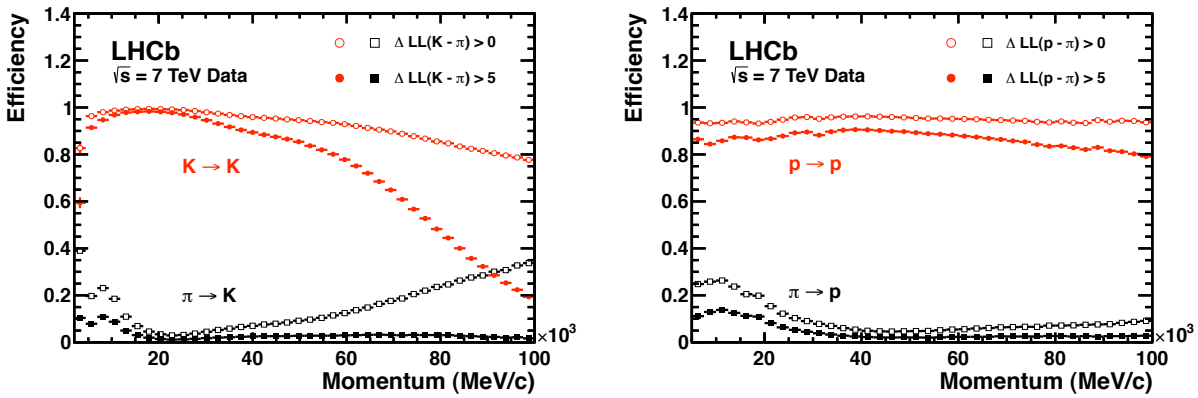

(a) (b)

Figure 2.22: Kaon (a) and proton (b) identification efficiency, as a function of momentum. Two different $\Delta \log \mathcal{L}$ requirements are shown, loose (open markers) and tight (closed markers). The pion misidentification rate is also shown.

2.9 Trigger

The LHCb trigger must choose which events are kept for further analysis. This is crucial, as $\sigma_{b\bar{b}}/\sigma_{inelastic} < 1\%$, and most B decays of interest have a branching fraction less than 10^{-5}.

The LHCb trigger has three levels: the Level 0 trigger (L0), and two High Level Triggers (HLT1 and HLT2). Their purpose is to reduce the rate from 11 MHz - the rate of visible pp collisions in LHCb in 2011, to 3 kHz - the rate at which events can be recorded to tape.

L0 is a hardware trigger, which reduces the 11 MHz collision rate down to 1 MHz. It uses information from the muon chambers and the calorimeter, and detects high-p_T muons, and high-E_T calorimeter objects. These two signals indicate the presence of a heavy meson decay. The total latency for these decisions is 4 µs. The full detector can be read out at 1 MHz.

The HLT is a software trigger, comprising C++ algorithms which run on $\sim$ 2000 multi-core processors in the event filter farm. HLT1 takes the detector output at 1 MHz and reduces it to 30 kHz. It reconstructs tracks by including information from the VELO and tracking stations. This enables vertexing and finding tracks with high impact parameter and p_T. In this way HLT1 confirms or rejects the L0 candidates.

HLT2 reduces this 30 kHz by approximately a factor of 10, down to 3 kHz. It performs a global track reconstruction and applies inclusive or exclusive selections similar to those used

in analyses, for example invariant mass selections, decay length cuts, muon and electron identification. The typical event size written to storage was expected to be 35 kB, but with 2011 data including more visible pp interactions than expected, this increased to 60 kB.

The overall efficiency of the muon triggers used in this thesis were measured in 2011 data. Offline reconstructed $B^{\pm} \to J/\psi K^{\pm}$ candidates were found to be selected by the muon triggers with an efficiency of $83.9 \pm 1\%$ [91].

2.10 Data processing

Events which pass the HLT are processed at computer centres around the world. Storage and processing facilities at these sites are connected through the Worldwide LHC Computing Grid. The Grid makes use of 115 sites in 21 countries, LHCb has access to 107 sites.

Each 'run' of data recorded by LHCb (about an hour's worth of data taking) is sent to one Grid site for processing. This may be CERN (the Tier0 site) or one of six Tier1 sites. Processing involves decoding the raw data and reconstructing track candidates. A Kalman filter [92] is used in the reconstruction to ascertain the probability of a track undergoing multiple scattering, given the track's path through the detector. Processing takes around 24 hours per run, and the result is written into an SDST file.

The reconstructed events from the SDST files are stripped. This is the process in which raw tracks are made into decay candidates. Tracks are assigned particle hypotheses, for instance tracks with hits in the muon stations become muon candidates. Groups of tracks are combined to give candidates of heavier particles usually at displaced secondary vertices. Numerous stripping lines are defined each with the purpose of selecting decays of interest. For example, for a B analysis the combined tracks would be required to be compatible with the B mass and to have come from a vertex displaced from the primary vertex.

Similar stripping lines are combined into streams, such as charm, electro-weak, and dimuon (the stream used for this thesis). The files for each stream are merged to give the DST files. These are replicated at CERN and three other Tier1 sites, and are archived twice to give a total of 6 copies. (Two copies of the raw data are kept.)

Users are then able to run their analysis jobs on the Grid, making use of the relevant stream of stripped data. In 2011, LHCb users ran almost 20 million jobs on the Grid, see Figure 2.23, corresponding to 15 thousand years worth of CPU time.

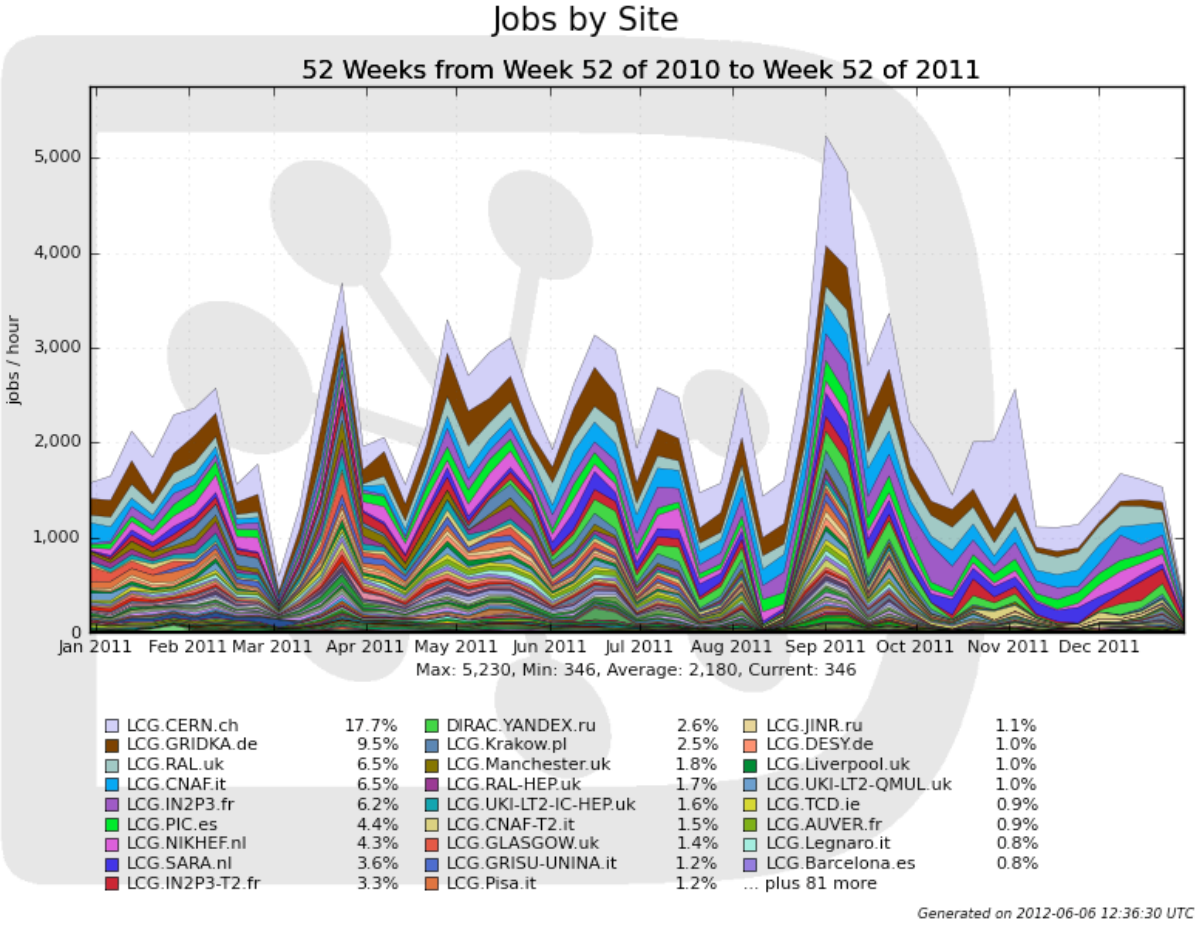

Figure 2.23: Number of jobs per hour executed on the GRID by LHCb users during 2011. Different colours correspond to different sites. CERN and the Tier1 sites carry the highest load.

Chapter 3

The branching fractions and CP asymmetries of $B^{\pm} \to \psi\pi^{\pm}$ decays

This chapter describes an analysis of $B^{\pm} \to \psi h^{\pm}$ decays ($h = \pi, K$), focussing on the Cabbibo suppressed $\psi\pi^{\pm}$ modes. The two quantities of interest are the CP asymmetry;

$$A_{CP}^{\psi h} = \frac{\mathcal{B}(B^- \to \psi h^-) - \mathcal{B}(B^+ \to \psi h^+)}{\mathcal{B}(B^- \to \psi h^-) + \mathcal{B}(B^+ \to \psi h^+)}\,, \tag{3.1}$$

and the charge-averaged ratio of branching fractions:

$$R^{\psi} = \frac{\mathcal{B}(B^{\pm} \to \psi\pi^{\pm})}{\mathcal{B}(B^{\pm} \to \psi K^{\pm})}\,, \tag{3.2}$$

where ψ is either a J/ψ or $\psi(2S)$ reconstructed in the $\mu^+\mu^-$ final state.

As covered in Chapter 1, the Standard Model predicts that for $b \to c\bar{c}s$ decays the tree and penguin contributions have a small relative weak phase and thus no significant direct CP violation is expected in $B^{\pm} \to \psi K^{\pm}$. For $B^{\pm} \to \psi\pi^{\pm}$, the tree and penguin contributions have different phases and CP asymmetries at the percent level may occur, see Equation 1.45. An additional asymmetry may be generated, also at the percent level, from long-distance rescattering [54]. Any asymmetry larger than this would be of significant interest.

3.1 Datasets and validation

This analysis is performed using 0.37 fb^{-1} of data, recorded during the first half of 2011. Data is taken from two stripping lines (see Section 2.10) which select $B^\pm \to h^\pm\mu^+\mu^-$ final states, where $h = K, \pi$. The $J/\psi \to \mu^+\mu^-$ and $\psi(2S) \to \mu^+\mu^-$ resonances are contained within this dataset, in addition to non-resonant dimuon pairs with $m_{\mu\mu} > 250\,\text{MeV}/c^2$.

A second dataset, recorded in 2010, is considered in order to validate simulation samples. This is necessary as some correction factors in the analysis are taken from simulation, which is tuned to replicate running conditions from 2010 and is reconstructed and stripped with the same software as the stripped datasets from this period.

Stripping selections are shown in Table 3.1, with variables defined in the Glossary. $B^\pm \to \pi^\pm\mu^+\mu^-$ and $B^\pm \to K^\pm\mu^+\mu^-$ selections are identical except for the RICH-based particle identification requirement on the hadron. Therefore the $B^\pm \to K^\pm\mu^+\mu^-$ dataset is a subset of the $B^\pm \to \pi^\pm\mu^+\mu^-$ dataset, reconstructed under an alternative hadron mass hypothesis.

Variable	2010 selection	2011 selection
$h^\pm\mu^+\mu^-$ mass (MeV/c^2)	$5050 - 5779$	$4879 - 5679$
$B^\pm$ pointing angle ($^\circ$)	< 3.624	< 1.812
$B^\pm$ decay vertex χ^2	< 30	< 21
$\mu^+\mu^-$ mass (MeV/c^2)	> 250	> 250
$\mu^\pm$ track χ^2/ndf	< 5	< 5
$\mu^\pm$ momentum (MeV/c)	> 3000	> 3000
$\mu^\pm$ transverse momentum (MeV/c)	> 500	> 500
$\mu^\pm$ impact parameter χ^2	> 4	> 4
$h^\pm$ track χ^2/ndf	< 5	< 5
$h^\pm$ momentum (MeV/c)	> 2000	> 2000
$h^\pm$ transverse momentum (MeV/c)	> 300	> 500
$h^\pm$ impact parameter χ^2	> 4	> 4
$K^\pm$ $\Delta \log \mathcal{L}(K - \pi)$	> -1	> -5

Table 3.1: Stripping selections for $B^\pm \to h^\pm\mu^+\mu^-$ in 2010 and 2011. The $\Delta \log \mathcal{L}(K - \pi)$ selection is only applied to the hadron when under the kaon hypothesis.

Stripped candidates are reconstructed as $B^\pm \to \psi(\to \mu^+\mu^-)h^\pm$, using the appropriate hadron mass hypothesis for each stripping line. Each B candidate decay is refitted using DecayTreeFitter [93]. This algorithm takes advantage of knowing the whole decay chain to fit vertex positions and momentum parameters of all particles in the B decay simultaneously. During this fit, the J/ψ and $\psi(2S)$ masses are constrained to their nominal values [49]. The

primary vertex is also refitted, excluding tracks used in the B decay of interest.

3.1.1 Data-simulation comparison of $B^{\pm} \to J/\psi\, K^{\pm}$

$B^{\pm} \to J/\psi\, K^{\pm}$ decays in 2010 data are compared with simulation in Figures 3.1 and 3.2. In these figures data are background suppressed using the ${}_s$Weighting technique[1] [94]. The plots show that simulation adequately describes the data within the selected ranges. Unusual variables used for comparison are described in the Glossary. Noteworthy features are now discussed in detail:

- $K^{\pm}\mu^{+}\mu^{-}$ and $\mu^{+}\mu^{-}$ mass distributions are shown before DecayTreeFitter has been applied. Once the ψ mass has been constrained by the fit, the width of the $K^{\pm}\mu^{+}\mu^{-}$ mass distribution narrows, and the $\mu^{+}\mu^{-}$ mass spectrum becomes a delta-function. Dimuon mass selections are applied before the mass constraint is imposed.

- The cosine of the $B^{\pm}$ pointing angle variable peaks sharply towards 1. For the data-simulation comparison it is therefore useful to transform it into a smoother distribution using $\log_{10}(1 - \cos(B^{\pm}\text{ pointing angle}))$. However, this results in an isolated peak of events with $\cos(B^{\pm}\text{ pointing angle}) = 1$ (to float precision) being assigned to $\log_{10}(1 - \cos(B^{\pm}\text{ pointing angle})) \equiv 0$. As shown in Figure 3.1, the selection retains all useful events.

- The track χ^2/ndf variable shows poor agreement between data and simulation, particularly for hadron tracks. This is a common feature seen in many LHCb analyses. The track χ^2/ndf variable is not used in the analysis.

The impact of observed differences between data and simulation is minimised by using only the simulated difference between $B^{\pm} \to \psi K^{\pm}$ and $B^{\pm} \to \psi \pi^{\pm}$ decays. Remaining differences are accounted for by systematic uncertainty evaluation.

[1]The reconstructed B mass distribution of data is fitted with signal and background fit components. Events are assigned a weight calculated by dividing the signal PDF height by the total PDF height at their particular mass. The weights are applied when variables are compared between data and simulation.

3.1.2 Comparison of $B^{\pm} \to J/\psi\, K^{\pm}$ and $B^{\pm} \to J/\psi\, \pi^{\pm}$ simulation

$B^{\pm} \to J/\psi\, \pi^{\pm}$ and $B^{\pm} \to J/\psi\, K^{\pm}$ simulations are compared in Figures 3.3 and 3.4. As expected, the kinematic properties of the two decays are almost identical. This indicates that the correction factor due to differences in reconstruction and selection efficiency between the two modes should be close to 1.

3.2 Selection

A selection was devised using the independent 2010 data and simulation samples. Variables with good distinguishing power are exploited to separate the B signal from random combinations of tracks. A series of independent, rectangular cuts were chosen to roughly maximise the significance ($S/\sqrt{S+B}$) in simulation, whilst taking into account simulation-data differences. This maximises the $J/\psi\, K^{\pm}$ mass peak in data whilst retaining a manageable level of background.

The final selections applied on top of those in Table 3.1 are shown in Table 3.2. Kinematic requirements are made on the hadron, and vertex χ^2 requirements are placed on both the reconstructed ψ and B candidates. The pointing angle selection is an important discriminator between combinatorial background and signal decays. The ψ mass resonance is exploited by requiring events to fall within $^{+30}_{-40}\,\mathrm{MeV}/c^2$ of the nominal value [49]. This asymmetry allows for the radiative tail of the ψ. Two further selections are made, now described in detail, which exploit specific kinematic characteristics of $B^{\pm} \to \psi h^{\pm}$ decays.

Variable	J/ψ selection	$\psi(2S)$ selection
$B^{\pm}$ decay vertex χ^2	< 10	< 10
$B^{\pm}$ impact parameter χ^2	< 25	< 25
$B^{\pm}$ pointing angle ($^{\circ}$)	< 0.573	< 1.812
ψ decay vertex χ^2	< 10	< 10
ψ mass (MeV/c^2)	3097^{+30}_{-40}	3686^{+30}_{-40}
$h^{\pm}$ momentum (MeV/c)	> 5000	> 5000
$h^{\pm}$ transverse momentum (MeV/c)	> 1000	> 1000
cos($h^{\pm}$ decay angle)	< 0	-
Same sign $m_{\pi\mu}$ (MeV/c^2)	-	> 300

Table 3.2: The selection criteria applied to $B^{\pm} \to \psi h^{\pm}$ candidates.

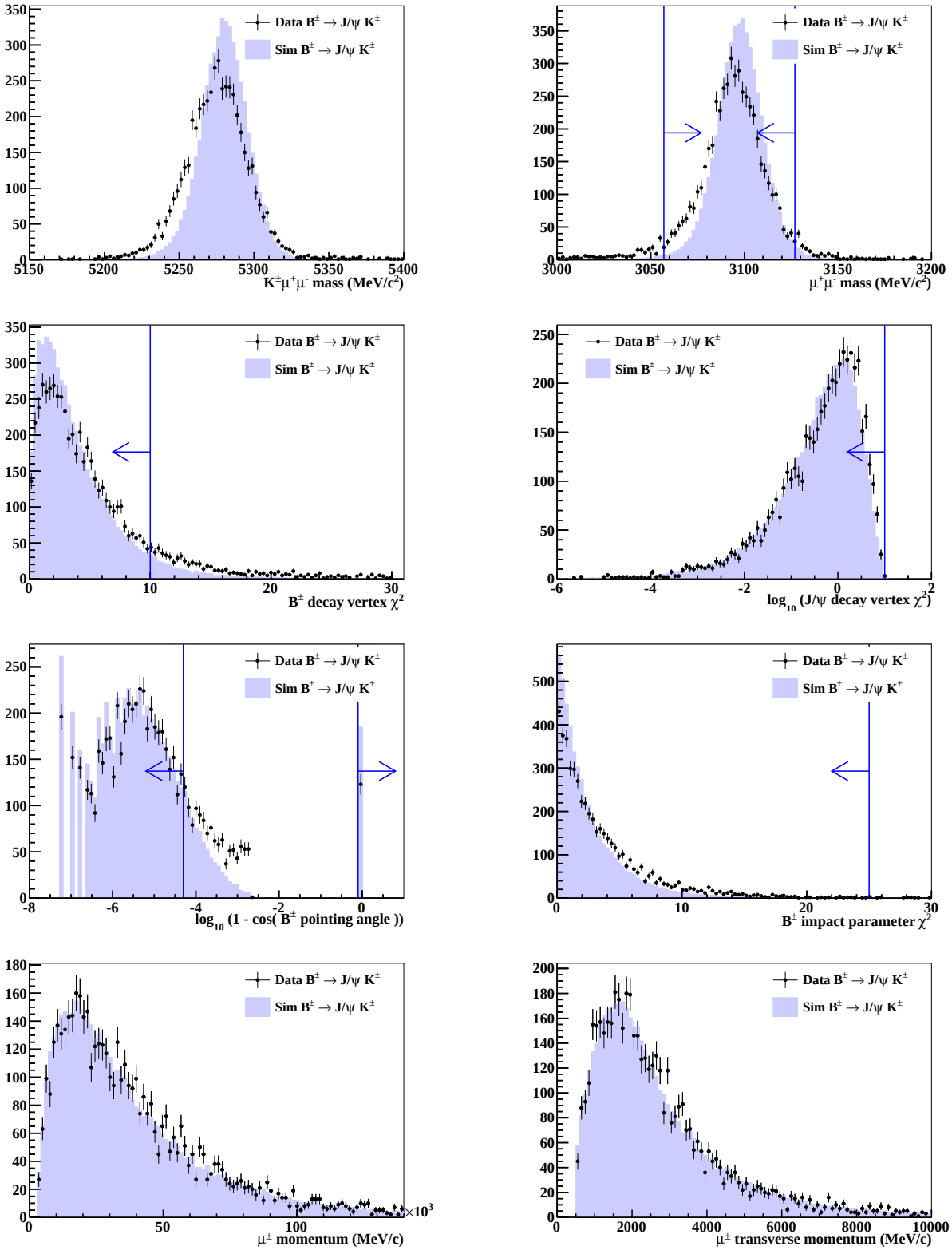

Figure 3.1: Comparison between selected $B^{\pm} \to J/\psi K^{\pm}$ events in 2010 data and $B^{\pm} \to J/\psi K^{\pm}$ simulation. Simulation (shaded blue) is scaled down to have the same entries per plot as the data (black points). Selection cuts are shown with a blue vertical line and arrow. All other cuts, except that on the plotted variable, are applied in each plot. Data is signal-only, isolated using the ${}_s$Weights.

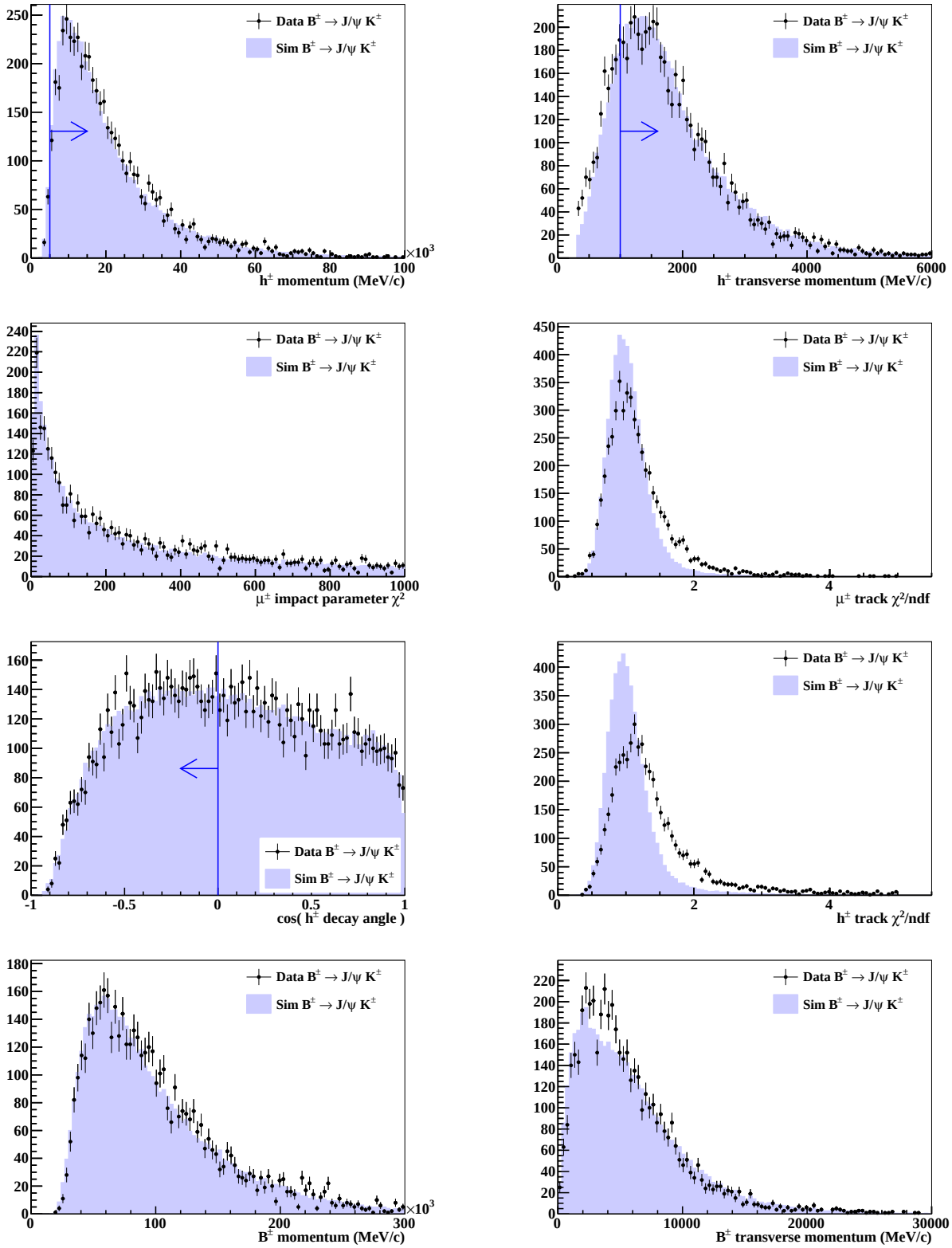

Figure 3.2: Comparison between selected $B^{\pm} \to J/\psi K^{\pm}$ events in 2010 data and $B^{\pm} \to J/\psi K^{\pm}$ simulation. For details see Figure 3.1 caption.

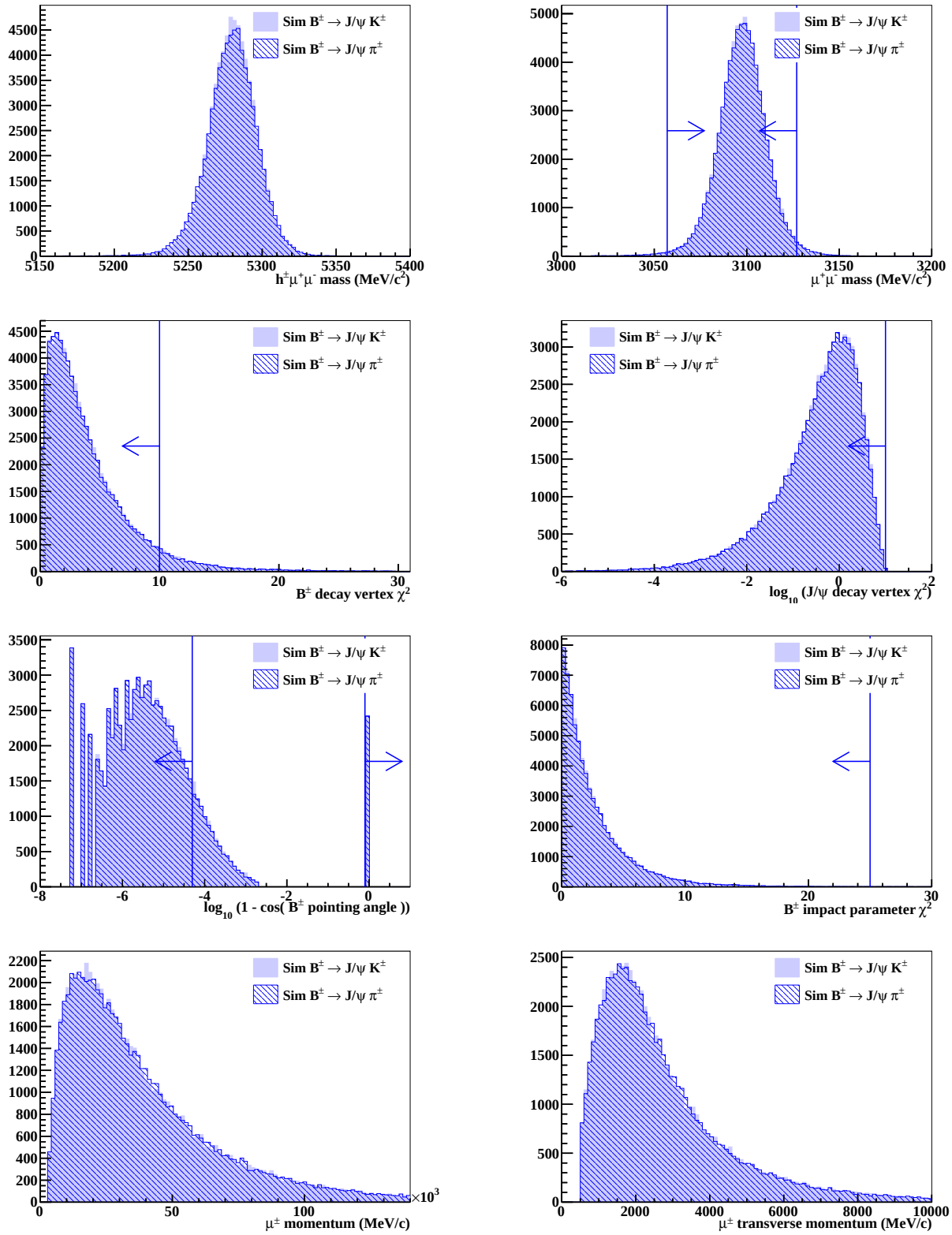

Figure 3.3: Comparison between selected $B^{\pm} \to J/\psi\pi^{\pm}$ and $B \to J/\psi K^{\pm}$ simulation. The $B^{\pm} \to J/\psi\pi^{\pm}$ plot (hashed) is scaled to have the same number of entries as the $B^{\pm} \to J/\psi K^{\pm}$ plot (shaded). The blue vertical line indicates the employed cut.

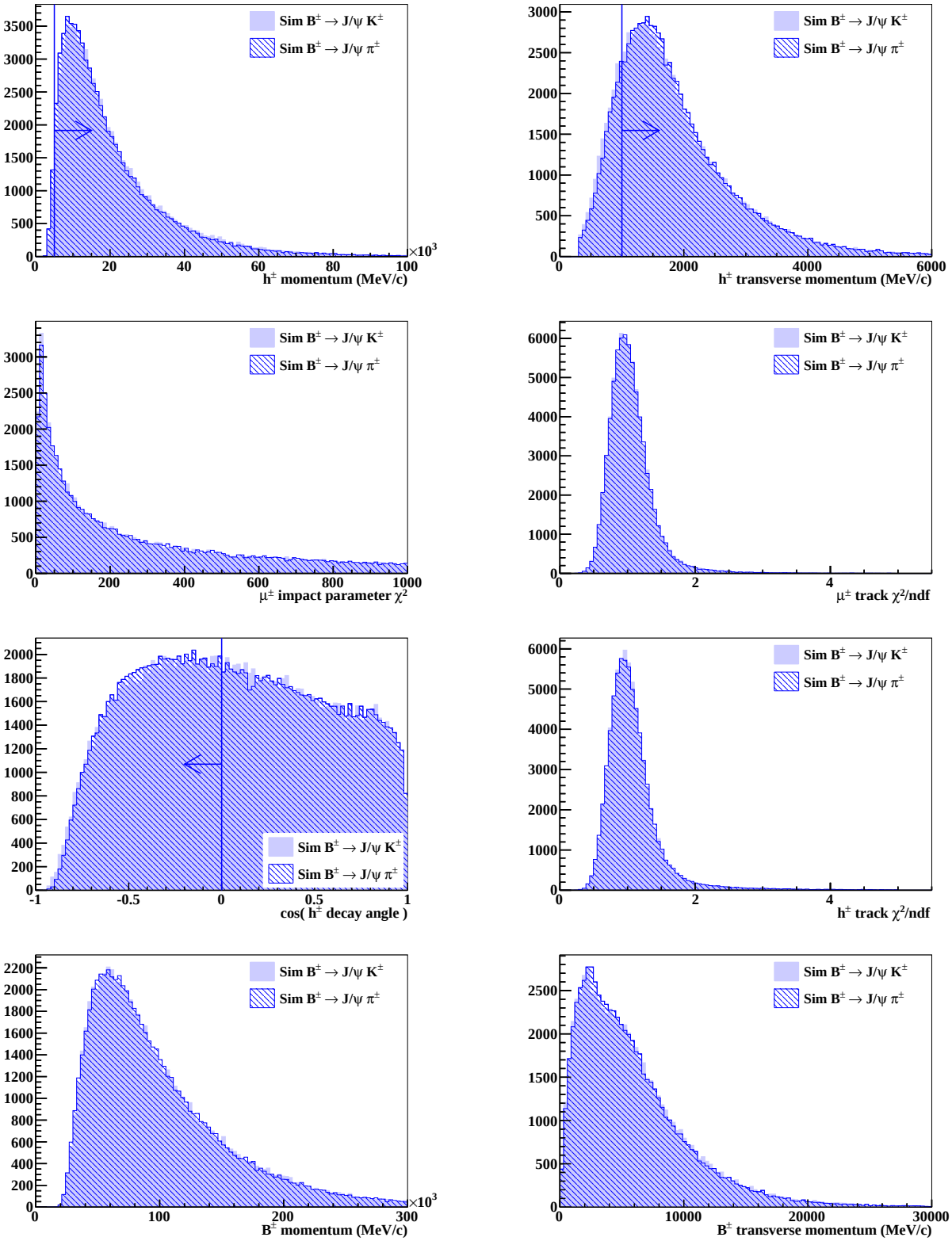

Figure 3.4: Comparison between selected $B^{\pm} \to J/\psi\,\pi^{\pm}$ and $B^{\pm} \to J/\psi\,K^{\pm}$ simulation. For details see Figure 3.3 caption.

3.2.1 Hadron decay angle

The hadron decay angle is defined as being the angle which the hadron makes to the direction of flight of the B, as measured in the rest frame of the B. A cut is made on this variable in the J/ψ modes, requiring that the hadron flies 'backwards' relative to the flight direction of the B. This results in the selected kaons having lower average momentum in the lab frame, and reconstructing these events with the incorrect mass hypothesis has the largest effect in the B invariant mass distribution (see Figure 3.5). The misreconstructed $J/\psi K^{\pm}$ background peak can therefore be separated from the signal $J/\psi \pi^{\pm}$ peak

In the $\psi(2S)$ modes, a selection on hadron decay angle is not made. The hadron in these channels is, on average, slower than the hadron in the J/ψ modes, due to the heavier ψ resonance. Therefore, the signal and background peaks are already sufficiently separated for the invariant mass fit to resolve the $\psi(2S)\pi^{\pm}$ signal from the misidentified $\psi(2S)K^{\pm}$ peak.

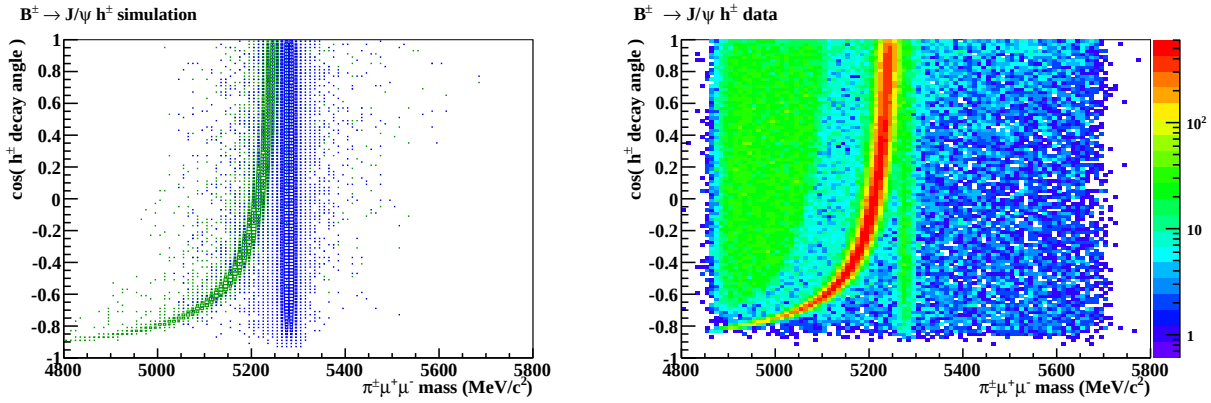

(a) (b)

Figure 3.5: Decay angle of the hadron vs. the reconstructed $\pi^{\pm}\mu^{+}\mu^{-}$ mass for: a) selected events from $B^{\pm} \to J/\psi K^{\pm}$ (green) and $B^{\pm} \to J/\psi \pi^{\pm}$ (blue) simulation. b) Selected events from data reconstructed as $B^{\pm} \to J/\psi \pi^{\pm}$. The green vertical band is the $J/\psi \pi^{\pm}$ component. The red (high statistics) curving band is $J/\psi K^{\pm}$ decays. The green region in the top left hand corner is partially reconstructed background.

3.2.2 Track clones

Track cloning describes the situation when the passage of one particle through the detector gives rise to two reconstructed tracks. In this case the two tracks will be associated to an almost identical set of hits in the reconstruction. Such duplicates are called clones and

although the LHCb reconstruction now removes them in an intelligent manner, in the early 2011 analyses the problem had to be handled by each analysis. A further complication can arise if one of the cloned tracks satisfies a different particle hypothesis to the first. Events containing track clones must be removed in order to prevent double, or mistaken, counting.

The $\psi(2S)$ analysis is affected most by track clones, which form a mass peak close to the B mass due to a kinematic coincidence of the decay. The affected events come about when the true track of a muon from a true ψ decay is cloned and reconstructed as a pion, so as to mimic the decay of interest. The two cloned tracks have essentially identical momentum measurements, so it can be shown that when the pion candidate is a clone of one of the two muons, the invariant mass of the B candidate is:

$$m_B \approx \sqrt{2m_\psi^2 + m_\pi^2 + (m_\pi^2 - m_\mu^2)\left(\frac{E_{\mu_1}}{E_{\mu_2}} + 1\right)}, \tag{3.3}$$

see Appendix B for a full derivation.

The two muons from the ψ decay have, on average, the same energy. Substituting measured mass values [49] into Equation 3.3, one finds that in the case of the J/ψ, cloning a muon track as a pion results in a B candidate of mass $\sim 4400\,\mathrm{MeV}/c^2$, well below the B mass range in this analysis. However, cloning a muon from a $\psi(2S)$ results in a B candidate with mass $60\,\mathrm{MeV}/c^2$ below the signal peak of $B^{\pm} \to \psi(2S)\pi^{\pm}$. The $\psi(2S)K^{\pm}$ mass distribution is not affected, as the muon is misidentified as a pion not a kaon. These calculations have been verified experimentally by forcing a track clone and misidentification to occur in the reconstruction.

To remove these track clone events from the $\psi(2S)$ analysis, a requirement is made that the invariant mass of the same-sign muon-hadron pair is greater than $300\,\mathrm{MeV}/c^2$. This is effective because the same sign muon and 'pion' tracks (having the same origin) are collinear, and so have invariant mass approximately equal to $m_\pi + m_\mu = 245\,\mathrm{MeV}/c^2$.

3.2.3 Trigger requirement

A requirement is also made of the way in which the event was triggered. In order to remove dependence on the hadron of the decay (π vs. K), it is required that the L0 trigger fired on the muons of the decay or on tracks other than the products of the B candidate under consideration. Typical L0 muon thresholds require that the muon transverse momentum be greater than 500 MeV/c [95]. An emulation of the hardware electronics of the L0 trigger is run on simulation to apply this requirement. Figure 3.1 shows the transverse momentum spectra of $\psi K^{\pm}$ and $\psi\pi^{\pm}$ final states are extremely similar, so any bias introduced by a threshold or inaccuracy of the emulation will be negligible. The trigger requirement retains 91.7% of the available data.

3.3 Signal extraction and correction strategy

The remainder of this chapter explains the line shapes, the mass fit, the corrections used to achieve the final result and the systematic issues. However it is beneficial at this point to give an overview of the strategy, to introduce and motivate the following sections.

In order to access the $B^{\pm} \to \psi\pi^{\pm}$ decays, particle identity information from the RICH detectors is used to split data into pion-like and kaon-like subsamples. This results in a visible $B^{\pm} \to \psi\pi^{\pm}$ peak in the pion-like subsample, which is isolated from the Cabbibo-favoured $B^{\pm} \to \psi K^{\pm}$ decays, see Figure 3.6(a). The remainder of the events are reconstructed as $B^{\pm} \to \psi K^{\pm}$, see Figure 3.6(b). This has the advantage that all selected $B^{\pm} \to \psi K^{\pm}$ events are retained, simplifying the normalisation of the Cabibbo-suppressed $B^{\pm} \to \psi\pi^{\pm}$.

Events are also split by the charge of the B meson, derived from the direction of track curvature measured by the spectrometer. This enables the charge asymmetry measurements. Due to differences seen in data recorded with the two magnet polarities (see Section 3.4), data is also partitioned by magnet polarity. In total therefore, eight subsamples are used.

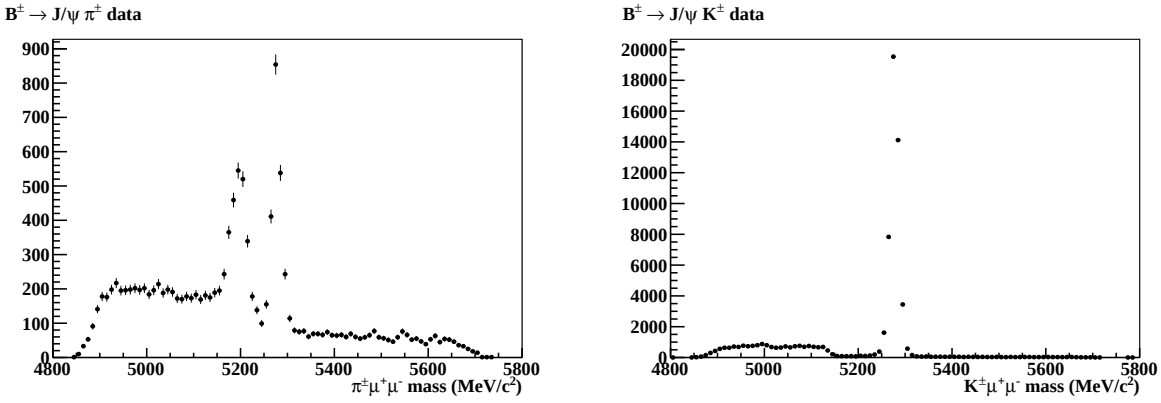

(a) (b)

Figure 3.6: Selected $B^{\pm} \to J/\psi h^{\pm}$ candidates partitioned by a requirement on hadron $\Delta \log \mathcal{L}(K-\pi)$. a) Pion-like events with $\Delta \log \mathcal{L}(K-\pi) < 6$, reconstructed as $B^{\pm} \to J/\psi\pi^{\pm}$. b) Kaon-like events with $\Delta \log \mathcal{L}(K-\pi) > 6$, reconstructed as $B^{\pm} \to J/\psi K^{\pm}$.

3.4 Signal lineshape

The shapes of the signal B mass peaks from $B^{\pm} \to J/\psi\pi^{\pm}$ and $B^{\pm} \to J/\psi K^{\pm}$ decays were studied in simulation. The events were selected in an identical way to data, and the B mass distributions were fitted with a modified Gaussian function:

$$f = \exp\left(\frac{-(x-\mu)^2}{g}\right),\ g = 2\sigma^2 + \alpha(x-\mu)^2,\ \alpha_{x<\mu} \neq \alpha_{x>\mu}\,, \tag{3.4}$$

with mean μ, width σ, and two α parameters which modify the tails. This allows the tails to be adjusted in a non-symmetric manner. Figure 3.7 shows that the peak is wider for $J/\psi\pi^{\pm}$ decays, 7.0 MeV/c^2 compared with 6.4 MeV/c^2 for $J/\psi K^{\pm}$ decays. This could be due to the higher energy available in $J/\psi\pi^{\pm}$ decays meaning these tracks have higher momentum, and hence worse momentum resolution and more final state radiation.

The signal peak shape is also studied in data. A clean sample of $B^{\pm} \to J/\psi K^{\pm}$ decays is selected using a $\Delta \log \mathcal{L}(K-\pi)$ cut to suppress $B^{\pm} \to J/\psi\pi^{\pm}$ decays, and is fitted with Equation 3.4. An additional linear polynomial function is used to describe the combinatorial background (see Section 3.5 for more details). Figure 3.8 shows the $B^{\pm} \to J/\psi K^{\pm}$ mass peak in data, both unconstrained and when the ψ mass is constrained to the nominal value (as is default in this analysis). Constraining the J/ψ mass reduces the B mass width by 10 MeV/c^2.

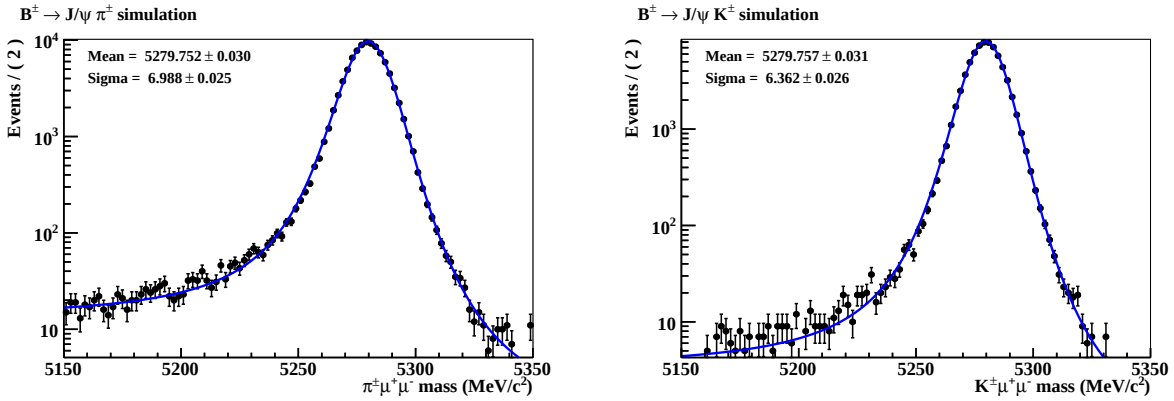

(a) (b)

Figure 3.7: Selected signal events from simulation samples. a) $B^{\pm} \to J/\psi\pi^{\pm}$ decays. b) $B^{\pm} \to J/\psi K^{\pm}$ decays. The distributions are fitted with a modified Gaussian lineshape, see Equation 3.4.

The constrained peak is $\sim 10\%$ wider than in simulation. By comparing the means of the fitted peaks, a mass shift of $2.2\,\mathrm{MeV}/c^2$ is seen between data and simulation. The constrained $\psi(2S)$ peak is found to be narrower than the constrained J/ψ peak, due to a larger fraction of the four momentum being constrained.

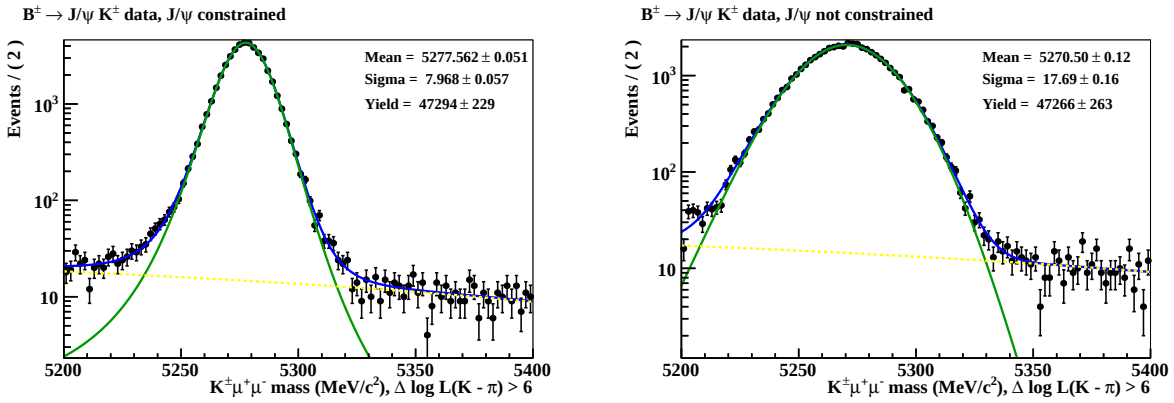

(a) (b)

Figure 3.8: $B^{\pm} \to J/\psi K^{\pm}$ mass spectrum in data. a) Constrained J/ψ mass, as used throughout this chapter. b) Non-constrained J/ψ mass.

The polarity of the LHCb magnet is regularly reversed during data taking, as described in Section 2.3. It is therefore interesting to compare four subsets of the data, split by the magnet polarity and the charge of the B meson. The width of the B peak is found to depend on the magnet polarity, and there is a $1\,\mathrm{MeV}/c^2$ mass shift between the different magnet polarities for B mesons of the same charge. This $1\,\mathrm{MeV}/c^2$ shift on a peak of width

7.7 MeV/c^2 is significant. Despite the separation of the $\psi\pi^{\pm}$ peak from the $\psi K^{\pm}$ background being good, data is split by magnet polarity in this analysis to allow for differences between the two samples, and to reduce the systematic uncertainty.

A comparison of the B mass peak parameters is made in Table 3.3. One value from this table is used as a fixed input to the signal extraction mass fit: the 2.2 MeV/c^2 mass shift seen between data and simulation is used to adjust the lineshape of a low-yield background component which is fixed from simulation, see Section 3.5.1.

Decay	Sample	Width (MeV/c^2)	Mean (MeV/c^2)	Δ_{mean} (MeV/c^2)
$B^{\pm} \to J/\psi\,\pi^{\pm}$	Simulation	6.99 ± 0.03	5279.8 ± 0.03	0
$B^{\pm} \to J/\psi\,K^{\pm}$	Simulation	6.36 ± 0.03	5279.8 ± 0.03	0
$B^{+} \to J/\psi\,K^{+}$	Down	7.90 ± 0.06	5276.9 ± 0.08	-2.9
$B^{-} \to J/\psi\,K^{-}$	Down	7.88 ± 0.06	5278.0 ± 0.08	-1.8
$B^{+} \to J/\psi\,K^{+}$	Up	7.78 ± 0.07	5278.2 ± 0.09	-1.6
$B^{-} \to J/\psi\,K^{-}$	Up	7.79 ± 0.07	5276.9 ± 0.07	-2.9
$B^{\pm} \to J/\psi\,K^{\pm}$	Combined	7.95 ± 0.06	5277.6 ± 0.05	-2.2
$B^{+} \to \psi(2S)K^{+}$	Down	6.19 ± 0.13	5277.3 ± 0.2	-2.5
$B^{-} \to \psi(2S)K^{-}$	Down	6.20 ± 0.14	5278.3 ± 0.2	-1.5
$B^{+} \to \psi(2S)K^{+}$	Up	6.42 ± 0.16	5278.3 ± 0.2	-1.5
$B^{-} \to \psi(2S)K^{-}$	Up	6.56 ± 0.16	5277.4 ± 0.2	-2.4
$B^{\pm} \to \psi(2S)K^{\pm}$	Combined	6.51 ± 0.12	5277.8 ± 0.1	-2.0

Table 3.3: B mass peak comparison between the two simulated signal samples and $B^{\pm} \to \psi K^{\pm}$ decays in data. The ψ mass is constrained. 'Down' and 'Up' refer to the magnet polarity used during data recording.

3.5 Backgrounds

To successfully analyse properties of $\psi\pi^{\pm}$ decays, several backgrounds must be addressed:

- kinematically similar $B^{\pm} \to \psi K^{\pm}$ decays, where the hadron is misidentified;
- partially reconstructed backgrounds from $B \to \psi X$ and $B_s \to \psi X$ decays;
- combinatorial background.

Each one of these backgrounds is accounted for by a component in the signal extraction fit. The different categories of background are now explained in detail.

3.5.1 Misidentified hadron peaking background

The data are split into pion-like and kaon-like subsamples by a $\Delta \log \mathcal{L}(K-\pi)$ selection on the hadron. A high value of $\Delta \log \mathcal{L}(K-\pi)$ is chosen to be efficient for $\psi\pi^{\pm}$; almost 100% of $\psi\pi^{\pm}$ decays are in the pion-like subsample. Therefore, many kaons will also enter the pion-like subsample. A small fraction ($\sim 4\%$) of pions will enter the kaon-like subsample.

Misidentified events are reconstructed with the wrong mass hypothesis, which results in this background either peaking at lower mass in the case of $\psi K^{\pm}$ misidentified as $\psi\pi^{\pm}$ events, or at higher mass in the contrary case. The shapes of these background peaks are studied in simulation. The reconstructed mass distributions are shown in Figure 3.9, each fitted with a Crystal Ball function [96]. These shapes are determined by the momentum distribution of the misidentified hadrons, and so are influenced by the selection on the decay angle of the hadron, and by the choice of $\Delta \log \mathcal{L}(K-\pi)$ as both alter the accepted momentum spectrum.

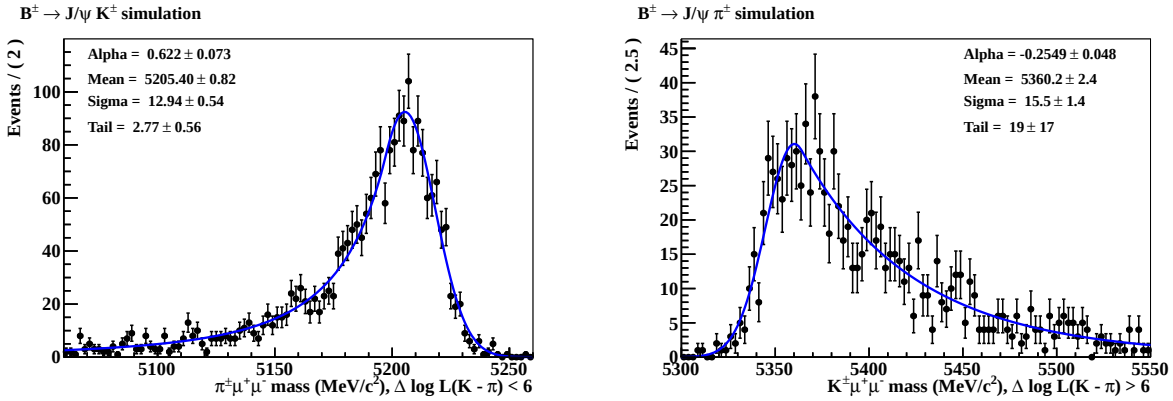

(a) (b)

Figure 3.9: a) Selected pion-like events from $B^{\pm} \to J/\psi K^{\pm}$ simulation with $\Delta \log \mathcal{L}(K-\pi) < 6$, fitted with a Crystal Ball shape. b) Selected kaon-like events from $B^{\pm} \to J/\psi \pi^{\pm}$ simulation with $\Delta \log \mathcal{L}(K-\pi) > 6$, also fitted with a Crystal Ball shape.

3.5.2 Partially reconstructed backgrounds

Partially reconstructed decays enter the analysis in the low-mass region. $B \to \psi h h^{(0)}$ decays, where the extra hadron is not reconstructed, can pass the selection but will have a reduced B mass due to the missing four momentum.

Background from B decays

$B \to \psi\rho(\to \pi\pi)$ and $B \to \psi K^*(\to K\pi)$ decays can both contribute to the partially reconstructed background. There are four possible situations in which this can occur. Either a pion or kaon can be omitted from the reconstruction of the final state. Missing a kaon results in a lower reconstructed B mass than missing a pion. In addition to these two possibilities, the reconstructed hadron can be correctly identified or not. This results in a further mass shift to the reconstructed B candidate.

The situation was studied using a simulated sample of $B^0 \to J/\psi K^{*0}$ events. The effect of missing a $\pi^{(0)}$ from the decay of a B can be approximated by reconstructing $B^0 \to J/\psi K^{*0}(\to K\pi)$ as $B^{\pm} \to J/\psi K^{\pm}$. The effect of missing a $K^{(0)}$ is modelled by reconstructing $B^0 \to J/\psi K^{*0}(\to K\pi)$ as $B^{\pm} \to J/\psi \pi^{\pm}$. Figure 3.10(a) shows all four possible mass distributions:

- In dark green: $B^{\pm} \to J/\psi K^{\pm}$ is correctly reconstructed, meaning the pion was missed from the decay. This is considered analogous to the case where a pion is missed from the $B^0 \to J/\psi \rho^0(\to \pi\pi)$ background.
- In light green: $B^{\pm} \to J/\psi K^{\pm}$ is reconstructed as $B^{\pm} \to J/\psi \pi^{\pm}$, meaning the pion was missed from the decay and the kaon has been assigned a pion mass.
- In dark red: $B^{\pm} \to J/\psi \pi^{\pm}$ is correctly reconstructed, meaning the kaon is missed.
- In light red: $B^{\pm} \to J/\psi \pi^{\pm}$ is reconstructed as $B^{\pm} \to J/\psi K^{\pm}$, meaning the kaon is missed and the pion has been assigned a kaon mass.

As can be seen from Figure 3.10(a), missing a kaon (red lines) in the reconstruction of the decay means that so much mass is lost, the B meson will almost always fall below the mass range required by the stripping selection (see Table 3.1). Therefore, partially reconstructed backgrounds where a kaon is missed are not considered further.

The green lines in Figure 3.10(a) show the cases where a pion is missed. Events in which the kaon is correctly identified will certainly enter the kaon-like subsample. The selected mass distribution of these events can be seen in Figure 3.10(b). When the kaon is misidentified

as a pion, the event will fall into the pion-like subsample. However, the misidentification fraction is small and so these events are not expected to feature.

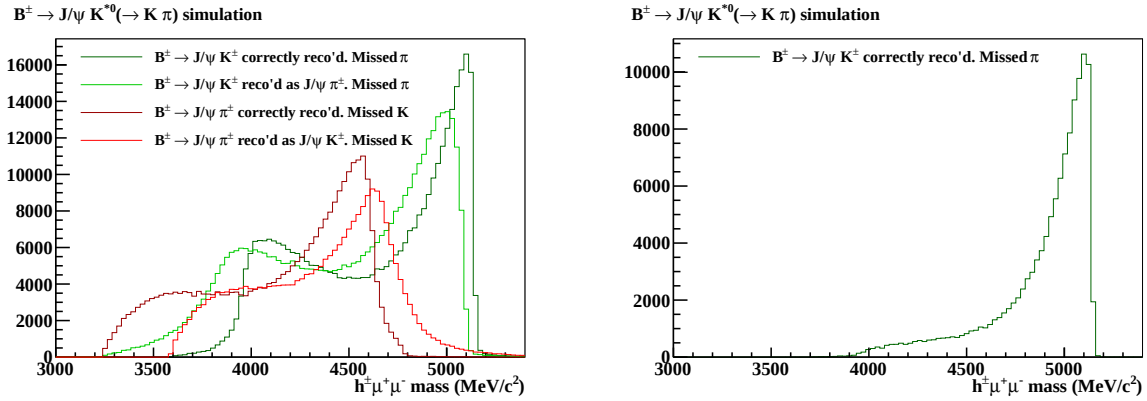

(a) (b)

Figure 3.10: Various reconstructions of $B^0 \to J/\psi\, K^{*0}(\to K\pi)$ simulation, see text for details. a) All simulated events. b) Simulated events which pass the selection. This is the only partially reconstructed background shape considered for B decays.

The selected distribution of $B^0 \to J/\psi\, K^{*0}(\to K\pi)$ decays reconstructed as $B^\pm \to J/\psi\, K^\pm$ is fitted with a bifurcated Gaussian, seen in Figure 3.11(a). This is used in the fit to model contributions from partially reconstructed $B \to \psi K^*(\to K\pi)$ and $B \to \psi\rho(\to \pi\pi)$ decays.

From B_s decays

$B_s \to \psi f(\to \pi\pi)$, $B_s \to \psi K^*(\to K\pi)$ and $B_s \to \psi\phi(\to KK)$ were also considered as partially reconstructed backgrounds. The B_s is 87 MeV/c^2 heavier than the B, which again means that missing a kaon from the decay shifts the reconstructed B mass below the range of interest. A $B_s^0 \to J/\psi\,\phi(\to KK)$ simulation sample was checked, and as expected no background was seen from this source.

Simulated $B_s^0 \to J/\psi\, f^0(\to \pi\pi)$ decays were reconstructed as $B^\pm \to J/\psi\,\pi^\pm$, shown in Figure 3.11(b). The distribution has been fitted with a bifurcated Gaussian. This shape is equated to the mass distribution from $B_s^0 \to J/\psi\, K^{*0}(\to K\pi)$ where the kaon is reconstructed and the pion is missed.

Relative yields The contributions from $B^0 \to \psi\rho^0(\to \pi\pi)$ and $B_s^0 \to \psi f^0(\to \pi\pi)$ have similar yields. Their expected ratio was calculated using the branching fraction of each

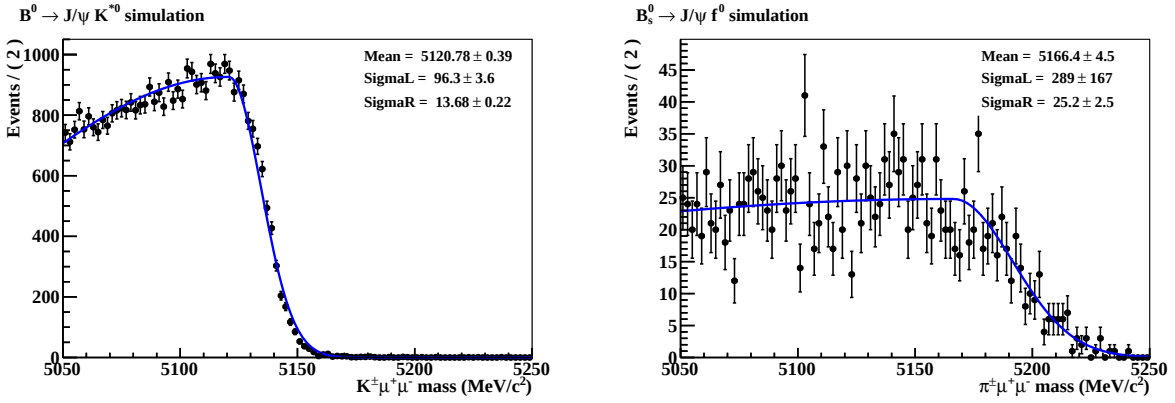

(a) (b)

Figure 3.11: Selected simulated events are fitted with a bifuricated Gaussian. a) $B^0 \to J/\psi\, K^{*0}(\to K\pi)$ simulation reconstructed as $B^{\pm} \to J/\psi\, K^{\pm}$. b) $B_s^0 \to J/\psi\, f^0(\to \pi\pi)$ simulation reconstructed as $B^{\pm} \to J/\psi\, \pi^{\pm}$. These shapes are propagated to the signal extraction fit to data.

decay, the observed fraction of the mass spectrum (see Table 3.4), and the $b\bar{b}$ hadronisation fraction:

$$f_s/f_d = 0.253 \pm 0.017\ (stat) \pm 0.017\ (syst) \pm 0.020\ (theo)\ [97]\,. \tag{3.5}$$

Decay	Branching fraction	Selected
$B_s^0 \to J/\psi\, f^0(\to \pi\pi)$	$(1.29 \pm 0.4) \times 10^{-4}$ [49]	0.312
$B^0 \to J/\psi\, \rho^0(\to \pi\pi)$	$(2.7 \pm 0.4) \times 10^{-5} \times (98.90 \pm 0.16) \times 10^{-2}$ [98, 49]	0.281

Table 3.4: Relative yield calculation of pion-like partially reconstructed backgrounds in the pion-like subsample, showing the branching fraction of relevant decays, and the fraction of selected events above the lower mass limit.

The expected ratio of the yields of the two backgrounds is calculated to be:

$$\frac{N_{B_s^0 \to J/\psi\, f^0}}{N_{B^0 \to J/\psi\, \rho^0}} = 0.253 \times \frac{1.29 \times 10^{-4}}{2.7 \times 10^{-5} \times 98.90 \times 10^{-2}} \times \frac{0.312}{0.281} = 1.36 \pm 0.50\,, \tag{3.6}$$

where it is assumed that these two $J/\psi\,\pi\pi$ final states have the same acceptance and reconstruction efficiencies. This ratio is a fixed input in the final signal extraction fit.

3.5.3 Combinatorial background

To assess the behaviour of the combinatorial background, sidebands were consulted. Two windows of 350 MeV/c^2 were considered, where each window was placed away from dimuon

resonances, one above the J/ψ mass and one below. The B mass spectrum in each window is shown in Figure 3.12, here both mass distributions are fitted with a linear function. Despite the gradient of the slope changing, the combinatorial background is found to be linear to good approximation, a strong exponential rise is not observed.

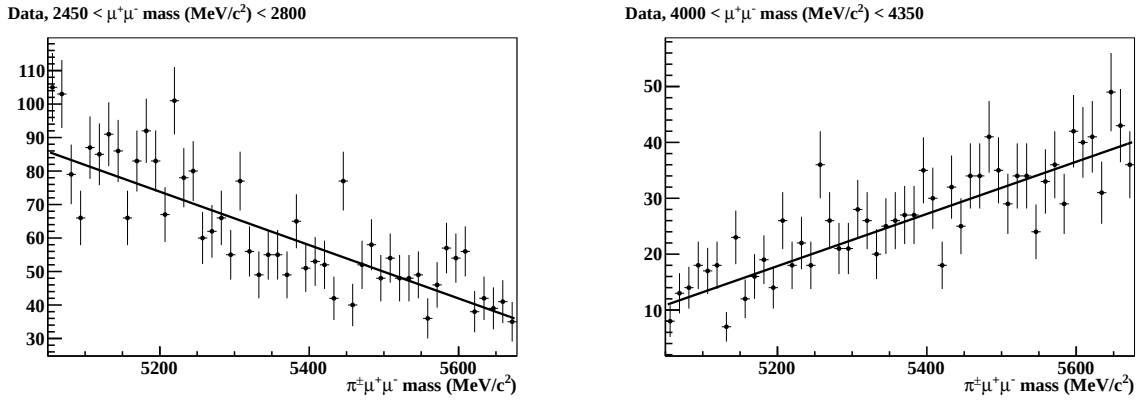

(a) (b)

Figure 3.12: Invariant mass spectra of $\psi(\mu^+\mu^-)\pi^\pm$ candidates in the dimuon mass sidebands. a) $2450 < \mu^+\mu^-$ mass $(\,\mathrm{MeV}/c^2) < 2800$. b) $4000 < \mu^+\mu^-$ mass $(\,\mathrm{MeV}/c^2) < 4350$.

3.6 Signal extraction fit

Results are extracted with a maximum likelihood fit (using RooFit [99]). The fit is constructed so that observables of interest are parameters of the fit, such that the error reported by Minuit can be taken directly as the statistical error on each quantity.

3.6.1 Description of the fitter

For either ψ resonance considered, there are two measurements of interest:

- the ratio between the number of $B^\pm \to \psi\pi^\pm$ and $B^\pm \to \psi K^\pm$ decays (R^{ψ}_{Raw});
- the normalised difference between the number of $B^- \to \psi h^-$ and $B^+ \to \psi h^+$ decays ($A^{\psi h}_{Raw}$);

These can be accessed by performing a 1D-fit of the B mass distribution of each mode considered in the analysis, and counting the number of events in each peak. $B^\pm \to \psi\pi^\pm$ is

separated from $B^{\pm} \to \psi K^{\pm}$ with a $\Delta \log \mathcal{L}(K-\pi)$ selection which splits events into pion-like and kaon-like subsamples. Sensitivity to charge asymmetries is achieved by splitting both the pion-like and kaon-like subsamples into B^{+} and B^{-}. Finally, data are split into magnet polarity subsamples corresponding to magnet up and magnet down. This results in eight subsamples which are fit simultaneously in an unbinned manner.

Each subsample has five components:

1. Correctly reconstructed $B^{\pm} \to \psi h^{\pm}$: the modified Gaussian function of Equation 3.4 is used. The origin of the width of this function is the accuracy of the momentum determination in the spectrometer. The fit parameters float freely, except for α_L. There is some fit instability in the left tail of the $B^{\pm} \to \psi h^{\pm}$ signal peaks, so the α_L parameter is fixed in the kaon-like subsample to 0.1128 (derived from data as seen in Figure 3.8). In the pion-like subsample this fixed parameter is adjusted by the ratio of α_L^K/α_L^π found from simulation.

2. Misidentified $B^{\pm} \to \psi h^{\pm}$: a Crystal Ball shape is used to account for the tails resulting from the incorrect mass-hypothesis in the reconstruction, see Section 3.5.1. The mean, sigma and yield of the Crystal Ball shape in the pion-like subsample are allowed to float freely, however the tail parameters are fixed. This is to prevent interference between this shape and the partially reconstructed background. The Crystal Ball shape in the kaon-like subsample is completely fixed to the parameters seen in Figure 3.9, with the addition of a 2.2 MeV/c^2 mass shift due to simulation-data differences (see Table 3.3).

   A small number of misidentified pions (typically a handful of events) are hidden under the large kaon signal peak. The fraction of pion events which fall into the kaon-like subsample is fixed from data using the following steps. First, the fraction of pions selected by the RICH particle identification requirement is determined. Then, one minus this fraction is the fraction of pions misidentified as kaons, which contribute to the kaon-like subsample. The background yield is calculated by normalising this misidentification fraction by the fitted number of correctly identified $\psi\pi^{\pm}$ events.

To determine the fraction of pions which are selected by the RICH particle identification requirement, a calibration was performed using a clean D^0 sample from $B^\pm \to D^0(\to K^\pm\pi^\mp)\pi^\pm$ decays. Only events within $25\,\mathrm{MeV}/c^2$ of $m_{D^0} = 1864\,\mathrm{MeV}/c^2$ are considered. The momentum spectrum of the pion from $D^0 \to K^\pm\pi^\mp$ in data was separately reweighted to match the momentum spectrum of the pion from $B^\pm \to J/\psi\,\pi^\pm$ and $B^\pm \to \psi(2S)\pi^\pm$ simulation. These weights were then applied to the $\Delta\log\mathcal{L}(K-\pi)$ spectrum of the pion from $D^0 \to K^\pm\pi^\mp$ in data. The fraction of the $\Delta\log\mathcal{L}(K-\pi)$ spectrum retained by applying a cut at $\Delta\log\mathcal{L}(K-\pi) > 6$ was calculated for the two ψ modes:

$$\begin{aligned} \epsilon_{J/\psi\,\pi}(\Delta\log\mathcal{L}(K-\pi) > 6) &= (4.2 \pm 1.0)\% \\ \epsilon_{\psi(2S)\pi}(\Delta\log\mathcal{L}(K-\pi) > 6) &= (3.4 \pm 1.0)\%\,. \end{aligned} \tag{3.7}$$

These efficiencies are fixed in the fit to data, and an appropriate systematic assigned.

3. Partially reconstructed backgrounds from B decays: $B \to \psi K\pi$ and $B \to \psi\pi\pi$. $B^0 \to \psi K^{*0}(\to K\pi)$ is a relatively prevalent decay and many events are expected in the kaon-like subsample. A bifurcated Gaussian function is used to fit this component, where the parameters and yield are allowed to float in the kaon-like subsample. The shape of $B^0 \to \psi\pi\pi$ in the pion-like subsample is fixed from $B^0 \to J/\psi\,\rho^0$ simulation, see Section 3.5.2.

4. Partially reconstructed backgrounds from B_s decays: $B_s \to \psi K^*$ and $B_s \to \psi f$. $B_s^0 \to \psi K^{*0}(\to K\pi)$ has a small yield in comparison to $B^0 \to \psi K^{*0}$ in the kaon-like subsample. The shape of this function is fixed, and its yield allowed to float. $B_s^0 \to \psi f^0$ events enter the pion-like subsample with approximately equal yield as $B^0 \to \psi\rho^0$. The ratio of yields from these two sources is fixed at 1.36 ± 0.50, see Section 3.5.2.

5. Combinatorial background has been shown to be linear, see Section 3.5.3. The gradient of the PDF floats in the fit to data, and is determined by the long tail in the high B mass region.

Results of the fit are shown in four plots, presented in 2×2 format where the polarity split has been suppressed for ease of display (i.e. data recorded under both magnet polarities appear in the same histogram). The top row of plots show the pion-like events, the bottom row contains kaon-like events. On the left are B^- events, on the right are B^+ events. Each plot contains various PDF shapes, each describing a certain component of the dataset (signal, background etc):

1. Solid red line: $B^{\pm} \to \psi\pi^{\pm}$ events. A signal peak in the pion-like subsample, an almost invisible Crystal Ball shape in the kaon-like subsample.

2. Solid green line: $B^{\pm} \to \psi K^{\pm}$ events. A large signal peak in the kaon-like subsample, a Crystal Ball in the pion-like subsample of comparable yield to the $\psi\pi$ peak.

3. Shading: Partially reconstructed background from B and B_s decays.

Combinatorial background is described by a linear function which is not shown. The sum of all component PDFs is shown by the solid blue line.

3.6.2 Multiple candidates

If two or more candidates exist within the same event, and the B decay vertex positions are within 2 mm of each other in z, then the candidate with the best B decay vertex χ^2 is kept and the other candidate(s) removed from the sample.

In the J/ψ analysis 1.2% of events are rejected as multiple candidates. 7.1% of events are rejected from the $\psi(2S)$ analysis; this increase is probably due to the higher combinatorial background level in this mode, due in turn to the slightly relaxed selection. The mass spectrum of removed J/ψ candidates is shown in Figure 3.13. The peaking nature of the rejected distribution suggests that most of the multiple candidates are due to track clones, where two tracks have been reconstructed from almost the same collection of hits in the tracking detectors (see Section 3.2.2). This figure also shows that candidate removal based on B decay vertex χ^2 gives no significant bias to the relative retention of $\psi\pi^{\pm}$ vs. $\psi K^{\pm}$ final states.

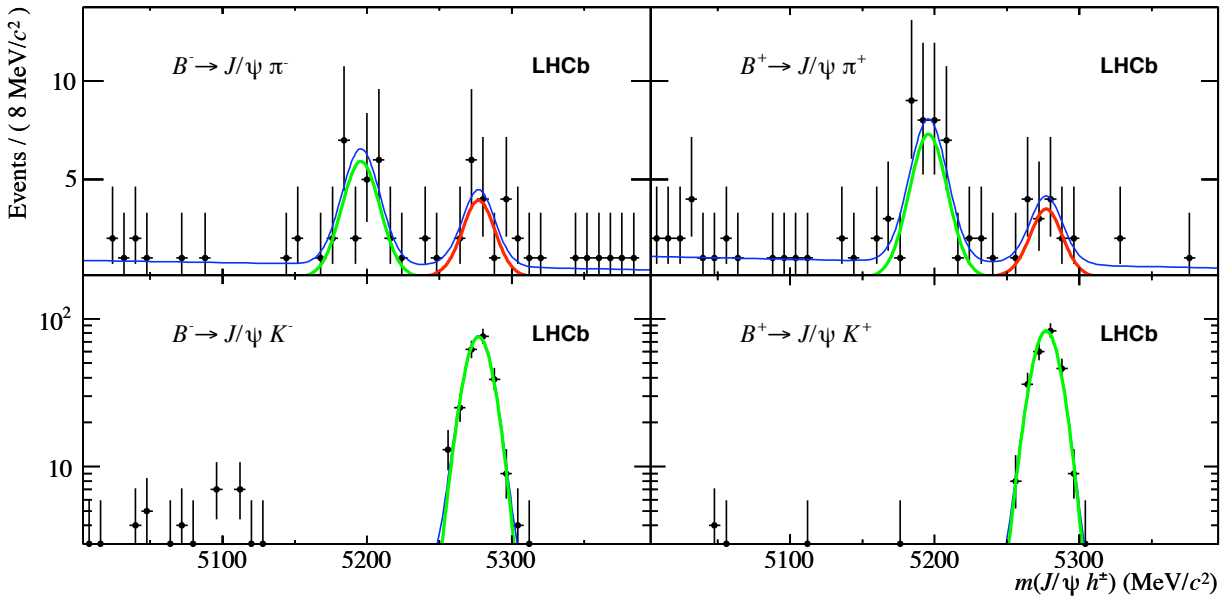

Figure 3.13: Fit applied to the removed multiple candidates in the J/ψ analysis. For a description of the fit, or multiple candidate removal process, see text.

3.6.3 Stability of the fit

The stability of the fit is tested by generating and fitting a large sample of pseudo-experiments with parameters close to those measured in data. Pull distributions of the floating fit parameters from 1000 toy experiments are shown in Figures 3.14 and 3.15. These are broadly consistent with a Gaussian of mean zero and unit width (a normal distribution), demonstrating that the fit is stable under statistical variation of total number of events.

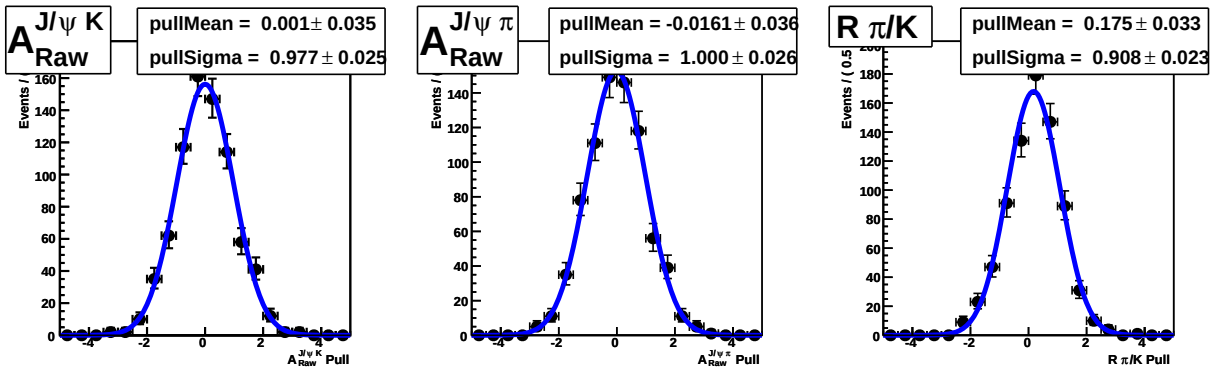

Figure 3.14: Pull distributions for variables of interest in the J/ψ analysis.

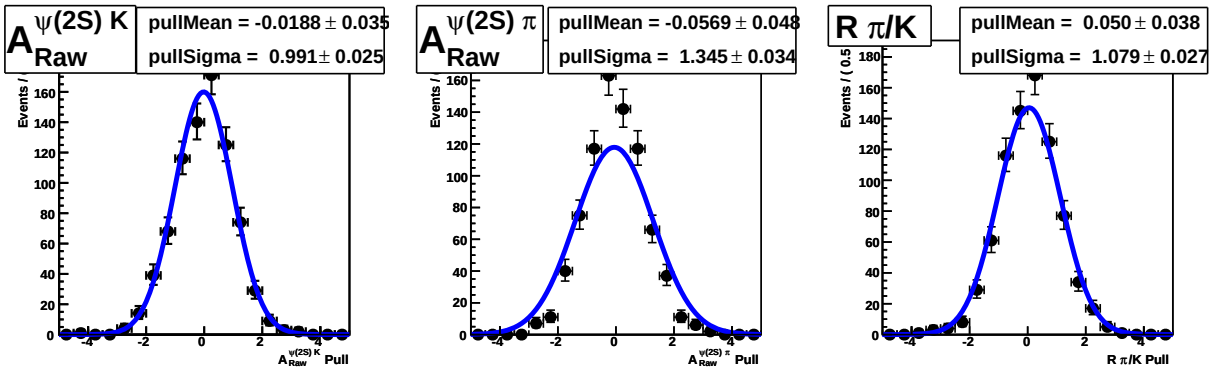

Figure 3.15: Pull distributions for variables of interest in the $\psi(2S)$ analysis. The fit to the $A_{Raw}^{\psi(2S)\pi}$ pull plot (centre) has been thrown off by an outlier, but one sees that the underlying distribution of toys is good.

3.6.4 Raw measurements

Fitted data in the J/ψ and $\psi(2S)$ analyses are shown in Figures 3.16 and 3.17. Fitted yields are shown in Table 3.5.

			B^-	B^+
J/ψ	π	Down	528 ± 27	518 ± 27
		Up	421 ± 23	428 ± 23
	K	Down	$13\,363 \pm 180$	$13\,466 \pm 181$
		Up	$10\,666 \pm 148$	$11\,120 \pm 155$
$\psi(2S)$	π	Down	94 ± 16	93 ± 16
		Up	82 ± 15	70 ± 13
	K	Down	$2\,331 \pm 88$	$2\,463 \pm 93$
		Up	$2\,026 \pm 78$	$1\,836 \pm 71$

Table 3.5: Raw fitted yields. The labels 'Down' and 'Up' refer to the two polarities of the magnet. The magnet down sample corresponds to $200\,\text{pb}^{-1}$, the magnet up sample $170\,\text{pb}^{-1}$.

3.7 Corrections

The observables R_{Raw}^{ψ} and $A_{Raw}^{\psi h}$ are taken from the fit, and must be corrected by efficiency factors and additional asymmetries in order to access the physics variables of interest. These corrections are now discussed.

The raw ratio of branching fractions taken from the fit must be corrected to take into account the relative geometric acceptance efficiency (ω_{acc}^{ψ}), the relative reconstruction and

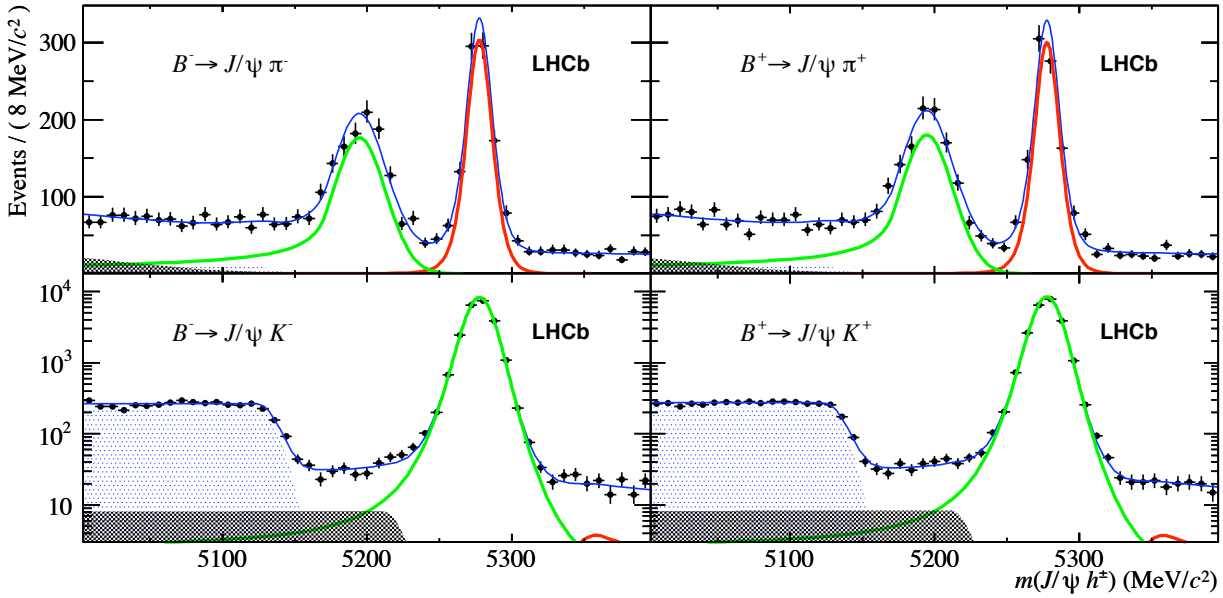

Figure 3.16: $B^\pm \to J/\psi h^\pm$ invariant mass distributions, overlain by the total fitted PDF (thin line). Pion-like events, with $\Delta \log \mathcal{L}(K-\pi) < 6$ are reconstructed as $J/\psi\pi^\pm$ and enter in the top plots. All other events are reconstructed as $J/\psi K^\pm$ and are shown in the bottom plots on a logarithmic scale. B^- decays are shown on the left, B^+ on the right. The dark (red) curve shows the $B^\pm \to J/\psi\pi^\pm$ component, the light (green) curve represents $B^\pm \to J/\psi K^\pm$. The partially reconstructed contributions are shaded. In the lower plots these are visualised with a dark (light) shade for B^0_s (B^+ or B^0) decays. In the top plots the shaded component are contributions from $B \to J/\psi K^\pm\pi$ (dark) and $B \to J/\psi\pi^\pm\pi$ (light).

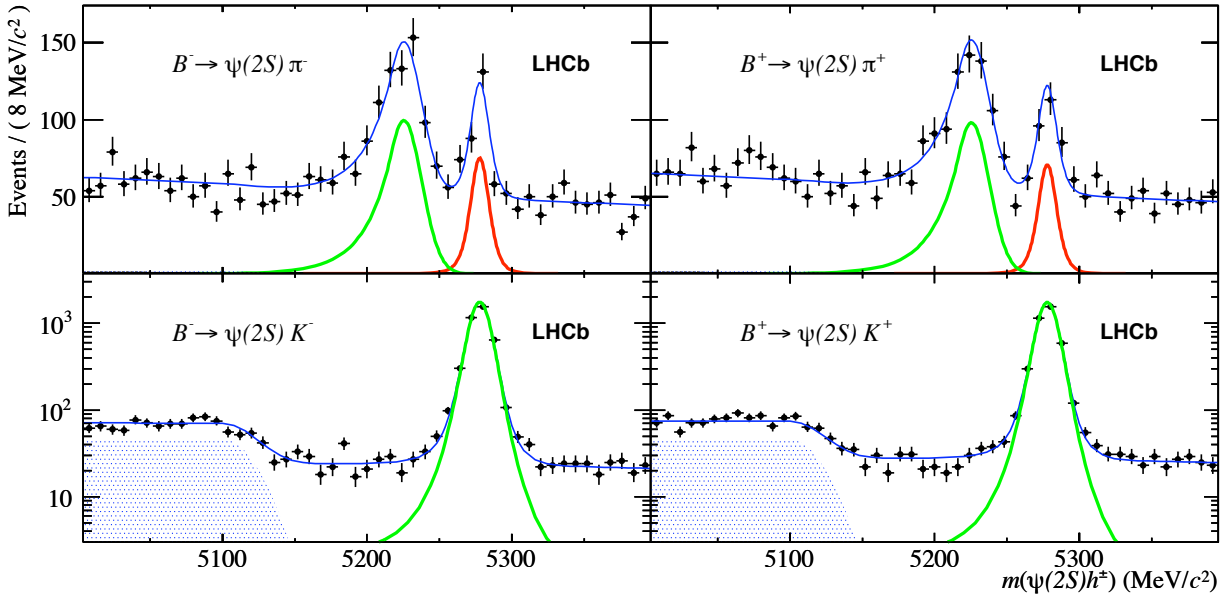

Figure 3.17: $B^\pm \to \psi(2S)h^\pm$ invariant mass distributions. For details see Figure 3.16 caption.

selection efficiency (ω^{ψ}_{sel}), and the relative trigger efficiency (ω^{ψ}_{trig}) of the decays in question:

$$R^{\psi} = R^{\psi}_{Raw}\, \omega^{\psi}_{acc}\, \omega^{\psi}_{sel}\, \omega^{\psi}_{trig}\,, \tag{3.8}$$

where the relative efficiency is the ratio of the efficiencies (ϵ) of the two modes:

$$\omega^{\psi} = \frac{\epsilon(B^{\pm} \to \psi K^{\pm})}{\epsilon(B^{\pm} \to \psi\pi^{\pm})}\,. \tag{3.9}$$

These corrections are now explained in detail.

3.7.1 Relative acceptance efficiency, ω^{ψ}_{acc}

The acceptance efficiency (ϵ_{acc}) measures the probability that a certain type of decay will occur within the acceptance of LHCb. In each ψ analysis, the ratio of acceptance efficiencies is calculated. They are expected to be close to one, as the only difference between the two decays is the hadron type. It was already shown (in Section 3.1.2) that $B^{\pm} \to \psi K^{\pm}$ and $B^{\pm} \to \psi\pi^{\pm}$ are kinematically very similar.

A stand-alone generator level study was performed to produce samples of the four decay modes, using Pythia [100] to generate the pp collision, and EvtGen [69] to model the B meson decay. As the decays in question are of type 'scalar to vector scalar', the SVS model of EvtGen was used. Figure 3.18 shows the generated pseudorapidity, η, of the hadron in the J/ψ and $\psi(2S)$ channels. (Hadron η is considered as this is the primary difference between the decays driving ω^{ψ}_{acc}.) The blue lines correspond to the limits of the LHCb acceptance ($1.6 < \eta < 5.3$). In both ψ analyses, the kaon distribution peaks at slightly higher η than the pion distribution, meaning that more kaon events decay inside the LHCb acceptance. Pions are more likely to be lost to the outside of LHCb, because the extra kinetic energy available to this decay increases the transverse momentum of the daughters.

Additional plots were made, requiring that all three daughter particles were within the LHCb acceptance. The hadron distribution in this case can be seen in Figure 3.19. From the statistics shown in Figures 3.18 and 3.19 it is calculated that the acceptance efficiency

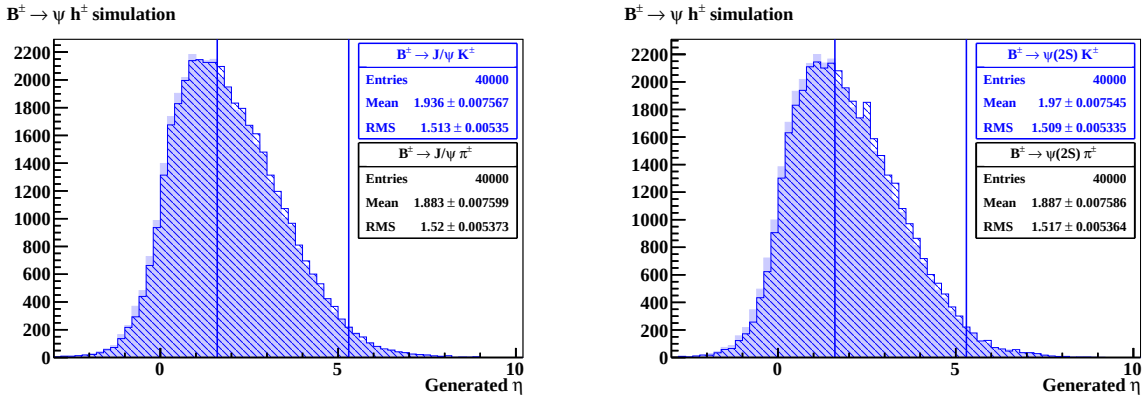

(a) (b)

Figure 3.18: Generated η distribution of the hadron for $B^{\pm} \to \psi K^{\pm}$ (hashed) and $B^{\pm} \to \psi \pi^{\pm}$ (shaded). a) J/ψ modes. b) $\psi(2S)$ modes. The blue lines show the acceptance of LHCb. In both cases, kaons have a slightly higher η than pions, perhaps causing them to be accepted more often within LHCb.

corrections are:

$$\begin{aligned} \omega_{acc}^{J/\psi} &= 1.038 \pm 0.011 \\ \omega_{acc}^{\psi(2S)} &= 1.052 \pm 0.011\,. \end{aligned} \tag{3.10}$$

The statistical uncertainties on the acceptance efficiencies are taken to be binomial:

$$\sigma(\epsilon) = \frac{\sqrt{m(1-m/N)}}{N}\,, \tag{3.11}$$

where N is the total number of generated events, and m is the number of events which pass the LHCb acceptance selection.

3.7.2 Relative reconstruction and selection efficiency, ω_{sel}^{ψ}

The reconstruction and selection efficiency (ϵ_{sel}) of each decay of interest is measured from simulation, which consists of a bespoke simulation of LHCb based on GEANT4 [101]. Two samples were considered: $B^{\pm} \to J/\psi\, K^{\pm}$ and $B^{\pm} \to J/\psi\, \pi^{\pm}$ where the daughter particles are required to be within the LHCb acceptance. The generated events are stripped, reconstructed and then selected, the progression is shown in Table 3.6 for both the J/ψ and $\psi(2S)$ modes, to take into account their different selections.

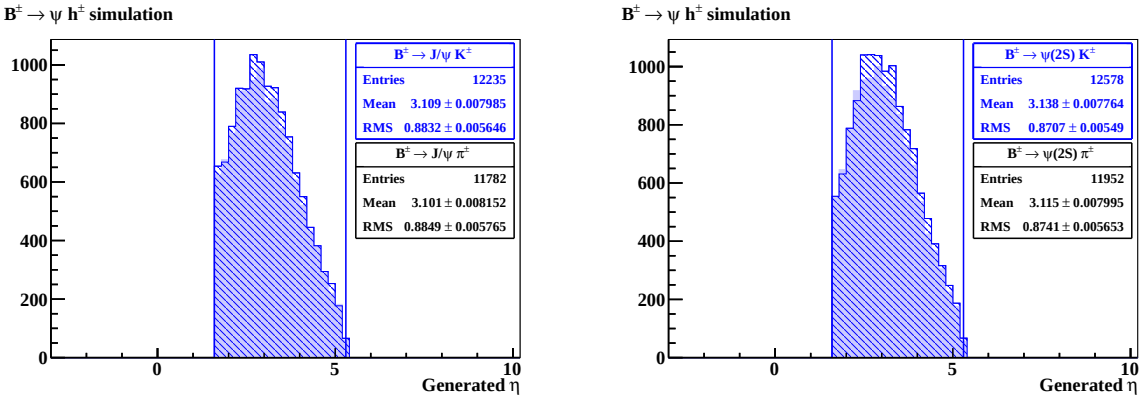

(a) (b)

Figure 3.19: As Figure 3.18, but here all three daughter particles are required to be within the LHCb acceptance. The overflow of events at $\eta = 5.3$ is due to binning. The bin width is 0.1946.

	$B \to J/\psi\pi$ (%)	$B \to J/\psi K$ (%)	$B \to \psi(2S)\pi$ (%)	$B \to \psi(2S)K$ (%)
Generated	1317990	1023988	1317990	1023988
Pass 2011 stripping	352068 (26.7)	263203 (25.7)	352068 (26.7)	263203 (25.7)
Selection	246588 (70.0)	182355 (69.3)	276415 (78.5)	204808 (77.8)
ψ mass	232582 (94.3)	172000 (94.3)	260835 (94.4)	193249 (94.4)
$\Delta \log \mathcal{L}(K-\pi)$	231456 (99.5)	172000 (100)	259670 (99.6)	193249 (100)
Trigger	210963 (91.2)	156684 (91.1)	235922 (90.9)	175556 (90.8)
Decay angle	98312 (46.6)	72779 (46.5)	-	-
Efficiency	0.0746	0.0711	0.179	0.171
Sim stat. error	2.29×10^{-4}	2.54×10^{-4}	3.34×10^{-4}	3.72×10^{-4}
Efficiency ratio	0.953 ± 0.004		0.958 ± 0.003	

Table 3.6: J/ψ and $\psi(2S)$ selection efficiencies taken from simulated samples of $B^{\pm} \to J/\psi K^{\pm}$ and $B^{\pm} \to J/\psi\pi^{\pm}$. The $\Delta \log \mathcal{L}(K-\pi)$ line checks for a physical value of this variable. All kaons pass, some pions fail as this is the default mass hypothesis.

The reconstruction and selection efficiency corrections for the two analyses are therefore:

$$\begin{aligned} \omega^{J/\psi}_{sel\,(uncorrected)} &= 0.953 \pm 0.004 \\ \omega^{\psi(2S)}_{sel\,(uncorrected)} &= 0.958 \pm 0.003\,, \end{aligned} \tag{3.12}$$

where the statistical uncertainties are taken to be binomial (see Eq. 3.11). Several corrections must be applied to these factors, now explained in detail.

- **Correction due to the $\Delta \log \mathcal{L}(K-\pi)$ cut in simulation**

  The kaon stripping lines in 2010 and 2011 used slightly different $\Delta \log \mathcal{L}(K-\pi)$ selections, see Table 3.1. The selection efficiencies must be corrected to take this into account.

  A second sample of $B^{\pm} \to J/\psi\, K^{\pm}$ was simulated and selected, removing the $\Delta \log \mathcal{L}(K-\pi)$ requirement. It was calculated that $(99.37 \pm 0.03)\%$ of the J/ψ mode, and $(98.29 \pm 0.04)\%$ of the $\psi(2S)$ mode, is selected by the stripping cut of $\Delta \log \mathcal{L}(K-\pi) > -1$. The efficiencies shown in Equation 3.14 are divided by these percentages to take this into account.

- **Correction due to the $\Delta \log \mathcal{L}(K-\pi)$ cut in data**

  A second correction of this type is necessary due to the requirement of hadron $\Delta \log \mathcal{L}(K-\pi) > -5$ in the kaon data. The efficiency of this selection is measured in data from a calibration sample. Kaons from a clean sample of $D^0 \to K^{\pm}\pi^{\mp}$ decays are used, and are separately reweighted to $B^{\pm} \to \psi K^{\pm}$ simulation samples, where $\psi = J/\psi\,, \psi(2S)$. The weights are then applied to the $\Delta \log \mathcal{L}(K-\pi)$ spectrum of the kaon from data. The efficiency of the selection $\Delta \log \mathcal{L}(K-\pi) > -5$ is calculated as:

$$\begin{aligned} \epsilon_{J/\psi\, K}(\Delta \log \mathcal{L}(K-\pi) > -5) &= (98.9 \pm 0.5)\% \\ \epsilon_{\psi(2S)K}(\Delta \log \mathcal{L}(K-\pi) > -5) &= (99.0 \pm 0.5)\%\,. \end{aligned} \tag{3.13}$$

  The factors in Equation 3.14 are therefore multiplied by these corrections. A systematic of $\pm 0.5\%$ is assigned due to the use of the particle identification calibration sample in

this correction, as shown in Equation 3.13.

- **Correction due to reconstruction differences of the $\psi(2S)$ mode**

  Dedicated simulation samples for the $\psi(2S)$ resonance were unavailable for this analysis. To determine how the selection efficiency ratio depends on dimuon mass, samples of non-resonant $B^{\pm} \to \pi^{\pm}\mu^{+}\mu^{-}$ and $B^{\pm} \to K^{\pm}\mu^{+}\mu^{-}$ were used. The $\psi(2S)$ selection efficiency correction was checked in two dimuon mass windows of width $70\,\text{MeV}/c^2$, seen in Figure 3.20.

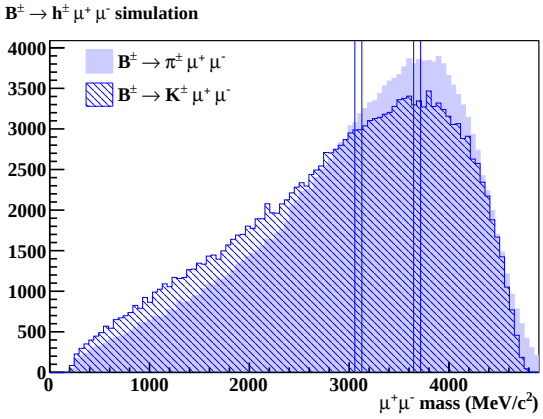

Figure 3.20: Dimuon mass distributions of the $B^{\pm} \to \pi^{\pm}\mu^{+}\mu^{-}$ (shaded) and $B^{\pm} \to K^{\pm}\mu^{+}\mu^{-}$ (hashed) simulation samples used to estimate the difference in selection efficiency between the J/ψ and $\psi(2S)$ modes. The two $70\,\text{MeV}/c^2$ mass windows used are shown in blue. The selection efficiency of both samples is measured in these windows.

	J/ψ selected / total	$\psi(2S)$ selected / total
$B^{\pm} \to K^{\pm}\mu^{+}\mu^{-}$	$3052/4306 = 0.709 \pm 0.007$	$3039/4723 = 0.643 \pm 0.007$
$B^{\pm} \to \pi^{\pm}\mu^{+}\mu^{-}$	$5372/7574 = 0.709 \pm 0.005$	$6025/9286 = 0.649 \pm 0.005$
Ratio $\epsilon_{K/\pi}$	0.999 ± 0.012	0.992 ± 0.013

Table 3.7: $\psi(2S)$ selection efficiency in two dimuon mass windows representing the J/ψ and $\psi(2S)$ in non-resonant samples of $B^{\pm} \to \pi^{\pm}\mu^{+}\mu^{-}$ and $B^{\pm} \to K^{\pm}\mu^{+}\mu^{-}$.

Table 3.7 shows the selected events (using the $\psi(2S)$ selection) divided by the total number of events within each window. The ratio of selection efficiencies is $0.992/0.999 = 0.992 \pm 0.018$ where the uncertainty here is due to the size of the simulation sample. This is used to scale the calculated $\psi(2S)$ efficiency.

After all corrections, the ratios of selection efficiencies are:

$$\begin{aligned} \omega_{sel}^{J/\psi} &= 0.948 \pm 0.004 \\ \omega_{sel}^{\psi(2S)} &= 0.957 \pm 0.017\,. \end{aligned} \tag{3.14}$$

3.7.3 Relative trigger efficiency, ω_{trig}^{ψ}

Due to the trigger requirements of this analysis, detailed in Section 3.2.3, the efficiency of triggering $B^{\pm} \to \psi h^{\pm}$ is expected to be independent of the hadron of the decay, and so $\omega_{trig}^{\psi} = 1$. A systematic uncertainty is assigned to this assumption.

3.7.4 Total correction to R_{Raw}^{ψ}

Combining the acceptance and selection corrections, the total corrections to R_{Raw}^{ψ} are:

$$\begin{aligned} \omega_{acc}^{J/\psi}\,\omega_{sel}^{J/\psi} &= 0.985 \pm 0.012 \\ \omega_{acc}^{\psi(2S)}\,\omega_{sel}^{\psi(2S)} &= 1.007 \pm 0.021\,. \end{aligned} \tag{3.15}$$

This factor scales the fitted R_{Raw}^{ψ} and its statistical uncertainty. The uncertainties on these correction factors are due to simulation statistics. A systematic is included to take these uncertainties into account. An additional uncertainty comes from the data efficiency of the kaon selection of $\Delta \log \mathcal{L}(K-\pi) > -5$ in the stripping. An additional systematic is assigned to this source.

3.7.5 Charge asymmetry corrections

Corrections to the measured charge asymmetries are now discussed. In addition to any physics *CP* asymmetry, there are other asymmetries which appear in the raw measurements:

- **Production asymmetry** (A_{Prod})**:**

  This accounts for a differing B^+ and B^- production rate at LHCb. Due to the pp nature of the collider only u valence quarks are available, not $\bar{u}$. This leads to unequal

production rates for $B^+ = u\bar{b}$ and $B^- = \bar{u}b$.

- **Detection asymmetry** (A^h_{Det})**:**
  Due to the LHCb detector being made of matter, the probability of detecting a hadron depends on its quark constituents (and so on its charge).

- **Left-right detector asymmetry** ($A^{\psi h}_{LR}$)**:**
  Differences between the left and right sides of LHCb, coupled with magnet polarity samples of different sizes, can contribute a perceived asymmetry due to acceptance effects.

These additional asymmetries need to be taken into account when converting from the measured asymmetry ($A^{\psi h}_{Raw}$) to the physics asymmetry ($A^{\psi h}_{CP}$).

The observable asymmetry is the sum of the contributing asymmetries:

$$A^{\psi h}_{Raw} \;=\; A_{Prod} + A^h_{Det} + A^{\psi h}_{CP} \pm A^{\psi h}_{LR}\,, \tag{3.16}$$

where this equation holds for the four channels of interest. The production asymmetry is the same in all channels. In this analysis it was decided to measure the production asymmetry in the $B^{\pm} \to J/\psi\, K^{\pm}$ channel, for which the *CP* asymmetry is already well determined; $A^{J/\psi\, K}_{CP} = (1 \pm 7) \times 10^{-3}$ [49]. Equation 3.16 can be rearranged:

$$A_{Prod} = A^{J/\psi\, K}_{Raw} - A^K_{Det} - A^{J/\psi\, K}_{CP} \pm A^{J/\psi\, K}_{LR}\,, \tag{3.17}$$

from which A_{Prod} is estimated to be -0.003 ± 0.009. This is used to determine the physics asymmetry in the three remaining channels:

$$A^{J/\psi\,\pi}_{CP} \;=\; A^{J/\psi\,\pi}_{Raw} - A_{Prod} - A^{\pi}_{Det} \pm A^{J/\psi\,\pi}_{LR} \tag{3.18}$$

$$A^{\psi(2S)\pi}_{CP} \;=\; A^{\psi(2S)\pi}_{Raw} - A_{Prod} - A^{\pi}_{Det} \pm A^{\psi(2S)\pi}_{LR} \tag{3.19}$$

$$A^{\psi(2S)K}_{CP} \;=\; A^{\psi(2S)K}_{Raw} - A_{Prod} - A^{K}_{Det} \pm A^{\psi(2S)K}_{LR}\,. \tag{3.20}$$

The kaon detection asymmetry term cancels from the definition of $A_{CP}^{\psi(2S)K}$ when substituting Equation 3.17, allowing a particularly precise determination of this parameter.

3.7.6 Hadron detection asymmetry

K^- mesons ($\bar{u}s$) have a higher interaction cross section than K^+ mesons ($u\bar{s}$). The principle reaction is $K^-N \to Y\pi$, where Y is a hyperon (a baryon containing one or more strange quarks, but no charm or bottom quarks) [102]. There is no equivalent reaction for the K^+.

Hadron detection asymmetry measurements are taken from other LHCb analyses. The most suitable analysis which determined the kaon detection asymmetry was also performed on the mid-2011 dataset, using a tagged sample of $D^{*\pm} \to D^0\pi^\pm$, $D^0 \to K^+\pi^-$. It finds $A_{Det}^K = (-1.0 \pm 0.2)\%$ [103]. As the detection asymmetry is expected to be largest at low kaon momentum, and this analysis uses a stronger hadron momentum selection ($5\,\text{GeV}/c$ vs. $1.1\,\text{GeV}/c$ in [103]), the detection asymmetry should be reduced. The uncertainty is nevertheless increased from 0.2% to 0.4% to take into account any remaining kinematic differences in the two analyses.

A recent LHCb study found the pion detection asymmetry to be compatible with 0 within 0.24% uncertainty [104]. This analysis uses $A_{Det}^\pi = (0.0 \pm 0.4)\%$, where an uncertainty equal to that of the kaon detection asymmetry uncertainty has been assigned.

3.7.7 Left-right detection asymmetry

Differences in the tracking and reconstruction efficiency in different regions of the detector have the potential to create a charge asymmetry. This asymmetry is accounted for by splitting the data by magnet polarity and fitting the samples separately, allowing fit parameters to differ between the two datasets. The A_{LR} parameter in the fit can float freely but must take an equal and opposite value in the two magnet polarity data samples. A_{LR} was found to be $(-8.49 \pm 4.27) \times 10^{-3}$.

3.8 Systematic uncertainties

The analysis was designed in such a way as to be largely free of systematic uncertainty. The majority of parameters in the fit are floating, and when using simulation, it is only the relative difference between pion and kaon decays which is relied upon.

In this section, all assumptions and fixed parameters are studied, either by altering a fixed parameter and rerunning the fit, or by modifying the selection. A systematic uncertainty is assigned, equal to the maximum variation seen in each observable. The systematic uncertainties are summarised in Table 3.8. The following list of effects was considered:

- **Simulation uncertainty**

  The largest uncertainty on R^{ψ} is due to the use of simulation to estimate the acceptance and selection efficiencies. This uncertainty accounts for the finite statistics of the simulation samples, and imperfections in the modelling of the relative detector response to pions and kaons. It was measured by adjusting the correction factors in Equation 3.15 by $\pm 1\sigma$, and calculating the shift in R^{ψ}.

- **Particle identification efficiencies**

  The calculation of the pion and kaon identification efficiencies also contributes significant systematic uncertainties to the R^{ψ} results. The fraction of pion events which pass the $\Delta \log \mathcal{L}(K-\pi) < 6$ selection is fixed from data, see Section 3.6. Varying the central values by $\pm 1\sigma$, the fit was rerun.

  In Section 3.7 the J/ψ and $\psi(2S)$ correction factors were multiplied by $(98.9 \pm 0.5)\%$ and $(99.0 \pm 0.5)\%$ respectively to take into account the stripping selection at kaon $\Delta \log \mathcal{L}(K-\pi) > -5$, which is not present in simulation. This figure is derived from data using a calibration sample. To calculate the systematic associated with this, R^{ψ} is recalculated using the central values $\pm 0.5\%$, and the shift taken as the uncertainty.

- $A_{CP}^{J/\psi K}$ **(PDG)**

  The estimation of the production asymmetry is a necessary component for all the physics asymmetry calculations in this analysis. It is performed in the $B^{\pm} \to J/\psi K^{\pm}$

channel, using the nominal value of $A_{CP}^{J/\psi K}$, the measured $A_{Raw}^{J/\psi K}$ and the kaon detector asymmetry.

The dominant systematic in the asymmetry measurements comes from uncertainty on the world average value of $A_{CP}^{J/\psi K}$, which is fixed to the PDG value:

$$A_{CP}^{J/\psi K} = (1 \pm 7) \times 10^{-3} \text{ [49]}. \tag{3.21}$$

A systematic equal to the uncertainty on this value is assigned.

- **$A_{Raw}^{J/\psi K}$ statistical uncertainty**

  The fitted value of $A_{Raw}^{J/\psi K}$ contributes to the production asymmetry determination. Therefore, the statistical uncertainty on this measurement is used as a systematic uncertainty in the asymmetry results.

- **Detection asymmetries**

  The pion and kaon detection asymmetries must be used to obtain the $A_{CP}^{\psi\pi}$ results. The uncertainty on both asymmetries is 0.004, which is taken twice as a systematic. In the $A_{CP}^{\psi(2S)K}$ result, the detector asymmetries cancel between this and the $A_{CP}^{J/\psi K}$ channel in which the production asymmetry is measured. Therefore no systematic is required.

- **Relative trigger efficiency**

  A selection is applied to the first level of the trigger (L0) to reduce the dependence on the hadron of the decay. However it is possible that an event is triggered at L0 by the muons, but at subsequent trigger levels by the hadron, so potentially introducing an efficiency difference between the two decays.

  A check was performed where in addition to passing the L0 requirement, data was also required to fire a (di)muon HLT2 line. This additional requirement removes 2.1% of the original L0 selected J/ψ data, and 4.6% of the selected $\psi(2S)$ data. The fit was rerun with the new data samples.

- **Fixed fit parameters**

  Various parameters of the fit are fixed to prevent instability, such as the line shape of

the pions which fall into the kaon-like subsample, the ratio of partially reconstructed backgrounds in the pion-like subsample, the left side of the kaon signal peak, and the tail shape of the kaons in the pion-like subsample. These fixed parameters were varied within their uncertainties, and the fit rerun.

	$R^{J/\psi}(\times 10^{-2})$	$A^{J/\psi\pi}$	$R^{\psi(2S)}(\times 10^{-2})$	$A^{\psi(2S)\pi}$	$A^{\psi(2S)K}$
Simulation uncertainty	0.045	-	0.088	-	-
PID efficiencies	0.043	-	0.052	-	-
$A^{J/\psi K}$ (PDG [49])	-	0.0070	-	0.0070	0.0070
$A^{J/\psi K}_{\rm Raw}$ statistical error	-	0.0046	-	0.0046	0.0046
Detection asymmetries	-	0.0056	-	0.0056	-
Relative trigger efficiency	0.020	0.0031	0.050	0.0036	0.0003
Fixed fit parameters	0.005	0.0006	0.017	0.0013	0.0001
Sum in quadrature (syst.)	0.065	0.0106	0.115	0.0108	0.0084
Fit error (stat.)	0.110	0.0268	0.404	0.0901	0.0136

Table 3.8: Summary of systematic uncertainties, and their sum in quadrature for each measurement. Statistical uncertainties on the fit results are included for comparison.

3.9 Results

The measured ratios of branching fractions are

$$\begin{aligned} R^{J/\psi} &= (3.83 \pm 0.11 \pm 0.07) \times 10^{-2} \\ R^{\psi(2S)} &= (3.95 \pm 0.40 \pm 0.12) \times 10^{-2}\,, \end{aligned}$$

where the first uncertainty is statistical and the second systematic. The measurement of $R^{J/\psi}$ is 3.2σ lower than the current world average of $(5.2 \pm 0.4) \times 10^{-2}$ [49]. $R^{\psi(2S)}$ is compatible with the one existing measurement, $(3.99 \pm 0.36 \pm 0.17) \times 10^{-2}$ [51]. Using the established measurements of the Cabibbo-favoured branching fractions [49], it is deduced that

$$\begin{aligned} \mathcal{B}(B^{\pm} \to J/\psi\pi^{\pm}) &= (3.88 \pm 0.11 \pm 0.15) \times 10^{-5} \\ \mathcal{B}(B^{\pm} \to \psi(2S)\pi^{\pm}) &= (2.52 \pm 0.26 \pm 0.15) \times 10^{-5}\,, \end{aligned}$$

where the systematic uncertainties are summed in quadrature.

The measured *CP* asymmetries are

$$\begin{aligned} A_{CP}^{J/\psi\,\pi} &= 0.005 \pm 0.027 \pm 0.011 \\ A_{CP}^{\psi(2S)\pi} &= 0.048 \pm 0.090 \pm 0.011 \\ A_{CP}^{\psi(2S)K} &= 0.024 \pm 0.014 \pm 0.008\,, \end{aligned}$$

where again the first uncertainty is statistical and the second systematic. These measurements have comparable or better precision than previous results [50] [51]. Every result is statistics limited. The limiting systematic in the charge asymmetry measurements is the current knowledge of $A_{CP}^{J/\psi\,K}$. No evidence of direct *CP* violation is seen.

3.9.1 Discussion

It is noted that the pull plot in Figure 3.14 shows a significant, though small, bias in the fitted value of $R^{J/\psi}$. The shift is measured as $+0.175\sigma$, or $+0.02\%$ using the statistical uncertainty quoted on $R^{J/\psi}$ above. This modifies the result at the per-mille level, from:

$$R^{J/\psi} = (3.83 \pm 0.11 \pm 0.07) \times 10^{-2}$$

to:

$$R^{J/\psi} = (3.81 \pm 0.11 \pm 0.07) \times 10^{-2}\,.$$

Chapter 4

The search for $B^{\pm} \to \pi^{\pm}\mu^{+}\mu^{-}$ decays

This chapter describes the search for, and the observation of, the rare $B^{\pm} \to \pi^{\pm}\mu^{+}\mu^{-}$ decay. It constitutes the same final state as that studied in Chapter 3 but does not pass through an intermediate ψ resonance. The charge averaged ratio of branching fractions is measured, relative to the Cabibbo favoured $B^{\pm} \to K^{\pm}\mu^{+}\mu^{-}$ decay:

$$R^{\mu\mu} = \frac{\mathcal{B}(B^{\pm} \to \pi^{\pm}\mu^{+}\mu^{-})}{\mathcal{B}(B^{\pm} \to K^{\pm}\mu^{+}\mu^{-})}\,, \tag{4.1}$$

and is expected to be around 5%. This measures the ratio of CKM matrix elements:

$$\frac{|V_{td}|^2}{|V_{ts}|^2} = \frac{R^{\mu\mu}}{f^2}\,, \tag{4.2}$$

where the final state hadronic factor $f = 0.87$ is calculated from simulation, see Section 1.8.1. The *CP* asymmetry of both modes is also measured:

$$A_{CP}^{\mu\mu h} = \frac{\mathcal{B}(B^{-} \to \mu\mu h^{-}) - \mathcal{B}(B^{+} \to \mu\mu h^{+})}{\mathcal{B}(B^{-} \to \mu\mu h^{-}) + \mathcal{B}(B^{+} \to \mu\mu h^{+})}\,, \tag{4.3}$$

where $h \in \{K, \pi\}$.

As covered in Chapter 1, the observation of $B^{\pm} \to \pi^{\pm}\mu^{+}\mu^{-}$ decays is the first detection of $b \to d\ell^{+}\ell^{-}$ transitions. Along with the observed $b \to s\ell^{+}\ell^{-}$ transitions, these decays are flavour changing neutral currents and are forbidden at tree level. New physics may interfere

at loop level, so causing a deviation from Standard Model predictions.

$|V_{td}/V_{ts}|$ has previously been measured using the radiative decays $b \to s\gamma$ and $b \to d\gamma$ [67] [68], and by neutral B meson mixing [66] to sub-percent level precision. $B^{\pm} \to h^{\pm}\mu^{+}\mu^{-}$ decays offer an alternative method for measuring this ratio of CKM matrix elements.

4.1 Datasets and validation

This analysis is performed on the full 2011 dataset, totalling $1.0\,\text{fb}^{-1}$. Raw data is taken from two stripping lines (see Section 2.10) which select $B^{\pm} \to h^{\pm}\mu^{+}\mu^{-}$ decays. The dataset includes the ψ resonances and dimuon pairs across the region $250 < m_{\mu\mu} < 5050\,\text{MeV}/c^2$. The stripping selection is shown in Table 4.1, it is tighter in comparison to that used in Chapter 3, which results in a higher preselected ratio of signal events to combinatorial background.

Variable	2011 selection
$K^{\pm}\mu^{+}\mu^{-}$ mass (MeV/c^2)	$4900 - 7000$
$B^{\pm}$ pointing angle ($^{\circ}$)	< 0.46
$B^{\pm}$ decay vertex χ^2	< 24
$B^{\pm}$ impact parameter χ^2	< 9
$B^{\pm}$ vertex separation χ^2	> 100
$\mu^{+}\mu^{-}$ mass (MeV/c^2)	< 5050
$\mu^{+}\mu^{-}$ decay vertex χ^2	< 9
$\mu^{\pm}$ track χ^2/ndof	< 4
$\mu^{\pm}$ impact parameter χ^2	> 16
$\mu^{\pm}$ $\Delta \log \mathcal{L}(\mu - \pi)$	> 0
$\mu^{\pm}$ isMuon	True
$h^{\pm}$ track χ^2/ndof	< 4
$h^{\pm}$ impact parameter χ^2	> 9

Table 4.1: Stripping selections of $B^{\pm} \to h^{\pm}\mu^{+}\mu^{-}$ candidates. Variables are defined in the Glossary.

Preselected candidates are reconstructed as $B^{\pm} \to h^{\pm}\mu^{+}\mu^{-}$, where the hadron mass hypothesis (K or π) is determined by the particle's $\Delta \log \mathcal{L}(K - \pi)$. In contrast to the $B^{\pm} \to \psi h^{\pm}$ analysis (Chapter 3), this analysis cannot employ a ψ mass constraint. Data is split into signal ($4900 < m_B(\,\text{MeV}/c^2) < 5600$) and sideband ($5600 < m_B(\,\text{MeV}/c^2) < 7000$) regions. The $\psi \to \mu^{+}\mu^{-}$ resonances are isolated, see Section 4.2.3, and act as high statistics control samples.

Comparisons between all preselected data events and simulation are shown in Appendix C.

These plots show simulated $B^{\pm} \to K^{\pm}\mu^{+}\mu^{-}$ decays, $B^{\pm} \to J/\psi K^{\pm}$ decays in data isolated by the ψ mass selection, and background from the data sideband reconstructed as $B^{\pm} \to K^{\pm}\mu^{+}\mu^{-}$. $B^{\pm} \to h^{\pm}\mu^{+}\mu^{-}$ decays are kinematically similar, whether or not they pass through a ψ resonance. Simulation, tuned to replicate 2011 running conditions, adequately describes the J/ψ data sample in the relevant distributions. Variables for which signal simulation and sideband distributions exhibit differences have discrimination power, and are used as input to a multivariate selection (see Section 4.2.5).

4.2 Selection

The principal selection is performed using a Boosted Decision Tree (BDT), implemented in TMVA [105]. This is preceded by the application of trigger requirements, and the removal of the ψ resonances. The $\Delta \log \mathcal{L}(K-\pi)$ value used to separate pions and kaons is also chosen.

4.2.1 Trigger requirements

In order to maintain the same trigger efficiency between the pion and kaon modes, the events are required to be triggered on the signal muons or on the decay products of the other b quark in the event (the event background). This trigger requirement is 82% efficient compared to the preselected data.

4.2.2 Particle identification calibration requirements

To calculate the efficiency of the $\Delta \log \mathcal{L}(K-\pi)$ requirement on selected pions and kaons, signal event samples are calibrated against high statistics pion and kaon reference samples from $D^{*} \to D^{0}\pi$, $D^{0} \to K^{\pm}\pi^{\mp}$ decays. The calibration is performed by reweighting the samples, binned in the variables which most strongly dictate the particle identification performance: p and p_T. The discriminating power of the RICH degrades at very high momentum, so a requirement that $p < 110\,\mathrm{GeV}/c$ is imposed on all hadron tracks. A loose upper limit on transverse momentum of hadrons is also used: $p_T < 20\,\mathrm{GeV}/c$.

4.2.3 Removal of ψ resonances

Signal-like $h^{\pm}\mu^{+}\mu^{-}$ final states which decay through the J/ψ or $\psi(2S)$ resonances must be vetoed from the sample. Due to the large size of the ψ peaks and their radiative tails, a cut based only on dimuon mass is not optimal and a two-dimensional selection based on both dimuon mass and B mass is preferred.

The J/ψ and $\psi(2S) \to \mu^{+}\mu^{-}$ peaks from the $1.0\,\text{fb}^{-1}$ sample are shown in Figure 4.1. The J/ψ peak is narrower than that of the $\psi(2S)$, $12.5\,\text{MeV}/c^2$ compared with $14.8\,\text{MeV}/c^2$, but the $B^{\pm} \to J/\psi\, h^{\pm}$ decay is a factor of 10 more prevalent. To ensure that no events from the ψ resonances enter the non-resonant sample, a J/ψ ($\psi(2S)$) veto of width $200\,\text{MeV}/c^2$ ($140\,\text{MeV}/c^2$) is used. Figure 4.2 shows the vetoed area. Two bands are removed from the dimuon mass versus B mass spectra, which ensures that an equal amount of dimuon mass spectrum is removed for a given B mass value. Within the region of the B peak, the sloping veto is described by:

$$\left|(m_B - M_B)\cos\left(\frac{\pi}{8}\right) - (m_\psi - M_\psi)\sin\left(\frac{\pi}{8}\right)\right| < 2w\cos\left(\frac{\pi}{8}\right) , \tag{4.4}$$

where m denotes measured mass values, M the PDG mass values, and w is half the width of the exclusion zone.

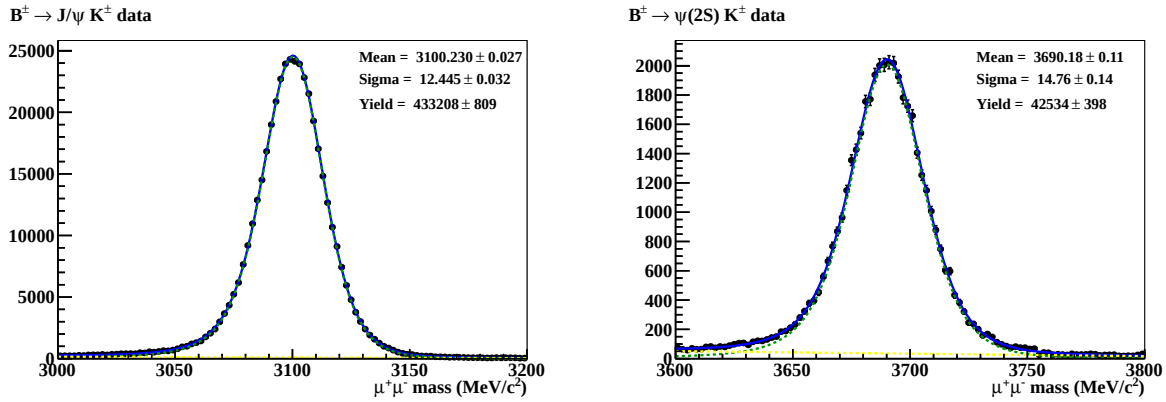

(a) (b)

Figure 4.1: Dimuon invariant mass spectra of a) $B^{\pm} \to J/\psi\, K^{\pm}$ and b) $B^{\pm} \to \psi(2S)K^{\pm}$ decays in data. The distributions are fitted with a modified Gaussian (Equation 3.4) and a linear polynomial.

A second veto is necessary to remove a specific background in which the same sign hadron

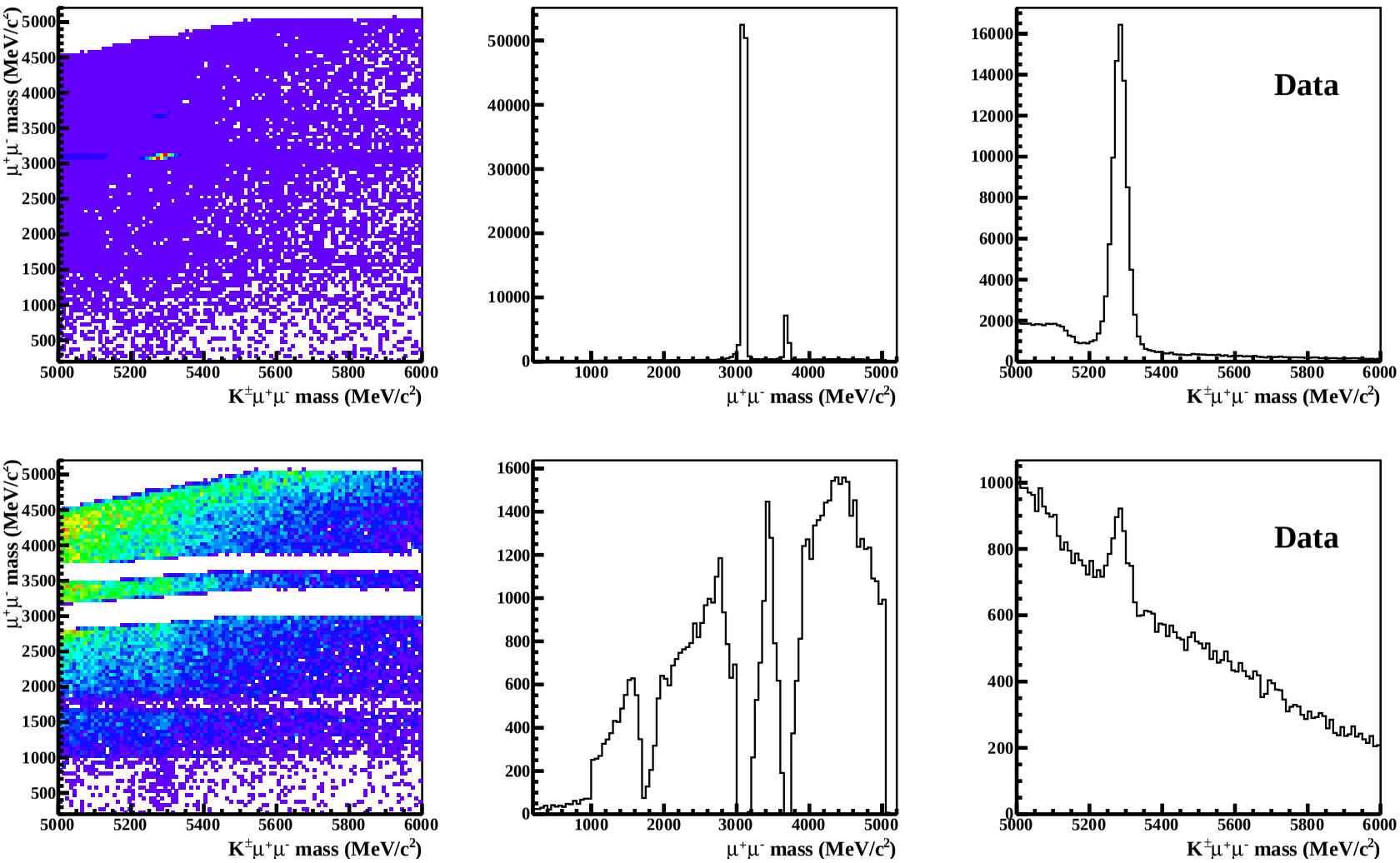

Figure 4.2: The effect of the ψ veto on the B mass and dimuon mass spectra of the $B^{\pm} \to K^{\pm}\mu^{+}\mu^{-}$ candidates in data. Top: veto not applied. Bottom: veto applied. The dimuon mass spectrum shows no remnant of the ψ peaks. The $K^{\pm}\mu^{+}\mu^{-}$ peak is clearly evident in the B mass spectrum, on top of a significant background (before the BDT application). The D^{0} veto is also applied, with muons under a hadron hypothesis, resulting in the dip at $\sim 1860\,\mathrm{MeV}/c^{2}$.

and muon in $B^{\pm} \to \psi h^{\pm}$ decays are both misidentified, forming an opposite sign dimuon pair and hadron which are reconstructed as signal. These events avoid the ψ veto due to the first misidentification, but fall under the B peak as the second misidentification compensates for the first. This background can be partially identified by determining whether the reconstructed hadron is associated with hits in the muon chambers. If this is the case, reconstructing the opposite sign hadron-muon pair, both under the muon hypothesis, shows clear ψ peaks which are vetoed (see Figure 4.3).

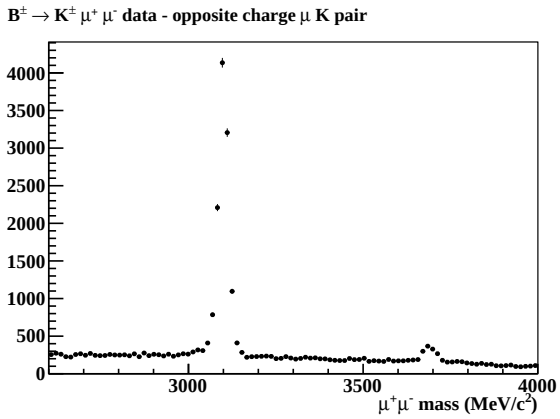

Figure 4.3: Mass spectrum of opposite charge μ h pairs in data, taken from a "suspicious" subset of events where the hadron has associated hits in the muon chambers. The h is reconstructed under the muon hypothesis, and clear J/ψ and $\psi(2S)$ peaks are clear. This $B^{\pm} \to \psi h^{\pm}$ pollution is removed by applying a ψ veto to these events.

4.2.4 Removal of $B^{\pm} \to D^{0}h^{\pm}$

$B^{\pm} \to D^{0}h^{\pm}$ decays were found to contaminate the event sample, and so are removed with a veto in dimuon mass. The muons are reconstructed under a hadron hypothesis, to match the favoured $B^{\pm} \to D^{0}(\to K^{\pm}\pi^{\mp})h^{\pm}$ decay mode. $B^{\pm} \to D^{0}(\to K^{\pm}\pi^{\mp})\pi^{\pm}$ has a branching fraction of $(2 \pm 0.4) \times 10^{-4}$, so a 1% hadron to muon misidentification probability means these events enter the data sample with the same order of magnitude as signal. Figure 4.2 shows the dimuon spectrum in data, with all vetoes applied.

4.2.5 Boosted decision tree

A multivariate analysis is used to distinguish between the rare $B^{\pm} \to h^{\pm}\mu^{+}\mu^{-}$ decays and the dominant combinatorial background. The TMVA framework [105] provides the multivariate classification. A Boosted Decision Tree[1] (BDT) method was chosen due to its speed, performance and robustness against over-training.

Multivariate analysis techniques make use of 'training' datasets, which are known to contain signal or background events, to train an algorithm to distinguish between the two. The trained algorithm is then used to extract signal events from a dataset including background. Each event is given a classification (a number between -1 and 1) which describes how signal-like it is. The choice of where to cut the dataset (the working point) depends on the required purity.

This section describes the datasets used to train and test the BDT, and the input variables which distinguish between signal and background. The performance of the BDT and choice of the working point are also described.

Input datasets

The BDT is trained on $B^{\pm} \to \pi^{\pm}\mu^{+}\mu^{-}$ simulation and the high B mass sideband from data. The selections described previously in this section are applied to these samples prior to training. The B mass distributions of the training samples are shown in Figure 4.4. The signal simulation sample contains 60k events. The B mass sideband ($5600 - 7000$ MeV/c^2) contains 20k events. The input events from both datasets are split randomly in half to give training and testing samples. The $B_c^{\pm}$ peak (see Figure 4.5) is visible in the sideband data, but is removed by the ψ veto. $B_c^{\pm} \to \pi^{\pm}\mu^{+}\mu^{-}$ is neglected.

[1] A Decision Tree is a set of sequential cuts, often visualised in a tree structure. Events pass through a series of selections, each following a branch of the tree before being labelled as signal or background. 'Boosting' refers to reweighting events from the training samples, and repeating the tree determination process. This results in many decision trees to classify each event. The individual results are combined for a single final classification.

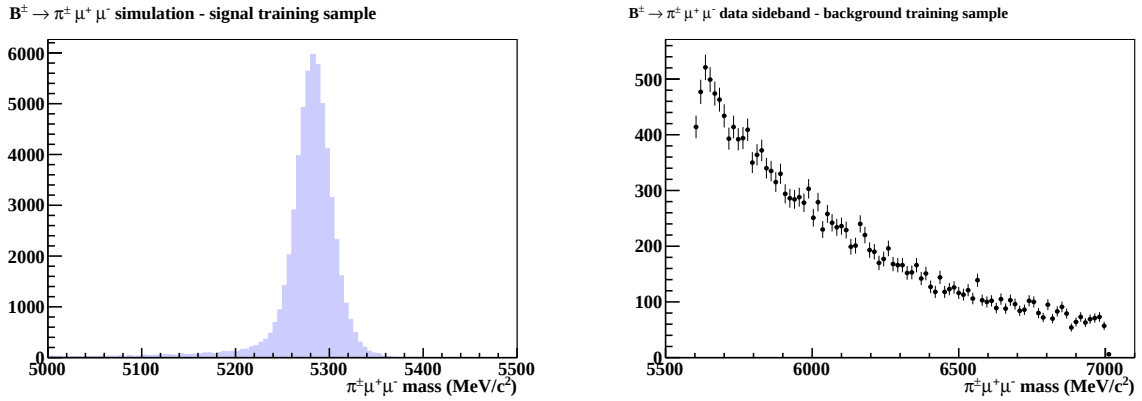

(a) (b)

Figure 4.4: B mass distributions of the signal (a) and background (b) training samples. There is no sign that any $B_c^{\pm}$ decays ($m_{B_c} = 6277\,\mathrm{MeV}/c^2$) pass the ψ veto.

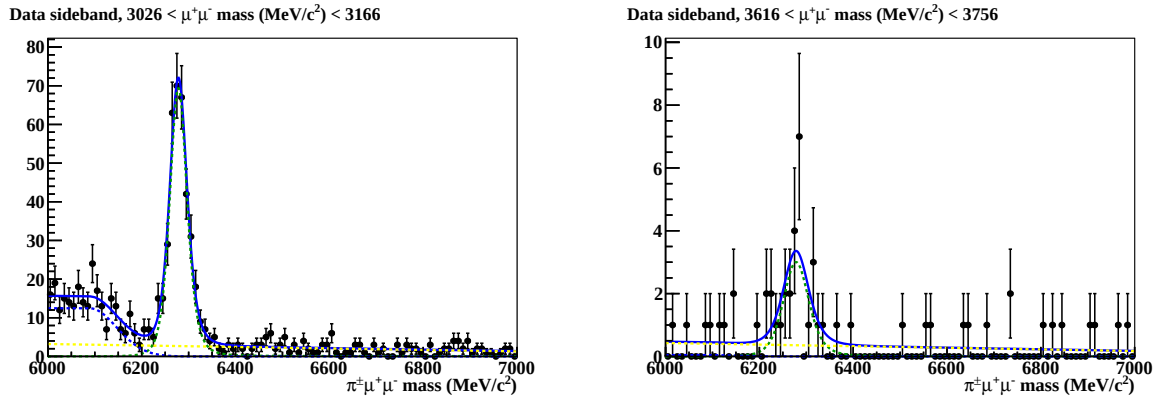

(a) (b)

Figure 4.5: $B_c^{\pm} \to \psi\pi^{\pm}$ decays, observed in the data sideband by applying a rough selection and hadron $\Delta \log \mathcal{L}(K - \pi) < 0$ requirement. Both the J/ψ (a) and $\psi(2S)$ (b) decays are seen. The yield of the $B_c^{\pm} \to \psi(2S)\pi^{\pm}$ decay is consistent with the first observation of this mode [106].

Input variables

The variables available to the BDT are shown in Table 4.2. In total 14 variables are used, which were chosen for their power to differentiate between signal and background. These variables also benefit from good data-simulation agreement.

Variable
h^+, $\mu^\pm$ momentum (MeV/c)
$h^+, \mu^\pm$ transverse momentum (MeV/c)
$\mu^+\mu^-$ momentum asymmetry (MeV/c)
$h^+, \mu^\pm$ impact parameter χ^2
cos(h^+ decay angle)
B transverse momentum (MeV/c)
B decay vertex χ^2
$\log_{10}(1 - \cos(B$ pointing angle))

Table 4.2: The 14 variables used by the multivariate analysis. Charge conjugation is applied.

The distributions for most of these variables are shown in Appendix C. The exception is seen in Figure 4.6. The difference in the muon momenta ($|p_{\mu^+} - p_{\mu^-}|$) is used as a discriminating variable as muons from the same mother particle are more likely to have similar momenta than combinatorial muons.

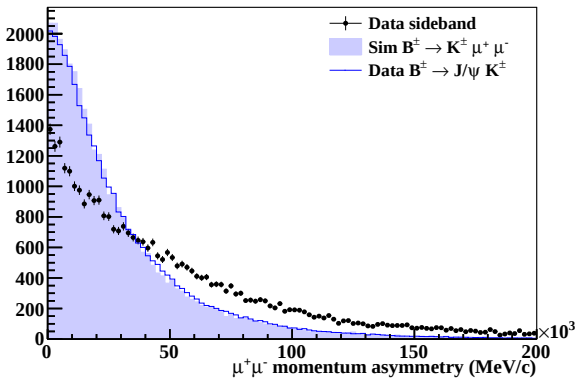

Figure 4.6: The muon momentum asymmetry, defined as $|p_{\mu^+} - p_{\mu^-}|$, shown for $B^\pm \to K^\pm\mu^+\mu^-$ simulation, $B^\pm \to J/\psi K^\pm$ data and data sideband. In true dimuon decays, the two muons are more likely to have a similar momentum than if the muons come from combinatorial background.

Classifier performance

The response of the classifier to the signal and background datasets is shown in Figure 4.7(a). This plot shows the training and testing datasets overlaid. A small disagreement is seen in the tail of the background samples, but overall over-training is not indicated. The performance of the classifier is quantified in Figure 4.7(b), which shows excellent background rejection versus signal efficiency.

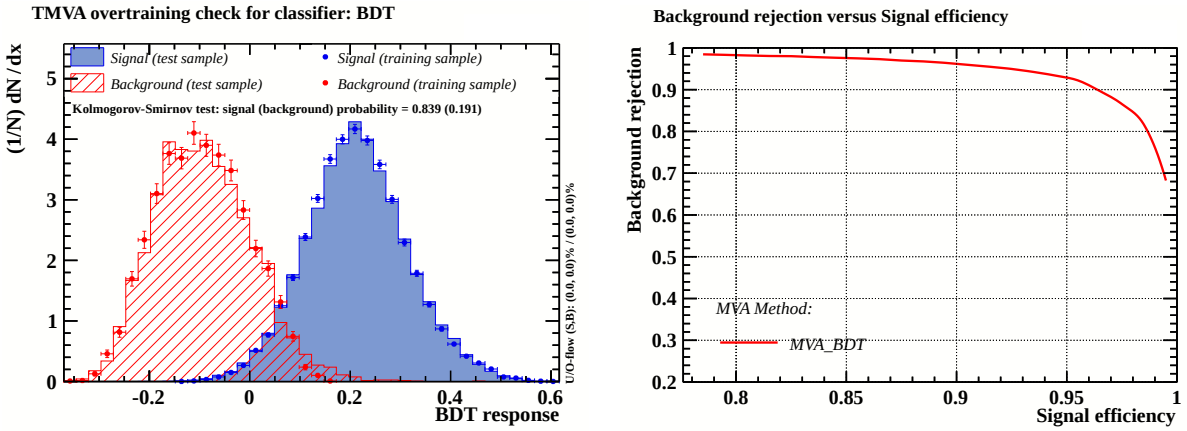

(a) (b)

Figure 4.7: a) Classifier responses to signal and background datasets for the BDT. Training and testing datasets are overlaid and in agreement, showing that overtraining has not occurred. b) Background rejection verses signal efficiency.

Choice of working point

The working point is chosen by applying the classifier response to the data, and choosing the value for which the significance of the $B^{\pm} \to \pi^{\pm}\mu^{+}\mu^{-}$ peak is expected to be maximal. To avoid any bias, the analysis is performed in a 'blind' manner, i.e. the $B^{\pm} \to \pi^{\pm}\mu^{+}\mu^{-}$ peak in data is not revealed until all analysis choices are finalised. The significance (σ) is defined as:

$$\sigma = \frac{S}{\sqrt{S+B}}, \tag{4.5}$$

where the number of signal events S is taken to be the number of $B^{\pm} \to K^{\pm}\mu^{+}\mu^{-}$ decays observed in data, scaled by the expected ratio of branching fractions (0.05 from Equation 4.1)

and the relative efficiency of observing $B^{\pm} \to K^{\pm}\mu^{+}\mu^{-}$ and $B^{\pm} \to \pi^{\pm}\mu^{+}\mu^{-}$ decays:

$$S = N_{\rm obs}^{K\mu\mu} \times 0.05 \times \frac{\varepsilon(\pi|\Delta\log\mathcal{L}(K-\pi) < x)}{\varepsilon(K|\Delta\log\mathcal{L}(K-\pi) > x)}\,, \tag{4.6}$$

where x is the value of $\Delta\log\mathcal{L}(K-\pi)$ used to separate pions and kaons.

The number of background events, B, is the number of combinatorial events seen within $\pm 2\sigma$ of the $B^{\pm} \to K^{\pm}\mu^{+}\mu^{-}$ peak mean, scaled by the ratio of background expected in $B^{\pm} \to K^{\pm}\mu^{+}\mu^{-}$ and $B^{\pm} \to \pi^{\pm}\mu^{+}\mu^{-}$ decays. This is measured at each possible working point using the high mass sideband with BDT and $\Delta\log\mathcal{L}(K-\pi)$ cuts applied:

$$B = \frac{N_{\rm SB}^{\pi\mu\mu}}{N_{\rm SB}^{K\mu\mu}} \times N_{\rm comb}^{K\mu\mu}\,. \tag{4.7}$$

To calculate the efficiency of various $\Delta\log\mathcal{L}(K-\pi)$ selections, a calibration was performed against samples known to contain either pions or kaons. Table 4.3 shows the efficiency of a range of $\Delta\log\mathcal{L}(K-\pi)$ values in separating pions from kaons. The ratio of efficiencies, needed in Equation 4.6 is also shown. A $\Delta\log\mathcal{L}(K-\pi)$ value of -5 was chosen to restrict the misidentified $B^{\pm} \to K^{\pm}\mu^{+}\mu^{-}$ yield to be less than 1% of the total. The systematic uncertainty on this calibration is 0.5% for pions, 0.1% for kaons.

$\Delta\log\mathcal{L}(K-\pi)$	π ID efficiency	K ID efficiency	π/K efficiency
-10	0.631	0.997	0.63
-9	0.654	0.997	0.66
-8	0.678	0.996	0.68
-7	0.702	0.995	0.71
-6	0.727	0.994	0.73
-5	**0.750**	**0.991**	**0.76**
-4	0.779	0.990	0.79
-3	0.806	0.986	0.82
-2	0.831	0.980	0.85
-1	0.857	0.973	0.88
0	0.880	0.963	0.91

Table 4.3: Efficiencies for a range of $\Delta\log\mathcal{L}(K-\pi)$ used to separate $B^{\pm} \to \pi^{\pm}\mu^{+}\mu^{-}$ decays from $B^{\pm} \to K^{\pm}\mu^{+}\mu^{-}$ decays. The ratio used in Equation 4.6 is shown. The chosen value of $\Delta\log\mathcal{L}(K-\pi) = -5$ is highlighted.

The fitted yields and the highlighted efficiencies from Table 4.3 are used to calculate

the expected signal significance according to Equation 4.5. Figure 4.8 shows how these quantities vary as a function of BDT selection. The highest expected significance occurs at BDT > 0.16.

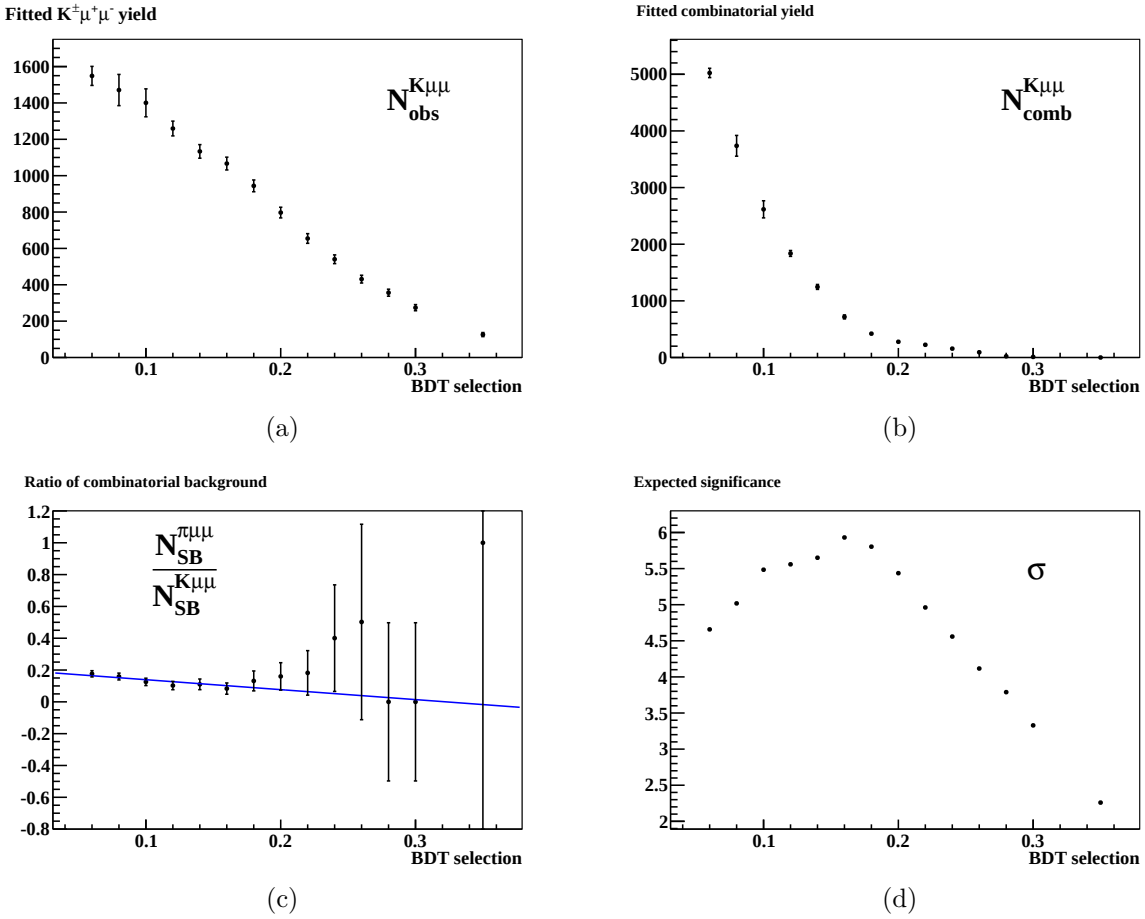

Figure 4.8: Choice of working point by maximising Equation 4.5. a) Fitted $B^{\pm} \to K^{\pm}\mu^{+}\mu^{-}$ signal yield. b) fitted combinatorial yield, measured from data as a function of BDT cut. c) Expected ratio of background events, measured from the sideband and fitted to avoid statistical fluctuations. d) Expected significance as a function of BDT cut.

As Equation 4.5 gives the significance only for a simple counting analysis, to finalise the choice of working point, several pseudo-experiments were run which generated the event yields expected given a BDT selection of ~ 0.16. The toys were fit with the 'full' hypothesis, including a $\pi^{\pm}\mu^{+}\mu^{-}$ signal peak, and a 'null' hypotheses in which the $\pi^{\pm}\mu^{+}\mu^{-}$ yield is forced to zero. The distance between the two fit minima gives the significance of the $\pi^{\pm}\mu^{+}\mu^{-}$ observation. From this it was found that a selection of BDT > 0.18 is expected to give the highest signal significance. Inspecting Figure 4.8(a) around 1000 $B^{\pm} \to K^{\pm}\mu^{+}\mu^{-}$ events

should be found in a signal extraction fit.

Selected data

Selected data and $B^{\pm} \to K^{\pm}\mu^{+}\mu^{-}$ simulation are compared in Figures 4.9 and 4.10. These figures show that post selection; data and simulation agree well. The track χ^2/ndf variable shows poor agreement between data and simulation. This variable is not used in the analysis. Other small differences are similar in both $K^{\pm}\mu^{+}\mu^{-}$ and $\pi^{\pm}\mu^{+}\mu^{-}$ decays, and so have negligible effect on the ratios used as correction factors.

4.3 Signal lineshape

The shapes of the $B^{\pm} \to \pi^{\pm}\mu^{+}\mu^{-}$ and $B^{\pm} \to K^{\pm}\mu^{+}\mu^{-}$ mass peaks were studied in simulation with the selection described in Section 4.2 applied. Figures 4.11 and 4.12 show details of the fitted $B^{\pm} \to K^{\pm}\mu^{+}\mu^{-}$ and $B^{\pm} \to \pi^{\pm}\mu^{+}\mu^{-}$ peaks respectively[2]. A modified Gaussian function is used to model the B peak (see Equation 3.4). As seen previously, the kaon channel has a slightly narrower peak than the pion channel due to the lower Q^2 available. The signal peak was studied as a function of invariant dimuon mass. In both channels, the resolution degrades slightly in the region of high dimuon mass. This may be due to the worsening momentum resolution of high momentum tracks, which curve less when traversing the magnetic field, or slow moving hadrons being multiply scattered more easily.

The ratios of fitted parameters as a function of dimuon mass are shown in Figure 4.13. Both plots are well described by a constant parameter, showing that the ratio of fitted parameters between π and K channels is independent of dimuon mass. The ratio of fitted B mass from the two channels is consistent with 1. The ratio of fitted B widths is 1.026 ± 0.010, reflecting the narrower peak width in the kaon mode.

The $B^{\pm} \to K^{\pm}\mu^{+}\mu^{-}$ peak lineshape in data was fitted with Equation 3.4. The width of the distribution is $\sim 18\,\mathrm{MeV}/c^2$, which is consistent with the unconstrained $B^{\pm} \to J/\psi\, K^{\pm}$

[2]For both channels, the simulation shows a B mass which is several MeV/c^2 too high. This is also seen in other LHCb analyses. It does not affect this analysis, as absolute B mass values from simulation are not used.

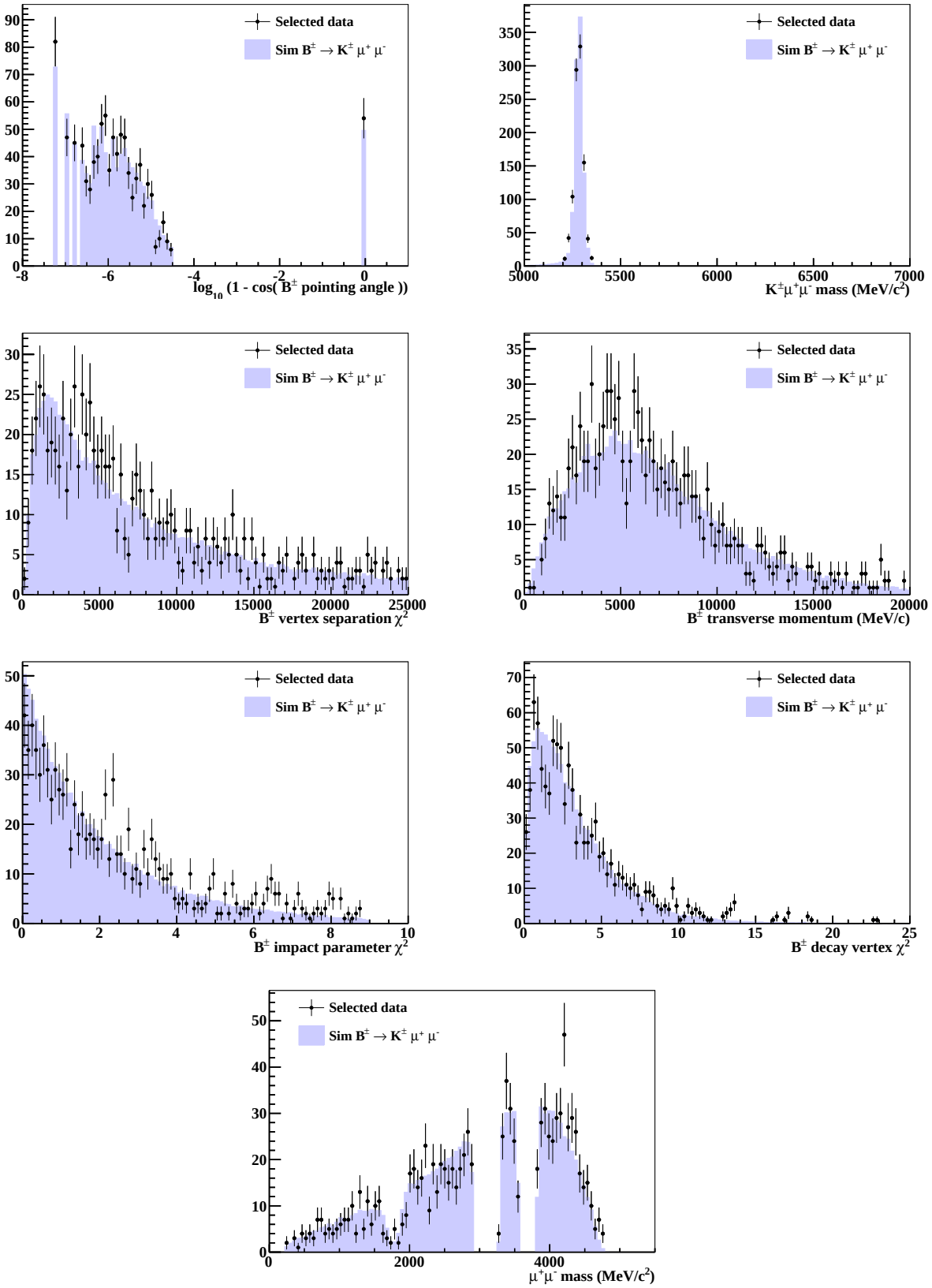

Figure 4.9: The final data set after selection (black points) compared with $B^{\pm} \to K^{\pm}\mu^{+}\mu^{-}$ simulation (shaded).

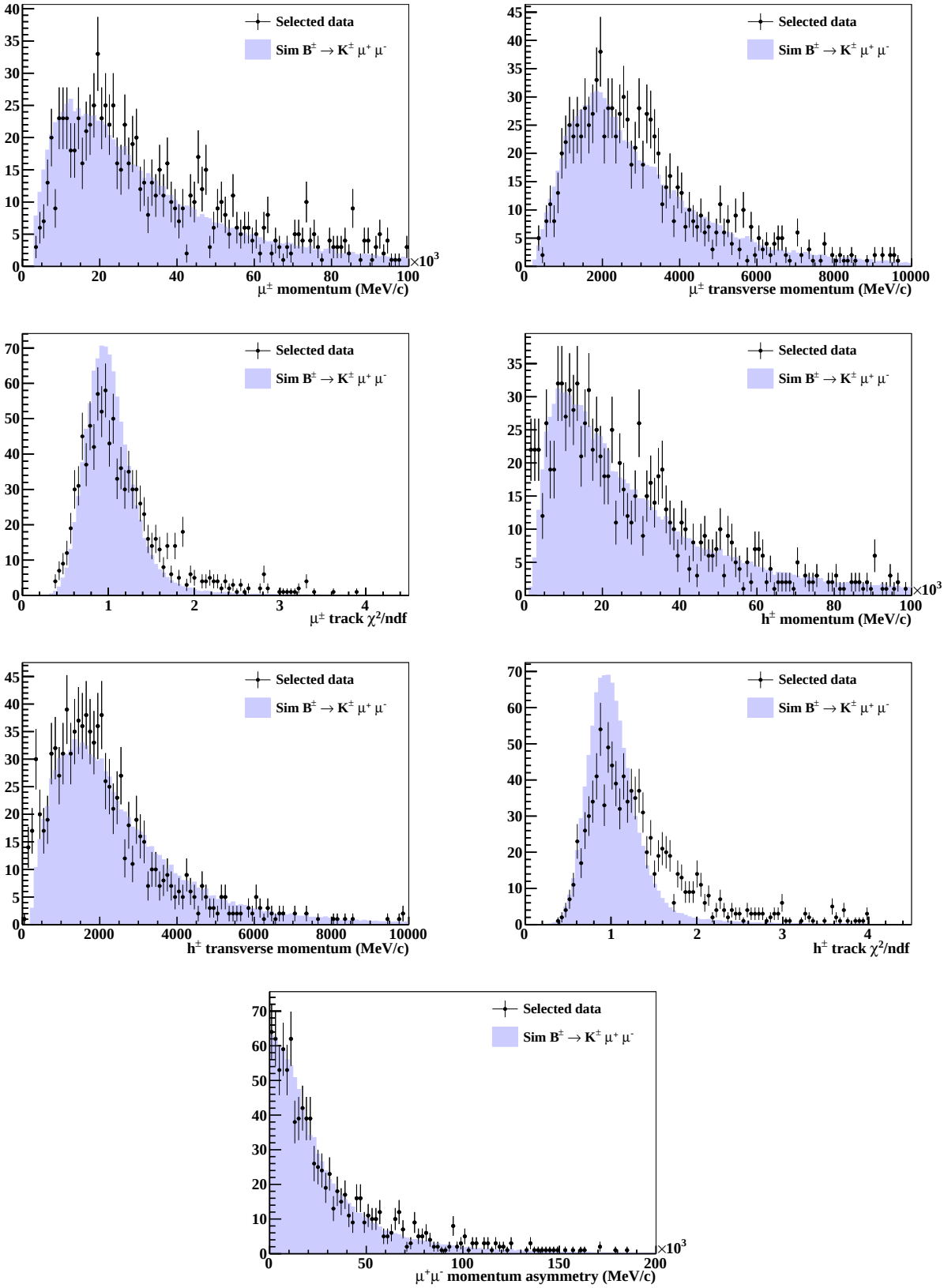

Figure 4.10: The final data set after selection (black points) compared with $B^{\pm} \to K^{\pm}\mu^{+}\mu^{-}$ simulation (shaded).

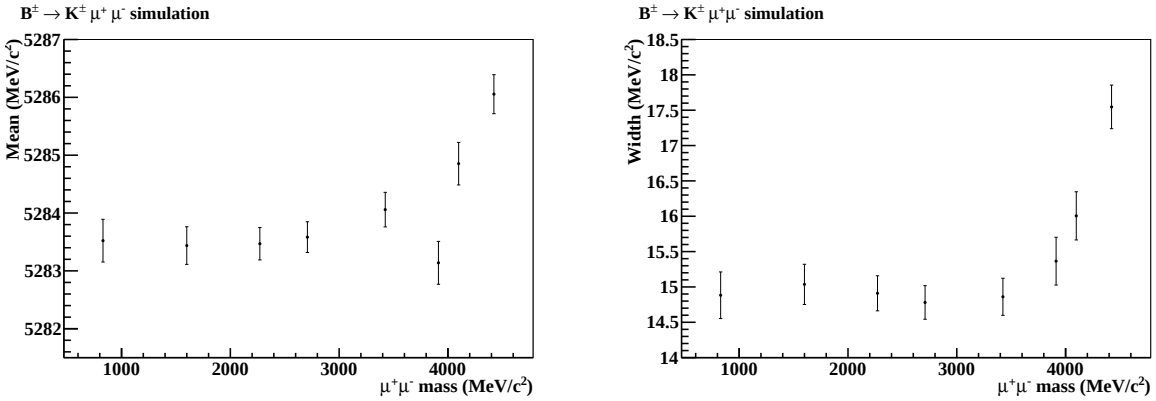

(a) (b)

Figure 4.11: B peak mean and width from simulated $B^{\pm} \to K^{\pm}\mu^{+}\mu^{-}$ decays, as a function of dimuon mass. Dimuon values are taken as the barycentre of the dimuon mass bin. a) Fitted B mass as a function of dimuon mass. b) Fitted B width as a function of dimuon mass.

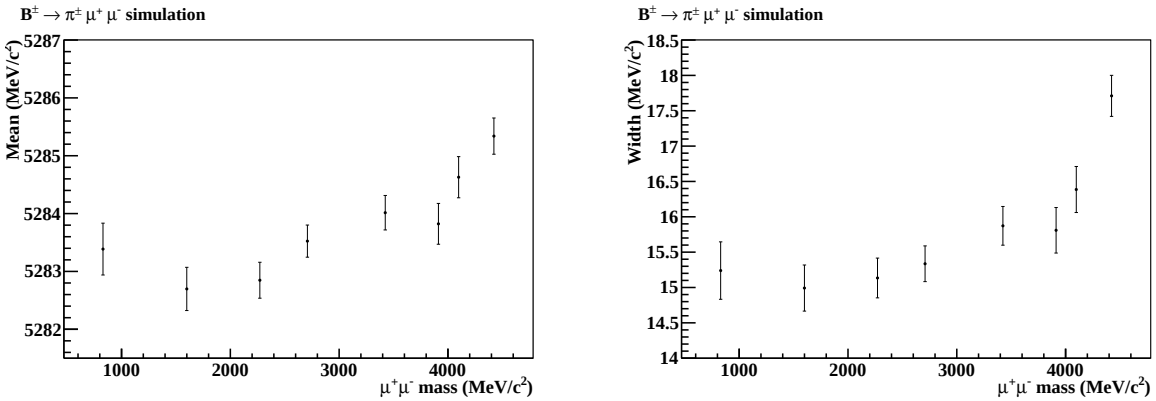

(a) (b)

Figure 4.12: B peak mean and width from simulated $B^{\pm} \to \pi^{\pm}\mu^{+}\mu^{-}$ decays, as a function of dimuon mass. For details see Figure 4.11 caption.

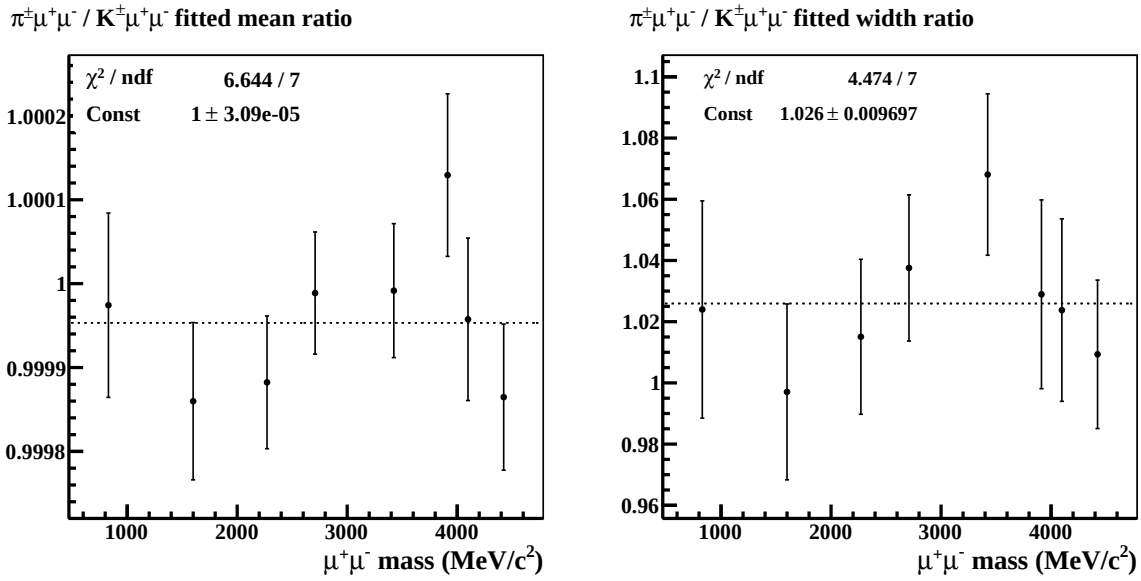

Figure 4.13: Ratio of fitted parameters from simulated $B^{\pm} \to \pi^{\pm}\mu^{+}\mu^{-}$ and $B^{\pm} \to K^{\pm}\mu^{+}\mu^{-}$ decays. Left: Ratio of fitted means, which is consistent with 1. Right: Ratio of fitted width parameters, shown to be independent of dimuon mass.

peak studied in the earlier analysis (Figure 3.8). This width is 20% larger than simulation, but this does not affect the ratio of widths used to derive the $K^{\pm}\mu^{+}\mu^{-}$ to $\pi^{\pm}\mu^{+}\mu^{-}$ correction.

The $B^{\pm} \to K^{\pm}\mu^{+}\mu^{-}$ peak shape in data was studied when partitioned by charge and magnet polarity, see Table 4.4. Some variation was seen between the partitioned samples, however, the statistical precision of the measurement is such that the signal extraction fit does not require such a complicated partitioning.

The results from this section are summarised in Table 4.4. One value is carried forward in the analysis. The well populated peak of the Cabibbo favoured $B^{\pm} \to K^{\pm}\mu^{+}\mu^{-}$ decay can be used to constrain the width of the lesser populated, suppressed $B^{\pm} \to \pi^{\pm}\mu^{+}\mu^{-}$ peak. Therefore, the ratio between $B^{\pm} \to K^{\pm}\mu^{+}\mu^{-}$ and $B^{\pm} \to \pi^{\pm}\mu^{+}\mu^{-}$ peak widths is fixed in the signal extraction fit of data to that seen in simulation:

$$\frac{\sigma_{\pi\mu\mu}}{\sigma_{K\mu\mu}} = 1.026 \pm 0.010. \tag{4.8}$$

The uncertainty in the ratio is included as a systematic.

Decay	Sample	Width (MeV/c^2)	Mean (MeV/c^2)	Δ_{mean} (MeV/c^2)
$B^{\pm} \to \pi^{\pm}\mu^{+}\mu^{-}$	Simulation	15.9 ± 0.1	5283.9 ± 0.1	-0.1
$B^{\pm} \to K^{\pm}\mu^{+}\mu^{-}$	Simulation	15.4 ± 0.1	5284.0 ± 0.1	0
$B^{+} \to K^{+}\mu^{+}\mu^{-}$	Down	19.2 ± 1.4	5281.7 ± 1.6	-2.3
$B^{-} \to K^{-}\mu^{+}\mu^{-}$	Down	18.7 ± 1.2	5284.3 ± 1.5	0.3
$B^{+} \to K^{+}\mu^{+}\mu^{-}$	Up	17.9 ± 1.4	5284.7 ± 1.6	0.7
$B^{-} \to K^{-}\mu^{+}\mu^{-}$	Up	19.2 ± 1.6	5283.2 ± 2.0	-0.8
$B^{\pm} \to K^{\pm}\mu^{+}\mu^{-}$	Combined	18.0 ± 0.6	5283.4 ± 0.8	-0.6

Table 4.4: B mass peak comparison between the two simulated signal samples and $B^{\pm} \to K^{\pm}\mu^{+}\mu^{-}$ decays in data. 'Down' and 'Up' refer to the magnet polarity used during data recording.

4.4 Backgrounds

4.4.1 Misidentified hadron peaking background

The hadron in $B^{\pm} \to h^{\pm}\mu^{+}\mu^{-}$ decays may be misidentified and therefore reconstructed with the wrong mass hypothesis. This causes an auxillary peak to the correctly reconstructed signal peak in the pion-like and kaon-like mass distributions. Two cases are considered:

Misidentified $B^{\pm} \to K^{\pm}\mu^{+}\mu^{-}$

Around 20 times more $B^{\pm} \to K^{\pm}\mu^{+}\mu^{-}$ decays are expected than $B^{\pm} \to \pi^{\pm}\mu^{+}\mu^{-}$ decays. Therefore, misidentifying a small fraction of the kaon mode as pion-like can cause a background peak of significant amplitude. Table 4.3 shows that $\sim 1\%$ of kaon events will be misidentified with the selection $\Delta \log \mathcal{L}(K - \pi) < -5$, approximately 10 events in this dataset.

Misidentified kaon decays are reconstructed with the pion mass hypothesis, and so peak below the B mass. Figure 4.15(a) shows the $B^{\pm} \to K^{\pm}\mu^{+}\mu^{-}$ peaking background shape from simulation. A Crystal Ball shape is found to be an adequate effective PDF for these events. All selections have been applied, including the requirement $\Delta \log \mathcal{L}(K - \pi) < -5$. This is necessary, as it alters the momentum spectrum of the selected hadrons and therefore the shape of their mass distribution.

The shape of this peaking background in data is estimated by correcting the shape from simulation by known differences between data and simulation. Correctly reconstructed $B^{\pm} \to K^{\pm}\mu^{+}\mu^{-}$ decays in simulation and data are used to determine the convolution function

necessary to correct for any differences, see Figure 4.14. This is applied to the shape of the peaking background from simulation, see Figure 4.15(a). Uncertainties on these shape parameters are accounted for as systematics.

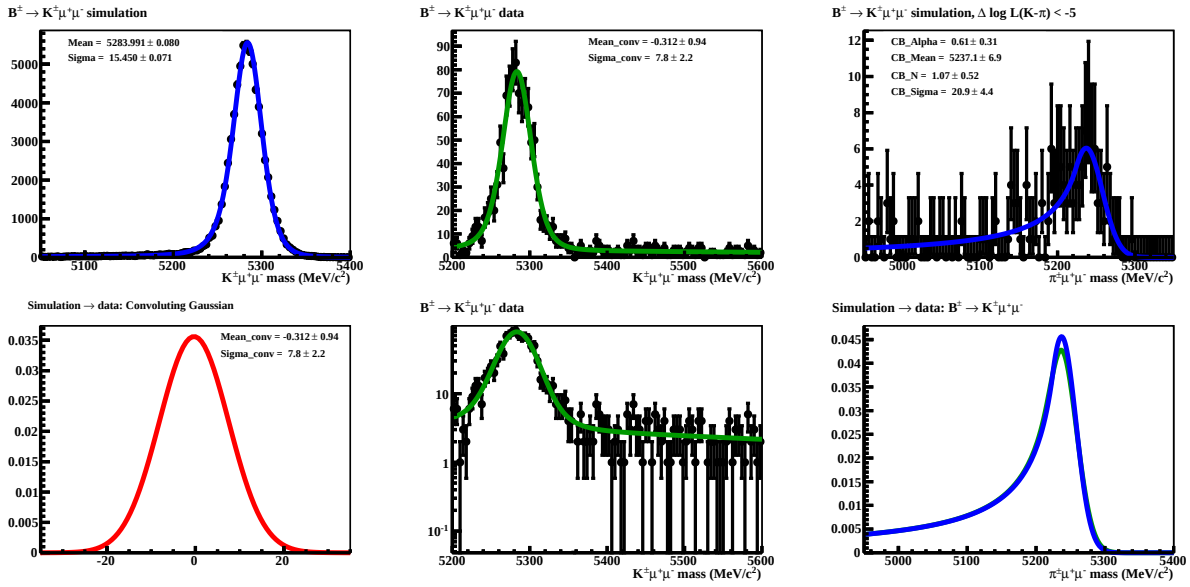

Figure 4.14: Determination of the convolution function necessary to correct simulation for data-simulation differences. Top left: $K^{\pm}\mu^{+}\mu^{-}$ mass peak fitted in simulation. Top centre: $K^{\pm}\mu^{+}\mu^{-}$ mass peak fitted in data, including a background function (seen on log scale, bottom centre). Bottom left: the convolution function necessary to translate from simulation to data. Top right: peaking background shape in simulation, fitted with a Crystal Ball. Bottom right: peaking background shape (blue) and when corrected for simulation-data differences (green).

Misidentified $B^{\pm} \to \pi^{\pm}\mu^{+}\mu^{-}$

The opposite misidentification also occurs, where $B^{\pm} \to \pi^{\pm}\mu^{+}\mu^{-}$ decays fall into the kaon-like subsample. Table 4.3 shows the efficiency of selecting pion events to be 75.3%, meaning that for a signal yield of 40 events, one expects approximately 10 misidentified events. The mass spectrum of $B^{\pm} \to \pi^{\pm}\mu^{+}\mu^{-}$ decays reconstructed under the kaon mass hypothesis is shown in Figure 4.15(b). This shape is expected to be unimportant because the size is smaller than the $K^{\pm}\mu^{+}\mu^{-}$ tail in that region. It is included in the fit nevertheless.

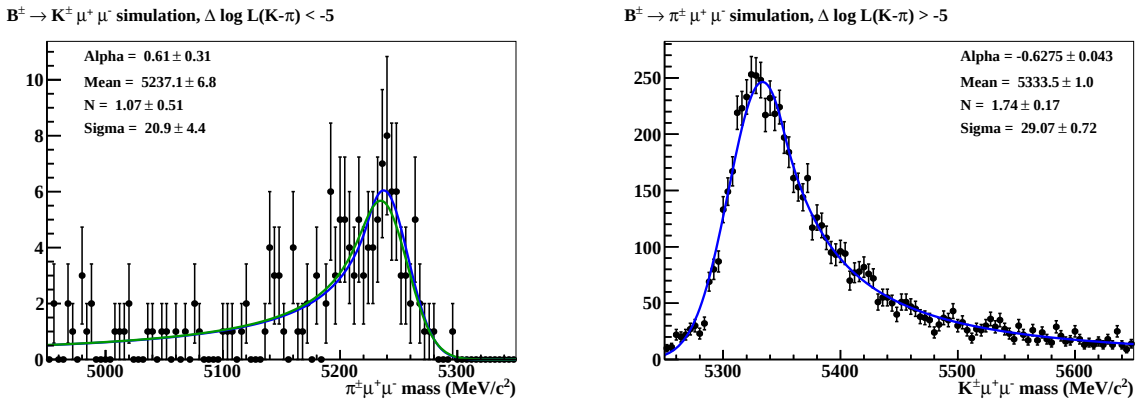

(a) (b)

Figure 4.15: a) Pion-like $B^{\pm} \to K^{\pm}\mu^{+}\mu^{-}$ decays from simulation reconstructed as $B^{\pm} \to \pi^{\pm}\mu^{+}\mu^{-}$. In blue: the fit to simulated events. In green: this fit adjusted for known data-simulation differences. b) Kaon-like $B^{\pm} \to \pi^{\pm}\mu^{+}\mu^{-}$ decays from simulation reconstructed as $B^{\pm} \to K^{\pm}\mu^{+}\mu^{-}$. Both distributions are fitted with a Crystal Ball shape.

4.4.2 Partially reconstructed backgrounds

As explained in Chapter 3, decays such as $B \to K^{*}(\to K\pi)\mu^{+}\mu^{-}$ can be partially reconstructed and enter the signal sample at low mass. The mass distributions of partially reconstructed decays are expected to be similar to those seen in the resonant analysis, and are therefore also accounted for using a bifurcated Gaussian shape. The same shape is used in both pion and kaon like samples, its parameters are allowed to float in the fit to data.

4.4.3 Combinatorial background

A linear polynomial is used to account for combinatorial background events. The same slope is used in pion and kaon-like subsamples, and is strongly constrained by the region above the B mass.

An exponential function was tested in the fit to data. No significant difference was seen between this and a linear function, given the size of the statistical uncertainties. A linear function was chosen to ensure better fit stability.

4.4.4 $B^{\pm} \to \pi^{\pm}\pi^{+}\pi^{-}$ background

Hadronic $B^{\pm} \to \pi^{\pm}\pi^{+}\pi^{-}$ decays can enter the signal sample if two pions of opposite charge are misidentified as muons. The pion and muon have very similar masses, so misidentified $B^{\pm} \to \pi^{\pm}\pi^{+}\pi^{-}$ decays sit close to the B signal peak, see Figure 4.16(a). There is a slight uncertainty in the shape of this background in data, as which of the two same sign pions was misidentified is unknown. Figures 4.16(b) and 4.16(c) show the boundary conditions, when the same sign pion with highest or lowest p_T is always misidentified. The parameters shown in these plots are averaged, scaled to represent data, and fixed in the signal extraction fit. Uncertainties in the shape are accounted for as a systematic.

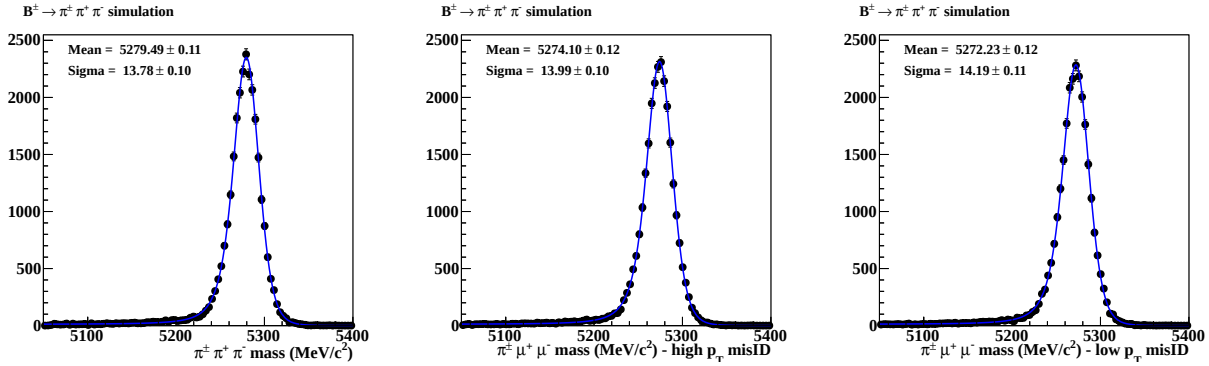

(a) (b) (c)

Figure 4.16: $B^{\pm} \to \pi^{\pm}\pi^{+}\pi^{-}$ mass distribution in simulation, fitted with a modified Gaussian (Equation 3.4). a) Correctly reconstructed. b) Reconstructed as $\pi^{\pm}\mu^{+}\mu^{-}$, with the highest p_T same sign pion misidentified. c) With the lowest p_T same sign pion misidentified.

The yield of this shape is also fixed. The identification efficiency of pions is measured in data from a clean D^{*} sample. The calibration sample is reweighted to match the kinematic distribution of the $\pi^{\pm}\pi^{+}\pi^{-}$ background, and required to pass the event selection. The calculated retention rate is 6×10^{-5}. Using the measured branching fraction $\mathcal{B}(B^{\pm} \to \pi^{\pm}\pi^{+}\pi^{-}) = (1.52 \pm 0.14) \times 10^{-5}$ [49] and the $b\bar{b}$ production cross section $\sigma(pp \to b\bar{b}X) = 284\,\mu\text{b}$ [107], $500,000$ $B^{\pm} \to \pi^{\pm}\pi^{+}\pi^{-}$ events are expected to decay within LHCb in $1\,\text{fb}^{-1}$. Assuming the same reconstruction and selection efficiency as for $B^{\pm} \to \pi^{\pm}\mu^{+}\mu^{-}$ (7%, see Table 4.6), 2.2 events are expected to enter the pion-like signal sample.

4.5 Signal extraction fit

Results are extracted from the data using a maximum likelihood fit (RooFit [99]). The parameters of interest are variables in the fit, so that the reported Minos error can be taken as the statistical uncertainty on each parameter.

4.5.1 Description of the fitter

There are two measurements of interest:

- the ratio between the number of $B^{\pm} \to \pi^{\pm}\mu^{+}\mu^{-}$ and $B^{\pm} \to K^{\pm}\mu^{+}\mu^{-}$ decays ($R^{\mu\mu}_{Raw}$);
- the normalised difference between the number of $B^{-} \to h^{-}\mu^{+}\mu^{-}$ and $B^{+} \to h^{+}\mu^{+}\mu^{-}$ decays ($A^{\mu\mu}_{Raw}$);

These are accessed by performing a 1D-fit of the B mass distribution of selected data, and counting the events within the peaks. $B^{\pm} \to \pi^{\pm}\mu^{+}\mu^{-}$ decays are separated from $B^{\pm} \to K^{\pm}\mu^{+}\mu^{-}$ decays by the $\Delta\log\mathcal{L}(K-\pi) < -5$ requirement. Charge asymmetries are accessed by partitioning the data into B^{+} and B^{-} samples. This results in two (π or K) or four (π or $K \times B^{-}$ or B^{+}) subsamples of the selected data, which are fit simultaneously in an unbinned manner.

Each subsample has five components:

1. Correctly reconstructed $B^{\pm} \to h^{\pm}\mu^{+}\mu^{-}$: The signal peaks are both fitted with a modified Gaussian lineshape (Equation 3.4), which share the same mean. The fit parameters float freely except for the width of the Cabibbo-supressed $B^{\pm} \to \pi^{\pm}\mu^{+}\mu^{-}$ peak, which is linked to the width of the higher statistics $B^{\pm} \to K^{\pm}\mu^{+}\mu^{-}$ peak via a fixed ratio 1.026 ± 0.010. This was measured from simulation, see Figure 4.13. The two tail parameters float freely, but the same parameters are used in both channels.

2. Misidentified $B^{\pm} \to h^{\pm}\mu^{+}\mu^{-}$: $B^{\pm} \to h^{\pm}\mu^{+}\mu^{-}$ decays which fall on the 'wrong' side of the $\Delta\log\mathcal{L}(K-\pi)$ split value are reconstructed with the incorrect hadron mass. They therefore form an auxiliary peak, adjacent to the signal peak of correctly reconstructed $B^{\pm} \to h^{\pm}\mu^{+}\mu^{-}$ decays. A Crystal Ball is used to model both of these shapes.

The shapes and yields of these misidentified peaks must be fixed, as they are undetectable under the larger signal peaks. Shape parameters are taken from Figures 4.15(a) and 4.15(b). Yields are taken as a fixed percentage of the correctly identified decays, according to the expected identification efficiency measured from data (see Table 4.3).

3. Partially reconstructed backgrounds from $B \to K^* \mu^+ \mu^-$ are seen at low mass. These decays are fitted with a Gaussian rise as mass decreases, for which the shape parameters float but are shared between subsamples, while the yields vary between the pion-like and kaon-like modes.

4. Combinatorial background is modelled as a linear polynomial, with the same gradient used in all subsamples.

5. Misidentified $B^\pm \to \pi^\pm \pi^+ \pi^-$ decays enter the dataset in the pion-like subsample. They are accounted for with a modified Gaussian of fixed shape and yield, see Section 4.4.4. This PDF is not used in the kaon-like subsample, where any misidentified decays would be undetectable under the Cabibbo-favoured $B^\pm \to K^\pm \mu^+ \mu^-$ decays.

Results of the fit are shown in 2 or 4 plots, depending on whether the charge split has been implemented. The top plot(s) show pion-like events, reconstructed under the $B^\pm \to \pi^\pm \mu^+ \mu^-$ hypothesis. The bottom plot(s) contain kaon-like events, reconstructed as $B^\pm \to K^\pm \mu^+ \mu^-$. If the charge split is used, B^- events are shown on the left, B^+ events on the right. Each plot contains various PDF shapes, each describing a component of the fit enumerated above (detailed in the figure caption).

4.5.2 Multiple candidates

Events in which more than one candidate decay exists are checked to see whether the two decay vertices are within 2 mm of each other in z. If so, the two candidates are deemed to be reconstructed from the same underlying decay, and the candidate with the best decay vertex χ^2 is kept, the other dismissed. 17 candidates are removed by this method.

4.5.3 Stability of the fit

The stability of the fit was tested by generating and fitting a series of pseudo-experiments. Pull distributions of the most important floating parameters are shown in Figure 4.17. These are consistent with a Gaussian of mean zero and unit width, demonstrating that the fit is stable under possible statistical fluctuations within the event sample.

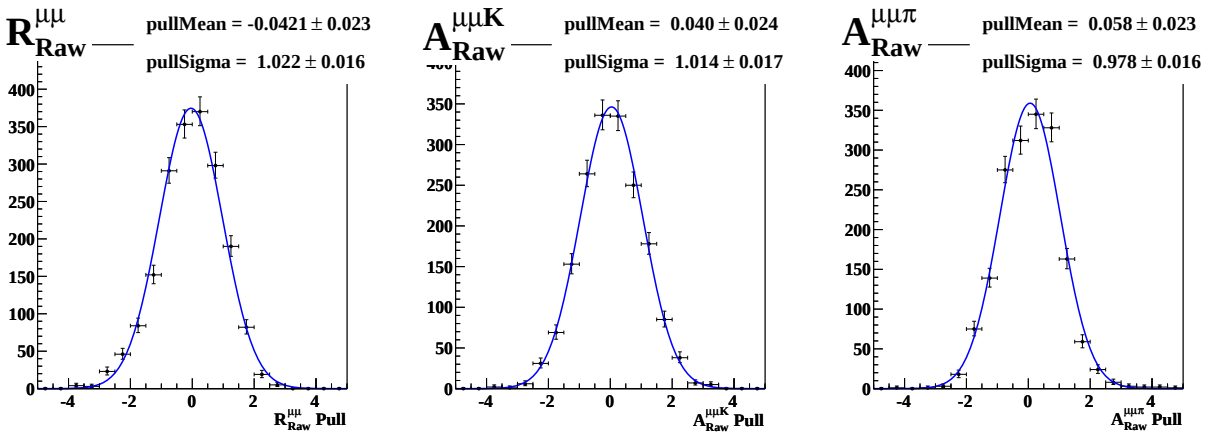

(a) (b) (c)

Figure 4.17: Pull distributions for the three measurements of interests, extracted from a series of pseudo-experiments in which the number of events has been statistically fluctuated.

4.5.4 Raw measurements

The charge averaged fit used to extract $R^{\mu\mu}_{Raw}$ is shown in Figure 4.18. 51 ± 8 $B^{\pm} \to \pi^{\pm}\mu^{+}\mu^{-}$ events are observed. When this fit is compared to the data fitted with the 'null' hypothesis (forcing 0 $B^{\pm} \to \pi^{\pm}\mu^{+}\mu^{-}$ events), the significance of the peak is found to be $(5.9 \pm 0.1)\sigma$. The uncertainty is determined by rerunning the fit to data while fluctuating fixed parameters within their uncertainties. The fit to data split by charge is shown in Figure 4.19. Table 4.5 summarises the fitted yields.

		$B^{\pm}$	B^{-}	B^{+}
$\mu^{+}\mu^{-}$	π	51 ± 8	24 ± 5	27 ± 6
	K	911 ± 31	456 ± 22	455 ± 22

Table 4.5: Raw fitted yields. The charge averaged totals are used to derive $R^{\mu\mu}_{Raw}$, the totals split by charge are used to calculate $A^{\mu\mu}_{Raw}$.

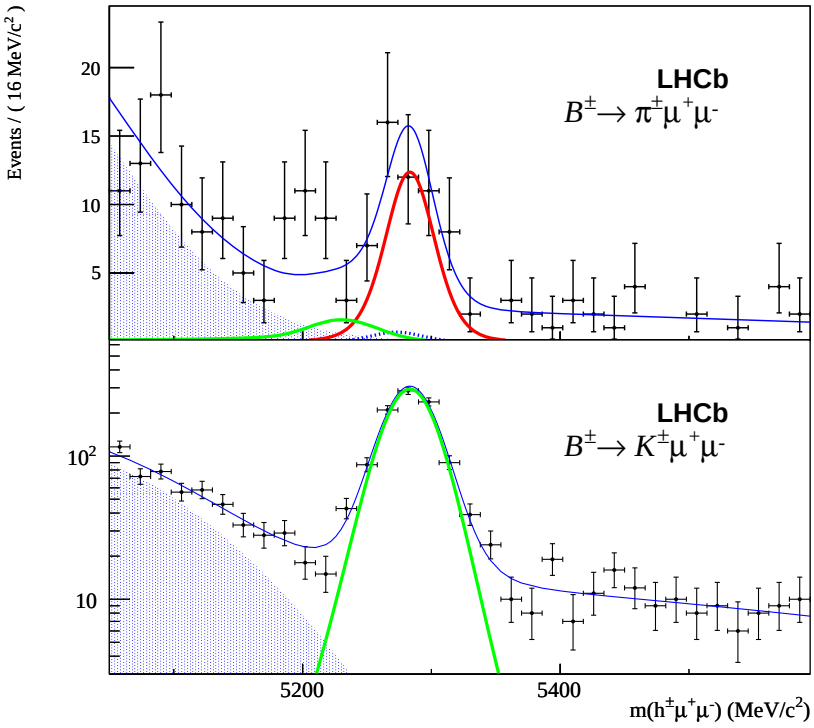

Figure 4.18: Fitted data used to extract $R^{\mu\mu}_{Raw}$. Top: Pion-like events. Bottom: Kaon-like events. The components of the fit are as follows: Solid red line: $B^{\pm} \to \pi^{\pm}\mu^{+}\mu^{-}$ decays. A modified Gaussian lineshape in the pion-like subsample, and an invisible Crystal Ball shape in the kaon-like subsample. Solid green line: $B^{\pm} \to K^{\pm}\mu^{+}\mu^{-}$ decays. A modified Gaussian lineshape in the kaon-like subsample, and a small Crystal Ball shape in the pion-like subsample. Blue shaded: Partially reconstructed background. Blue dotted line: $B^{\pm} \to \pi^{\pm}\pi^{+}\pi^{-}$ background. Not shown: linear combinatorial component. The sum of all component PDFs is shown as a solid blue line.

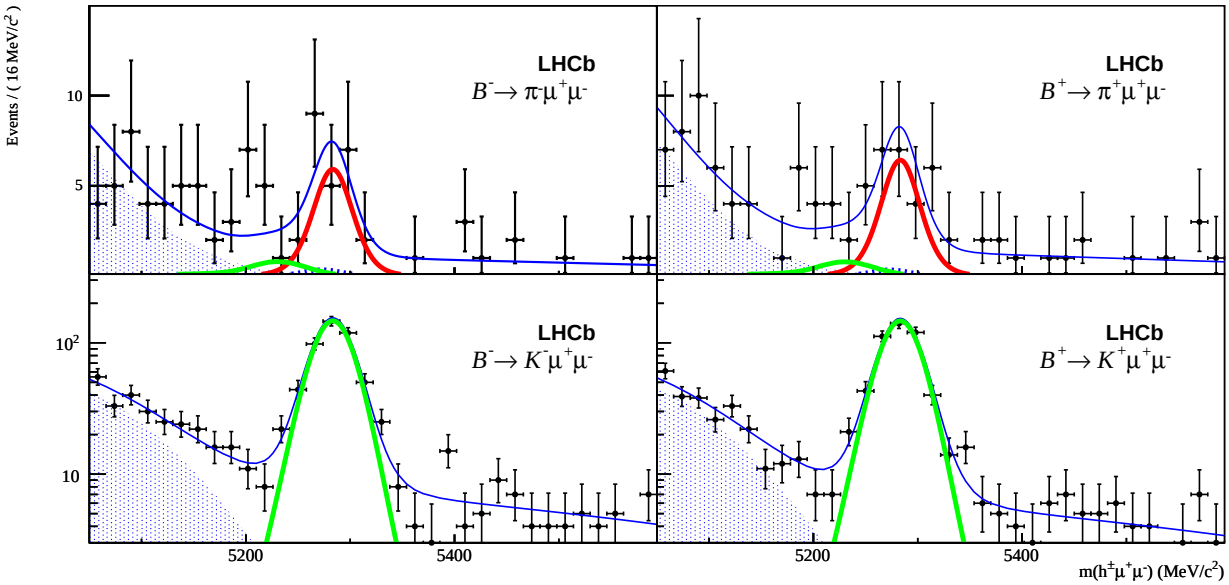

Figure 4.19: Fitted data, used to extract $A^{\mu\mu}_{Raw}$. Top: Pion-like events, showing the peak of $B^{\pm} \to \pi^{\pm}\mu^{+}\mu^{-}$ decays fitted in red. Bottom: Kaon-like events, with $B^{\pm} \to K^{\pm}\mu^{+}\mu^{-}$ decays fitted in green. Left: B^{-} decays. Right: B^{+} decays. For more details see Figure 4.18 caption.

4.5.5 Statistical uncertainty on $A_{Raw}^{\pi\mu\mu}$

Due to the small number of events defining the raw *CP* asymmetry of $B^{\pm} \to \pi^{\pm}\mu^{+}\mu^{-}$ decays, a Feldman Cousins technique was used to evaluate the statistical uncertainty on the fit result. Many pseudo-experiments were run, where the fitted asymmetry was compared to the asymmetry used to generate the dataset. This is presented in Figure 4.20 and shows that the true raw asymmetry is within 1σ of the measured raw asymmetry to 68.3% confidence level.

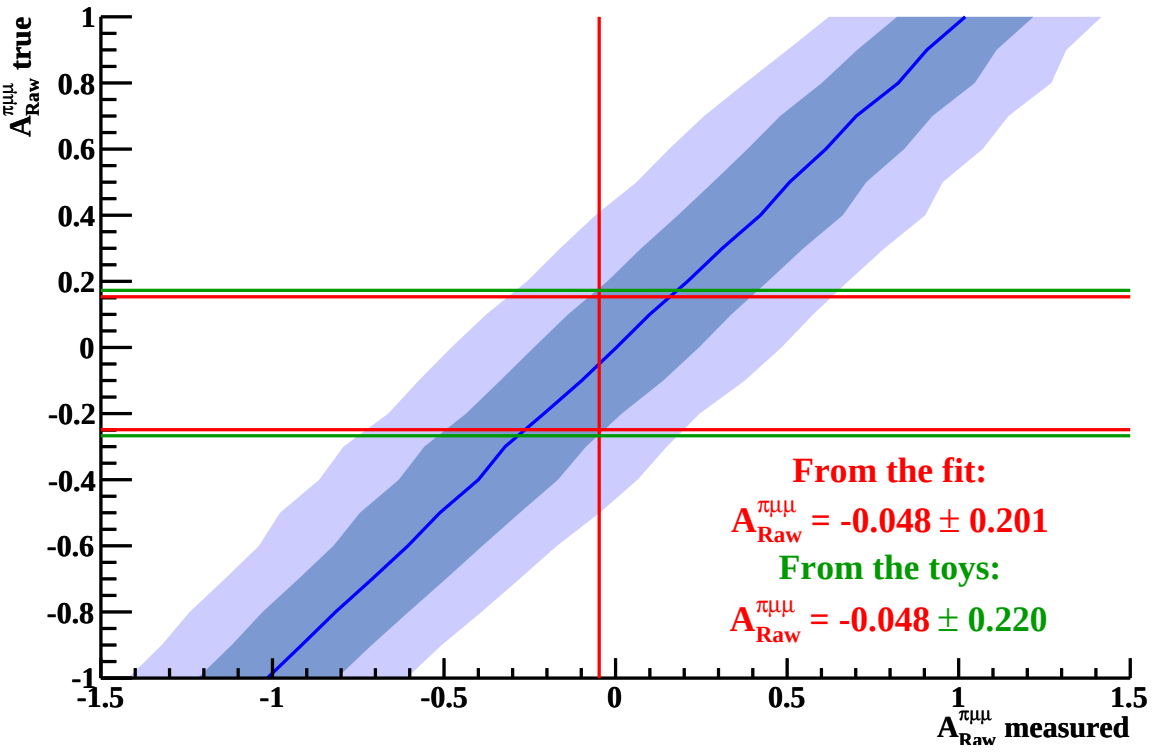

Figure 4.20: Variation of fitted $A_{Raw}^{\pi\mu\mu}$ measured in many pseudo-experiments. Each slice in $A_{Raw}^{\pi\mu\mu}$ true contains many pseudo-experiments which are fitted with a Gaussian to give the mean (solid blue line), the 1σ band (dark blue shading) and 2σ band (light blue shading). The measured *CP* asymmetry from data, with its reported statistical uncertainty is overlaid (red lines). The values of $A_{Raw}^{\pi\mu\mu}$ true for which the measured asymmetry intersects the 1σ band are also shown (green). These values are taken as the statistical uncertainty on the measured result.

4.6 Corrections

The $R^{\mu\mu}_{Raw}$ observable taken from the fit must be corrected by efficiency factors in order to conclude on the physics variable of interest.

The raw ratio of branching fractions taken from the fit must be corrected to take into account the relative geometric acceptance efficiency ($\omega^{\mu\mu}_{acc}$), the relative reconstruction and selection efficiency ($\omega^{\mu\mu}_{sel}$), and the relative trigger efficiency ($\omega^{\mu\mu}_{trig}$) of the decays in question:

$$R^{\mu\mu} = R^{\mu\mu}_{Raw}\,\omega^{\mu\mu}_{acc}\,\omega^{\mu\mu}_{sel}\,\omega^{\mu\mu}_{trig}\,, \tag{4.9}$$

where the relative efficiency is the ratio of the efficiencies (ϵ) of the two modes:

$$\omega^{\mu\mu} = \frac{\epsilon(B^{\pm} \to \mu^+\mu^- K^{\pm})}{\epsilon(B^{\pm} \to \mu^+\mu^- \pi^{\pm})}\,. \tag{4.10}$$

These corrections are now explained in detail.

4.6.1 Relative acceptance efficiency, $\omega^{\mu\mu}_{acc}$

The acceptance efficiency for $B^{\pm} \to \pi^{\pm}\mu^+\mu^-$ and $B^{\pm} \to K^{\pm}\mu^+\mu^-$ decays was studied with a generator-level[3] simulation. As in Section 3.7.1, the effect of requiring the decay products to be within the LHCb acceptance was measured. The ratio of acceptance efficiencies is found to be:

$$\omega^{\mu\mu}_{acc} = 1.038 \pm 0.007\,. \tag{4.11}$$

This is comparable to the ratios found in the $B^{\pm} \to \psi h^{\pm}$ analysis (Equation 3.10). This result is used to correct the measured $R^{\mu\mu}_{Raw}$ from the fit, to take into account the different acceptance efficiencies of the two decay modes.

The acceptance efficiency was studied as a function of dimuon mass. Figure 4.21 shows that the efficiency difference increases at high dimuon mass. This is in agreement with the

[3] PYTHIA [100] is used to generate the pp collision, and EVTGEN [69] (BtosllBall model) to describe the B meson decay.

findings of Section 3.7.1, where the $\psi(2S)$ correction was found to be larger than the J/ψ correction. Also shown is the dimuon mass spectrum of $B^{\pm} \to K^{\pm}\mu^{+}\mu^{-}$ before and after the LHCb acceptance is applied. The spectra are in agreement.

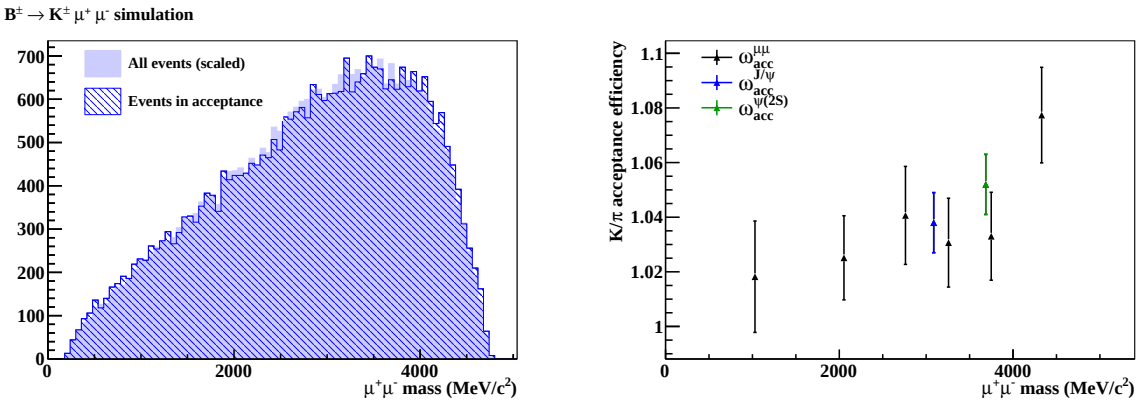

(a) (b)

Figure 4.21: Left: Dimuon mass spectrum of $B^{\pm} \to K^{\pm}\mu^{+}\mu^{-}$ before (red line) and after (black points) the decay products are required to be within the LHCb acceptance. Right: The acceptance efficiency correction as a function of dimuon mass. In black, values for $B^{\pm} \to h^{\pm}\mu^{+}\mu^{-}$, where the points are plotted at the barycentre of the dimuon mass bin. The ψ results from the previous chapter have been included and are in agreement with the non-resonant results.

4.6.2 Relative reconstruction and selection efficiency, $\omega_{sel}^{\mu\mu}$

The reconstruction and selection efficiencies are measured by applying the reconstruction and selection requirements to simulated samples of $B^{\pm} \to \pi^{\pm}\mu^{+}\mu^{-}$ and $B^{\pm} \to K^{\pm}\mu^{+}\mu^{-}$ decays, see Table 4.6. (The trigger efficiency is included in this section, and as expected is very close to 1 due to triggering only on the signal muons or event background.)

	$B^{\pm} \to \pi^{\pm}\mu^{+}\mu^{-}$ (%)	$B^{\pm} \to K^{\pm}\mu^{+}\mu^{-}$ (%)
Generated	770399	1042198
Pass stripping	150193 (19.5)	198076 (19.0)
Trigger	129691 (86.3)	168914 (85.3)
ψ and D vetoes	87326 (67.3)	115117 (68.2)
Multivariate analysis	54882 (62.8)	72268 (62.8)
Efficiency	0.0712	0.0693
Sim. stat. error	0.000304	0.000258
Efficiency ratio	0.973 ± 0.006	

Table 4.6: Efficiency of selections when applied to $B^{\pm} \to \pi^{\pm}\mu^{+}\mu^{-}$ and $B^{\pm} \to K^{\pm}\mu^{+}\mu^{-}$ simulation samples. Up and Down refer to the magnet polarity used in the simulation.

The uncertainties of the selection efficiencies are binomial, based on the finite size of the simulation samples. The reconstruction and selection efficiency correction is therefore:

$$\omega_{sel}^{\mu\mu} = 0.973 \pm 0.006\,. \tag{4.12}$$

4.6.3 Total correction to $R_{Raw}^{\mu\mu}$

Combining the acceptance, reconstruction, selection and trigger efficiency corrections, the total correction to $R_{Raw}^{\mu\mu}$ is:

$$\omega_{acc}^{\mu\mu}\,\omega_{sel}^{\mu\mu} = 1.010 \pm 0.009\,. \tag{4.13}$$

This factor scales the fitted $R_{Raw}^{\mu\mu}$ and its statistical uncertainty. The uncertainty on this correction factor is due to simulation statistics.

4.6.4 Charge asymmetry corrections

Corrections to the measured charge asymmetries are now discussed. In addition to any physics *CP* asymmetry, there are other asymmetries which affect the raw measurements:

- **Production asymmetry** (A_{Prod})**:**
  This accounts for the fact that B^+ ($\bar{b}u$) and B^- ($b\bar{u}$) mesons are likely to be produced at a different rate due to the excess of valence u quarks over $\bar{u}$ antiquarks in the pp collisions.

- **Detection asymmetry** (A_{Det}^{h})**:**
  Due to the LHCb detector being made of matter, the probability of detecting a hadron depends on its quark constituents (and so on its charge).

These additional asymmetries need to be taken into account when converting from the measured asymmetry ($A_{Raw}^{\mu\mu h}$) to the physics asymmetry ($A_{CP}^{\mu\mu h}$).

The observable asymmetry is to a good approximation, the sum of the contributing asymmetries,

$$A_{Raw}^{\mu\mu h} = A_{Prod} + A_{Det}^{h} + A_{CP}^{\mu\mu h} . \quad (4.14)$$

The production asymmetry is the same for both channels. In this analysis it was decided to take the measured production asymmetry from the $B^{\pm} \to J/\psi K^{\pm}$ channel (see Chapter 3), for which the charge asymmetry is already well determined [49]. The measured value of A_{Prod} is used to determine the physics asymmetry in the two non-resonant channels:

$$A_{CP}^{\mu\mu\pi} = A_{Raw}^{\mu\mu\pi} - A_{Prod} - A_{Det}^{\pi} \quad (4.15)$$

$$A_{CP}^{\mu\mu K} = A_{Raw}^{\mu\mu K} - A_{Prod} - A_{Det}^{K} \quad (4.16)$$

The kaon detection asymmetry term cancels from the definition of $A_{CP}^{\mu\mu K}$ when substituting Equation 3.17.

4.6.5 Hadron detection asymmetry

The same hadron detection asymmetries as in Section 3.7.6 are used:

$$A_{Det}^{K} = (-1.0 \pm 0.4)\%$$

$$A_{Det}^{\pi} = (0.0 \pm 0.4)\% , \quad (4.17)$$

as the momentum spectra of the hadrons in the resonant and non-resonant decay modes is very similar.

4.7 Systematic uncertainties

Systematic uncertainties are assigned to account for uncertainties in fixed fit parameters and the assumptions built into the correction factors. The systematic due to uncertainties in the fixed fit parameters is evaluated by varying each fixed parameter in a Gaussian manner

according to its uncertainty, and measuring the difference in measured $R^{\mu\mu}_{Raw}$. This is done with a toy dataset, the same data are fitted multiple times with varying fits.

The systematic uncertainties are summarised in Table 4.7. The following list of effects was considered:

- **Simulation uncertainty**

  Simulation is used to correct $R^{\mu\mu}_{Raw}$ for acceptance and selection efficiencies. This uncertainty represents the finite statistics of the simulation samples, and imperfections in the modelling of the relative detector response to pions and kaons.

- **PID efficiencies**

  The calculation of the pion and kaon PID efficiencies also contributes systematic uncertainties to the $R^{\mu\mu}_{Raw}$ results. The fraction of pion events which pass the $\Delta \log \mathcal{L}(K-\pi) < -5$ selection is fixed from data at $(75.0 \pm 0.5)\%$. The kaon selection efficiency is $(99.1 \pm 0.1)\%$.

- $A^{J/\psi K}_{CP}$ **(PDG)**

  The estimation of the production asymmetry is performed in the $B^{\pm} \to J/\psi K^{\pm}$ channel, using the nominal value of $A^{J/\psi K}_{CP}$, the measured $A^{J/\psi K}_{Raw}$ and the kaon detector asymmetry.

  An uncertainty in the asymmetry measurements comes from uncertainty on the world average value of $A^{J/\psi K}_{CP}$, which is fixed to the PDG value [49]:

  $$A^{J/\psi K}_{CP} = (1 \pm 7) \times 10^{-3} \,. \tag{4.18}$$

  A systematic equal to the uncertainty on this value is assigned.

- $A^{J/\psi K}_{Raw}$ **statistical uncertainty**

  The fitted value of $A^{J/\psi K}_{Raw}$ contributes to the production asymmetry determination. Therefore, the statistical uncertainty on this measurement is used as a systematic uncertainty in the asymmetry results.

- **Detection asymmetries**

  The pion and kaon detection asymmetries must be used to obtain the $A_{CP}^{\mu\mu\pi}$ results. The uncertainty on both asymmetries is 0.004 (see Section 3.7.6). In the $A_{CP}^{\mu\mu K}$ analysis, the detector asymmetries cancel between this and the $A_{CP}^{J/\psi K}$ channel in which the production asymmetry is measured. Therefore, neglecting small variations as a function of kaon momentum, no systematic is required.

- **Fixed fit parameters**

  Various parameters of the fit are fixed to prevent instability, such as the line shape of the misidentified $B^{\pm} \to h^{\pm}\mu^{+}\mu^{-}$ decays. These fixed parameters were varied within their uncertainties, and the fit rerun. A large contribution comes from the yield of misidentified $B^{\pm} \to \pi^{\pm}\pi^{+}\pi^{-}$ decays, which is estimated as 2 ± 2 events.

	$R^{\mu\mu}(\times 10^{-2})$	$A^{\mu\mu\pi}$	$A^{\mu\mu K}$
Simulation uncertainty	0.064	-	-
$A^{J/\psi K}$ (PDG [49])	-	0.0070	0.0070
$A_{\rm Raw}^{J/\psi K}$ statistical error	-	0.0046	0.0046
Detection asymmetries	-	0.0056	-
Ratio of signal widths	0.178	0.0237	0.0031
Pion $\epsilon(\Delta \log \mathcal{L})$	0.023	0.0217	0.0006
Kaon $\epsilon(\Delta \log \mathcal{L})$	0.060	0.0182	0.0042
MisID'd $K^{\pm}\mu^{+}\mu^{-}$ shape	0.125	0.0266	0.0018
MisID'd $\pi^{\pm}\mu^{+}\mu^{-}$ shape	0.038	0.0121	0.0035
$\pi^{\pm}\pi^{+}\pi^{-}$ yield and shape	0.208	0.0447	0.0040
Sum in quadrature (syst.)	0.317	0.0657	0.0114
Fit error (stat.)	1.220	0.2010	0.0360

Table 4.7: Summary of systematic uncertainties, and their sum in quadrature for each measurement. Statistical uncertainties from the fit are included for comparison.

4.8 Results

The decay $B^{\pm} \to \pi^{\pm}\mu^{+}\mu^{-}$ is observed for the first time. The measured ratio of branching fractions with the Cabibbo favoured $B^{\pm} \to K^{\pm}\mu^{+}\mu^{-}$ decay is

$$R^{\mu\mu} \;=\; (5.69 \pm^{1.28}_{1.18} \pm 0.32) \times 10^{-2}\,,$$

where the first uncertainty is statistical and the second systematic. Normalising to the recent LHCb measurement of the branching fraction of $B^{\pm} \to K^{\pm}\mu^{+}\mu^{-}$ decays [59]:

$$\mathcal{B}(B^{\pm} \to \pi^{\pm}\mu^{+}\mu^{-}) = (2.48 \pm^{0.57}_{0.52} \pm 0.17) \times 10^{-8}\,. \tag{4.19}$$

This is in agreement with SM theoretical predictions (Section 1.8). The ratio of CKM matrix elements is determined from Equation 1.48 to be:

$$\frac{|V_{td}|}{|V_{ts}|} = 0.274 \pm^{0.031}_{0.028} \pm 0.008\,. \tag{4.20}$$

This result has 2σ separation from the averaged result from neutral B meson mixing shown in Equation 1.46.

The measured CP asymmetries are

$$\begin{aligned} A_{CP}^{\mu\mu\pi} &= -0.045 \pm 0.220 \pm 0.066 \\ A_{CP}^{\mu\mu K} &= 0.014 \pm 0.036 \pm 0.012\,, \end{aligned}$$

where again the first uncertainty is statistical and the second systematic. The CP asymmetry measurement in $B^{\pm} \to \pi^{\pm}\mu^{+}\mu^{-}$ decays is the first of its kind. The measurement in the $B^{\pm} \to K^{\pm}\mu^{+}\mu^{-}$ channel is the world's most precise, and is consistent with previous results. The CP asymmetries were also calculated in bins of dimuon mass, see Figure 4.22.

4.8.1 Comparison with the published LHCb analysis

The work in this chapter is an independent analysis of $B^{\pm} \to \pi^{\pm}\mu^{+}\mu^{-}$ decays. The same dataset was used in collaboration to produce a published analysis [4] on a shorter timescale. The methods of the two analyses differ: the published analysis normalises to $B^{\pm} \to J/\psi\, K^{\pm}$ decays instead of $B^{\pm} \to K^{\pm}\mu^{+}\mu^{-}$ decays. Both analyses employ a BDT to separate signal from background, however the training datasets and working points were chosen differently. The fit procedure of the two analyses is quite different, due to the alternative choice of control channels ($J/\psi\, K^{\pm}$ vs. $K^{\pm}\mu^{+}\mu^{-}$). Comparisons are now drawn between the two results.

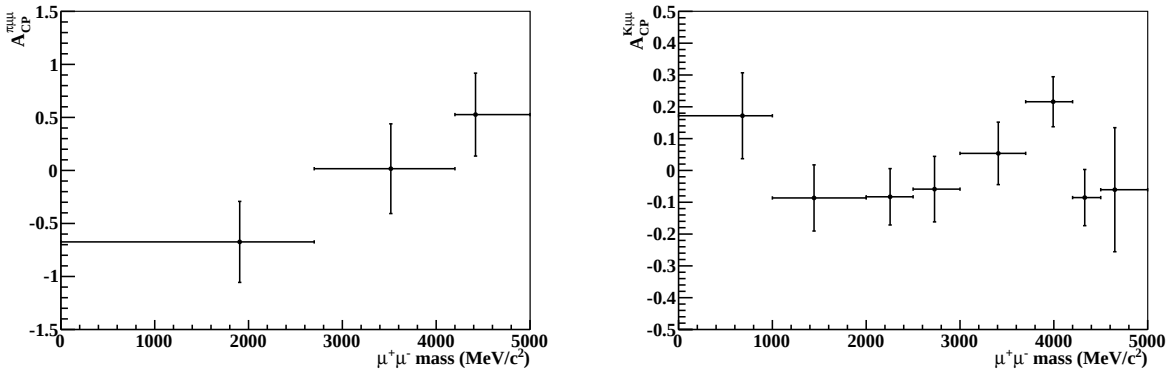

(a) (b)

Figure 4.22: *CP* asymmetries of $B^{\pm} \to \pi^{\pm}\mu^{+}\mu^{-}$ decays (a) and $B^{\pm} \to K^{\pm}\mu^{+}\mu^{-}$ decays (b) in bins of dimuon mass. Bins were chosen to have roughly equal number of events. Horizontal error bars show the bin widths, the results are plotted at the barycentre of each bin. The uncertainties on the asymmetries are statistical only, and are taken from the fit.

In the published analysis, $B^{\pm} \to \pi^{\pm}\mu^{+}\mu^{-}$ decays were observed for the first time at LHCb with 5.2 σ significance, using the full 2011 dataset [4]. In total, $25.3^{+6.7}_{-6.4}$ candidates were fitted, see Figure 4.23. The measured ratio of branching fractions in this analysis was $(5.4 \pm 1.4 \pm 0.3) \times 10^{-2}$, giving a branching fraction of $(2.4 \pm 0.6 \pm 0.2) \times 10^{-8}$ and an estimation of $|V_{td}/V_{ts}|$ of $0.270 \pm 0.035 \pm 0.008$. These results are compatible with theoretical predictions, previous measurements and the results of the independent analysis detailed in this thesis.

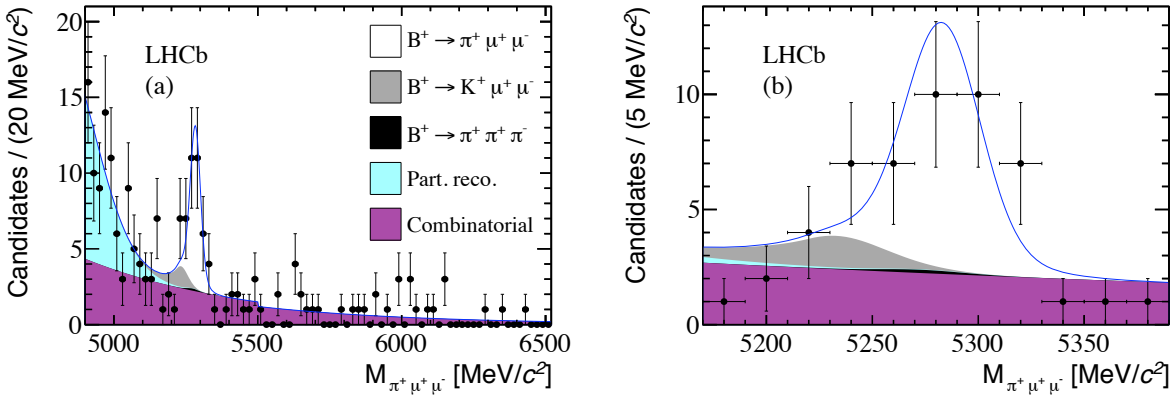

(a) (b)

Figure 4.23: Invariant mass distribution of $B^{\pm} \to \pi^{\pm}\mu^{+}\mu^{-}$ candidates with the fit overlaid (a) in the full mass range and (b) in the region around the B mass. In the legend, 'part. reco.' and 'combinatorial' refer to partially reconstructed and combinatorial backgrounds respectively. The discontinuity at 5500 MeV/c^2 is from the removal of data used for training the BDT. Taken from [4].

Appendix A

Symmetries

Symmetries play an important role in physics. Noether's Theorem describes how continuous symmetries imply invariance under certain translations. Specifically, symmetry in translation through time implies energy conservation, symmetry in rotation implies conservation of angular momentum, and symmetry in translation through space implies conservation of momentum.

In addition to these continuous symmetries, three discrete symmetries are relevant to particle physics [108]:

- Charge, C

  Charge symmetry implies invariance under charge conjugation, or the reversal of electromagnetic charge. Particles and antiparticles carry opposite electric charge. C symmetry asserts that each particle and antiparticle pair will feel the same magnitude of force in a magnetic field.

- Parity, P

  Parity symmetry implies invariance under the inversion of spatial coordinates. P symmetry asserts that the observer should be unable to detect a difference between watching processes with and without the spatial coordinates reversed. Of particular relevance to particle physics: inverting spatial coordinates inverses the handedness of systems, and inverts the sign of the helicity of the particle. The weak force violates parity conservation.

- Direction of time, T

  The discrete time symmetry implies invariance under the reversal of time. It asserts that watching a process in reverse should be described by the same laws as the original process.[1] The direction of time symmetry relates to the symmetry between matter and antimatter, as particles can be described as travelling forward through time, and antiparticles backward through time.

Symmetries can be combined. For example, the weak force violates P symmetry, but conserves CP symmetry almost perfectly. The small amount of CP violation present in the weak force demonstrates an asymmetry between matter and antimatter

The combination of CPT symmetries is thought to be conserved by all physical systems. Violation of the CPT symmetry implies violation of Lorentz invariance, upon which the SM is built. CPT symmetry has been tested in many experiments, summarised in [109]. No definitive violation of CPT symmetry has been measured. Recent results from the OPERA collaboration, which measured the speed of neutrinos as being faster than the speed of light, would constitute CPT violation. However this result was later found to be erroneous and revised to be consistent with the speed of light [110].

CP violation has been seen in particle physics processes (see Section 1.3). To preserve CPT symmetry, this implies that T violation must also occur, for example meaning that reaction processes happen quicker in one direction than the other. Time reversal violation has been observed by the BABAR collaboration in the B^0 meson system [111]. The analysis uses entangled B^0 and $\bar{B}^0$ states. The time of the first decay t_1 and its flavour are tagged, meaning at that time the other B meson's state is known. The second meson decays at time t_2, perhaps having oscillated (changed CP state) since t_1. Time reversal symmetry is tested by comparing $\bar{B}^0(t_1) \to B^0(t_2)$ with $B^0(t_1) \to \bar{B}^0(t_2)$ [112].

[1] Time symmetry does not hold at the macroscopic level, as the second law of thermodynamics causes the entropy of an ensemble of particles to increase with time. However, this doesn't imply time-reversal asymmetry in the laws of microscopic physics.

Appendix B

Track clone B mass

The reconstructed B candidate is the sum of the pion and ψ 4-momenta. Using $m^2 = E^2 - p^2$, where p is the momentum 3-vector:

$$\begin{aligned} m_B^2 &= E_B^2 - p_B^2 \\ &= (E_\pi + E_\psi)^2 - (p_\pi + p_\psi)^2 \,. \end{aligned} \tag{B.1}$$

Expanding and rearranging terms:

$$\begin{aligned} m_B^2 &= E_\pi^2 + 2E_\pi E_\psi + E_\psi^2 - p_\pi^2 - 2p_\pi \cdot p_\psi - p_\psi^2 \\ &= E_\pi^2 - p_\pi^2 + E_\psi^2 - p_\psi^2 + 2E_\pi E_\psi - 2p_\pi \cdot p_\psi \\ &= m_\pi^2 + m_\psi^2 + 2E_\pi E_\psi - 2p_\pi \cdot p_\psi \,. \end{aligned} \tag{B.2}$$

The ψ can be similarly deconstructed into its constituent $\mu_1\mu_2$ objects:

$$\begin{aligned} m_B^2 = m_\pi^2 + m_\psi^2 + 2E_\pi(E_{\mu_1} + E_{\mu_2}) &- 2p_\pi \cdot (p_{\mu_1} + p_{\mu_2}) \\ &- 2p_{\mu_2} \cdot (p_{\mu_1} + p_{\mu_2}) \\ &- 2p_{\mu_2}^2 - 2p_{\mu_1} \cdot p_{\mu_2} \,, \end{aligned} \tag{B.3}$$

where the substitution $p_\pi = p_{\mu_2}$ has been made due to the track clone.

Expanding the ψ in terms of its constituent $\mu_1\mu_2$ parts:

$$\begin{aligned} m_\psi^2 &= (E_{\mu_1} + E_{\mu_2})^2 - (p_{\mu_1} + p_{\mu_2})^2 \\ &= E_{\mu_1}^2 + 2E_{\mu_1}E_{\mu_2} + E_{\mu_2}^2 - p_{\mu_1}^2 - 2p_{\mu_1} \cdot p_{\mu_2} - p_{\mu_2}^2 \\ &= m_{\mu_1}^2 + m_{\mu_2}^2 + 2E_{\mu_1}E_{\mu_2} - 2p_{\mu_1} \cdot p_{\mu_2} \,. \end{aligned} \tag{B.4}$$

The subscript indices on m_{μ_i} may be dropped. Therefore:

$$-2p_{\mu_1} \cdot p_{\mu_2} = m_\psi^2 - 2m_\mu^2 - 2E_{\mu_1}E_{\mu_2} \,, \tag{B.5}$$

which can be substituted into Equation B.3:

$$\begin{aligned} m_B^2 = m_\pi^2 + m_\psi^2 + 2E_\pi(E_{\mu_1} + E_{\mu_2}) &- 2(E_{\mu_2}^2 - m_{\mu_2}^2) + m_\psi^2 - 2m_\mu^2 - 2E_{\mu_1}E_{\mu_2} \\ &- 2E_{\mu_2}^2 + m_\psi^2 - 2E_{\mu_1}E_{\mu_2} \,. \end{aligned} \tag{B.6}$$

Now overall:

$$\begin{aligned} m_B^2 &= 2m_\psi^2 + m_\pi^2 + 2E_\pi(E_{\mu_1} + E_{\mu_2}) - 2E_{\mu_2}(E_{\mu_2} + E_{\mu_1}) \\ &= 2m_\psi^2 + m_\pi^2 + 2(E_\pi - E_{\mu_2})(E_{\mu_1} + E_{\mu_2}) \,. \end{aligned} \tag{B.7}$$

A further substitution can be made, once again using the fact that $p_\pi = p_{\mu_2}$:

$$\begin{aligned} E_\pi^2 - m_\pi^2 &= E_{\mu_2}^2 - m_{\mu_2}^2 \\ E_\pi &= \sqrt{E_{\mu_2}^2 - m_{\mu_2}^2 + m_\pi^2} \\ &= E_{\mu_2}\sqrt{1 + \frac{m_\pi^2 - m_{\mu_2}^2}{E_{\mu_2}^2}} \,. \end{aligned} \tag{B.8}$$

At this point a Taylor expansion can be used to approximate:

$$\sqrt{1+x} \approx 1 + \frac{1}{2}x \,, \tag{B.9}$$

for $|x| < 1$. As the muon and pion are light and the collision energy is high, this condition is satisfied. Therefore:

$$\sqrt{1 + \frac{m_\pi^2 - m_{\mu_2}^2}{E_{\mu_2}^2}} \approx 1 + \frac{m_\pi^2 - m_{\mu_2}^2}{2E_{\mu_2}^2}\,, \tag{B.10}$$

and from Equation B.8:

$$E_\pi \approx E_{\mu_2} + \frac{m_\pi^2 - m_{\mu_2}^2}{2E_{\mu_2}}\,. \tag{B.11}$$

This can be substituted into Equation B.7:

$$\begin{aligned} m_B^2 &\approx 2m_\psi^2 + m_\pi^2 + 2\frac{m_\pi^2 - m_{\mu_2}^2}{2E_{\mu_2}}(E_{\mu_1} + E_{\mu_2}) \\ &\approx 2m_\psi^2 + m_\pi^2 + (m_\pi^2 - m_\mu^2)\left(\frac{E_{\mu_1}}{E_{\mu_2}} + 1\right)\,, \end{aligned} \tag{B.12}$$

or:

$$m_B \approx \sqrt{2m_\psi^2 + m_\pi^2 + (m_\pi^2 - m_\mu^2)\left(\frac{E_{\mu_1}}{E_{\mu_2}} + 1\right)}\,, \tag{B.13}$$

as shown in Equation 3.3.

Appendix C

Preselected $B^{\pm} \to \pi^{\pm}\mu^{+}\mu^{-}$ plots

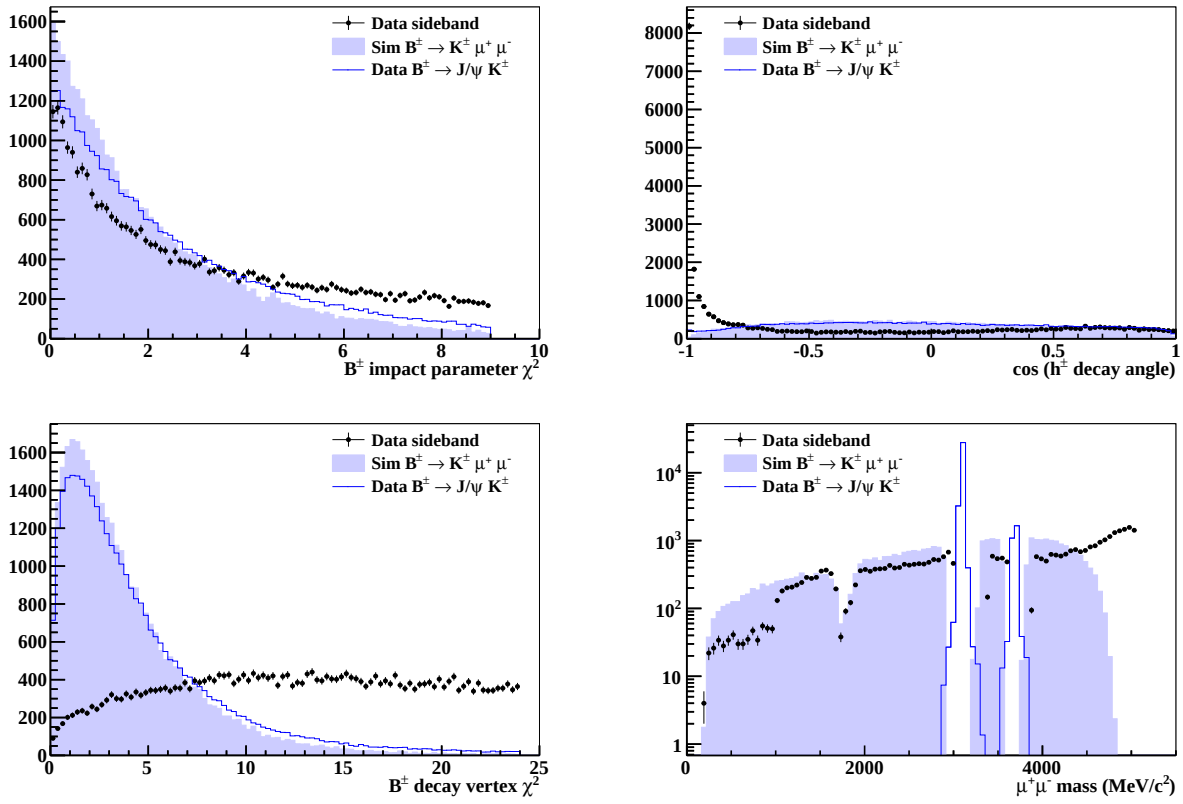

Figure C.1: Comparison between $B^{\pm} \to J/\psi K^{\pm}$ events in 2011 data, $B^{\pm} \to K^{\pm}\mu^{+}\mu^{-}$ simulation and data sideband. Simulation (shaded blue) and J/ψ data (blue line) are scaled to have the same entries per plot as the data (black points).

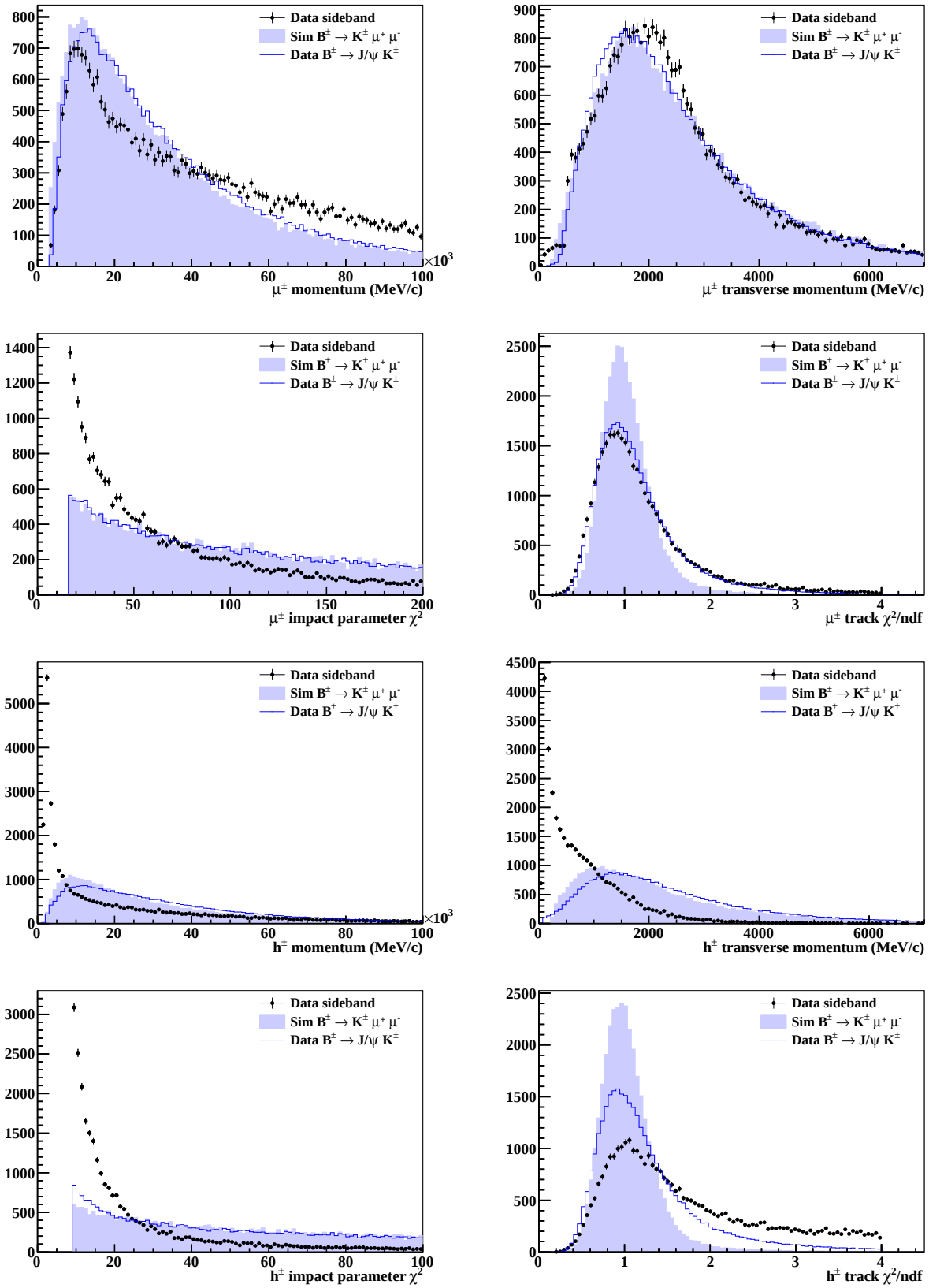

Figure C.2: Comparison between $B^{\pm} \to J/\psi K^{\pm}$ events in 2011 data, $B^{\pm} \to K^{\pm}\mu^{+}\mu^{-}$ simulation and data sideband. For details see Figure C.1 caption.

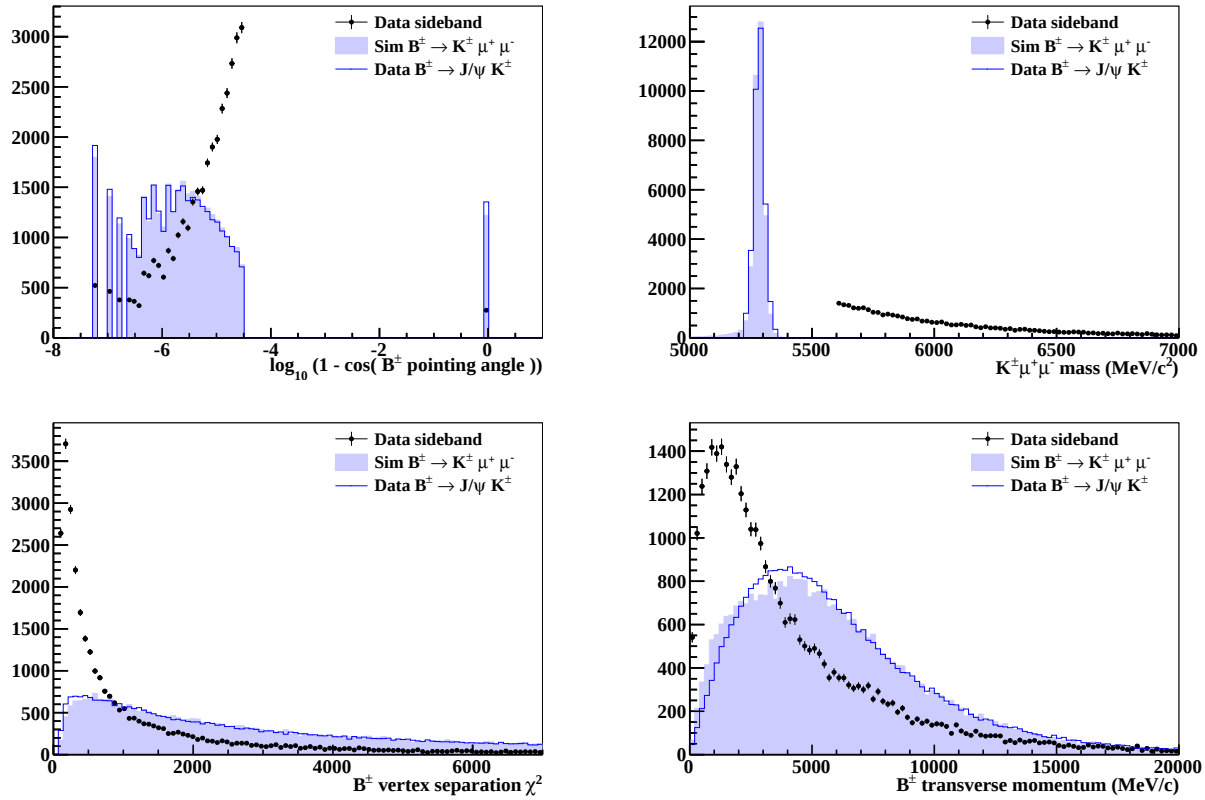

Figure C.3: Comparison between $B^{\pm} \to J/\psi K^{\pm}$ events in 2011 data, $B^{\pm} \to K^{\pm}\mu^{+}\mu^{-}$ simulation and data sideband. For details see Figure C.1 caption.

Bibliography

[1] S. Redford, *LHCb VELO Closing Control, Vertex Resolution and Luminosity Measurement*, *PoS* **VERTEX2010** (2010) 018.

[2] LHCb Collaboration, R. Aaij et al., *Absolute luminosity measurements with the LHCb detector at the LHC*, *JINST* **7** (2012) P01010, [arXiv:1110.2866].

[3] LHCb Collaboration, R. Aaij et al., *Measurements of the branching fractions and CP asymmetries of $B^+ \to J/\psi\,\pi^+$ and $B^+ \to \psi(2S)\pi^+$ decays*, *Phys.Rev.* **D85** (2012) 091105, [arXiv:1203.3592].

[4] LHCb Collaboration, R. Aaij et al., *First observation of the decay $B^+ \to \pi^+\mu^+\mu^-$*, arXiv:1210.2645.

[5] P. Dirac, *The Quantum Theory of the Electron*, *Proc.R.Soc.* **A117** (1928) 610–624.

[6] C. D. Anderson, *The Positive Electron*, *Phys.Rev.* **43** (1933) 491–494.

[7] ATLAS Collaboration, G. Aad et al., *Observation of a new particle in the search for the Standard Model Higgs boson with the ATLAS detector at the LHC*, *Phys.Lett.* **B716** (2012) 1–29, [arXiv:1207.7214].

[8] CMS Collaboration, S. Chatrchyan et al., *Observation of a new boson at a mass of* 125 GeV *with the CMS experiment at the LHC*, *Phys.Lett.* **B716** (2012) 30–61, [arXiv:1207.7235].

[9] J. C. Maxwell, *A dynamical theory of the electromagnetic field*, *Phil.Trans.* **155** (1865) 459–513.

[10] S. L. Glashow, J. Iliopoulos, and L. Maiani, *Weak Interactions with Lepton-Hadron Symmetry*, *Phys.Rev.* **D2** (1970) 1285–1292.

[11] S. Weinberg, *A Model of Leptons*, *Phys.Rev.Lett.* **19** (1967) 1264–1266.

[12] A. Salam, *Elementary Particle Theory*. Almquist and Wiksells, 1969.

[13] LIGO Scientific Collaboration, Virgo Collaboration, J. Abadie et al., *All-sky search for gravitational-wave bursts in the second joint LIGO-Virgo run*, *Phys.Rev.* **D85** (2012) 122007, [arXiv:1202.2788].

[14] V. C. Rubin, W. K. J. Ford, and N. Thonnard, *Rotational properties of 21 Sc galaxies with a large range of luminosities and radii, from NGC 4605 (R = 4kpc) to UGC 2885 (R = 122 kpc)*, *Astrophys.J.* **238** (1980) 471–487.

[15] D. Clowe et al., *A direct empirical proof of the existence of dark matter*, *Astrophys.J.* **648** (2006) 109–113, [arXiv:astro-ph/0608407].

[16] DAMA Collaboration, LIBRA Collaboration, R. Bernabei et al., *New results from DAMA/LIBRA*, *Eur.Phys.J.* **C67** (2010) 39–49, [arXiv:1002.1028].

[17] CDMS-II Collaboration, CDMS Collaboration, Z. Ahmed et al., *Search for inelastic dark matter with the CDMS II experiment*, *Phys.Rev.* **D83** (2011) 112002, [arXiv:1012.5078].

[18] Supernova Search Team, A. G. Riess et al., *Observational evidence from supernovae for an accelerating universe and a cosmological constant*, *Astron.J.* **116** (1998) 1009–1038, [arXiv:astro-ph/9805201].

[19] N. Jarosik et al., *Seven-Year Wilkinson Microwave Anisotropy Probe (WMAP) Observations: Sky Maps, Systematic Errors, and Basic Results*, *Astrophys.J.Suppl.* **192** (2011) 14, [arXiv:1001.4744].

[20] A. D. Sakharov, *Violation of CP invariance, C asymmetry, and baryon asymmetry of the universe*, *Sov.Phys.Usp.* **34** (1991), no. 5 392.

[21] P. Huet and E. Sather, *Electroweak baryogenesis and standard model CP violation*, *Phys.Rev.* **D51** (1995) 379–394, [arXiv:hep-ph/9404302].

[22] S. Dimopoulos and H. Georgi, *Softly broken supersymmetry and SU(5)*, *Nucl.Phys.* **B193** (1981), no. 1 150 – 162.

[23] ATLAS Collaboration, G. Aad et al., *Search for squarks and gluinos using final states with jets and missing transverse momentum with the ATLAS detector in* $\sqrt{s} = 7\,\text{TeV}$ *proton-proton collisions*, *Phys.Lett.* **B701** (2011) 186–203, [arXiv:1102.5290].

[24] CMS Collaboration, V. Khachatryan et al., *Search for Supersymmetry in pp Collisions at* 7 TeV *in Events with Jets and Missing Transverse Energy*, *Phys.Lett.* **B698** (2011) 196–218, [arXiv:1101.1628].

[25] N. Sakai and T. Yanagida, *Proton decay in a class of supersymmetric grand unified models*, *Nucl.Phys.* **B197** (1982), no. 3 533 – 542.

[26] SNO Collaboration, S. Ahmed et al., *Constraints on nucleon decay via 'invisible' modes from the Sudbury Neutrino Observatory*, *Phys.Rev.Lett.* **92** (2004) 102004, [arXiv:hep-ex/0310030].

[27] J. Ellis, J. Hagelin, D. Nanopoulos, K. Olive, and M. Srednicki, *Supersymmetric relics from the big bang*, *Nucl.Phys.* **B238** (1984), no. 2 453 – 476.

[28] H. Yukawa, *On the Interaction of Elementary Particles*, *Progr.Theoret.Phys.Suppl.* **1** (1955) 1–10.

[29] T. D. Lee and C. N. Yang, *Question of Parity Conservation in Weak Interactions*, *Phys.Rev.* **104** (1956) 254–258.

[30] C. S. Wu, E. Ambler, R. W. Hayward, D. D. Hoppes, and R. P. Hudson, *Experimental Test of Parity Conservation in Beta Decay*, *Phys.Rev.* **105** (1957) 1413–1415. Copyright 1957 by the American Physical Society.

[31] R. L. Garwin, L. M. Lederman, and M. Weinrich, *Observations of the Failure of Conservation of Parity and Charge Conjugation in Meson Decays: the Magnetic Moment of the Free Muon*, *Phys.Rev.* **105** (1957) 1415–1417. Copyright 1957 by the American Physical Society.

[32] Gargamelle Neutrino Collaboration, F. Hasert et al., *Search for elastic muon-neutrino electron scattering*, *Phys.Lett.* **B46** (1973) 121–124.

[33] Gargamelle Neutrino Collaboration, F. Hasert et al., *Observation of Neutrino Like Interactions Without Muon Or Electron in the Gargamelle Neutrino Experiment*, *Phys.Lett.* **B46** (1973) 138–140.

[34] UA1 Collaboration, G. Arnison et al., *Experimental observation of isolated large transverse energy electrons with associated missing energy at* $\sqrt{s} = 540\,\text{GeV}$, *Phys.Lett.* **B122** (1983), no. 1 103 – 116.

[35] UA1 Collaboration, G. Arnison et al., *Experimental observation of lepton pairs of invariant mass around* $95\,\text{GeV}/c^2$ *at the CERN SPS collider*, *Phys.Lett.* **B126** (1983), no. 5 398 – 410.

[36] UA2 Collaboration, M. Banner et al., *Observation of single isolated electrons of high transverse momentum in events with missing transverse energy at the CERN* $\bar{p}p$ *collider*, *Phys.Lett.* **B122** (1983), no. 5-6 476 – 485.

[37] UA2 Collaboration, P. Bagnaia et al., *Evidence for* $Z^0 \to e^+e^-$ *at the CERN* $\bar{p}p$ *collider*, *Phys.Lett.* **B129** (1983), no. 1-2 130 – 140.

[38] Particle Data Group, J. Beringer et al., *Review of particle physics*, *Phys.Rev.* **D86** (2012) 010001.

[39] J. H. Christenson, J. W. Cronin, V. L. Fitch, and R. Turlay, *Evidence for the* 2π *Decay of the* K_2^0 *Meson*, *Phys.Rev.Lett.* **13** (1964) 138–140.

[40] F. Halzen and A. Martin, *Quarks and Leptons*. John Wiley and Sons, 1983.

[41] Y. Nir, *CP violation in meson decays*, `arXiv:hep-ph/0510413`.

[42] I. J. R. Aitchison and A. J. G. Hey, *Gauge Theories in Particle Physics*. Adam Hilger Ltd, 1984.

[43] E. Leader and E. Predazzi, *An Introduction to Gauge Theories and New Physics*. Cambridge University Press, 1982.

[44] ATLAS Collaboration, G. Aad et al., *Search for dilepton resonances in pp collisions at $\sqrt{s} = 7\,\text{TeV}$ with the ATLAS detector*, *Phys.Rev.Lett.* **107** (2011) 272002, [arXiv:1108.1582].

[45] S.-L. Chen and N. Okada, *Flavorful Z' signatures at LHC and ILC*, *Phys.Lett.* **B669** (2008) 34–38, [arXiv:0808.0331].

[46] ARGUS Collaboration, H. Albrecht et al., *Observation of B^0 - $\bar{B}^0$ Mixing*, *Phys.Lett.* **B192** (1987) 245.

[47] DØ Collaboration, S. Abachi et al., *Observation of the top quark*, *Phys.Rev.Lett.* **74** (1995) 2632–2637, [arXiv:hep-ex/9503003].

[48] CDF Collaboration, F. Abe et al., *Observation of top quark production in $\bar{p}p$ collisions*, *Phys.Rev.Lett.* **74** (1995) 2626–2631, [arXiv:hep-ex/9503002].

[49] Particle Data Group, K. Nakamura et al., *Review of particle physics*, *J. Phys.* **G37** (2010) 075021.

[50] BABAR Collaboration, B. Aubert et al., *Study of $B^\pm \to J/\psi\pi^\pm$ and $B^\pm \to J/\psi K^\pm$ decays: Measurement of the ratio of branching fractions and search for direct CP violation*, *Phys.Rev.Lett.* **92** (2004) 241802, [arXiv:hep-ex/0401035].

[51] Belle Collaboration, V. Bhardwaj et al., *Observation of $B^\pm \to \psi(2S)\pi^\pm$ and search for direct CP-violation*, *Phys.Rev.* **D78** (2008) 051104, [arXiv:0807.2170].

[52] LHCb Collaboration, R. Aaij et al., *Observation of CP violation in $B^+ \to DK^+$ decays*, *Phys.Lett.* **B712** (2012) 203–212, [arXiv:1203.3662].

[53] M. Neubert and B. Stech, *Heavy Flavours II*. World Scientific, 1988.

[54] J. M. Soares, *More on direct CP violation in $b \to dJ/\psi$ decays*, *Phys.Rev.* **D52** (1995) 242–247, [arXiv:hep-ph/9404336].

[55] L. Wolfenstein, *Final-state interactions and CP violation in weak decays*, *Phys.Rev.* **D43** (1991) 151–156.

[56] Belle Collaboration, K. Abe et al., *Observation of the decay $B \to K\ell^+\ell^-$*, *Phys.Rev.Lett.* **88** (2002) 021801, [arXiv:hep-ex/0109026].

[57] CLEO Collaboration, M. S. Alam et al., *First Measurement of the Rate for the Inclusive Radiative Penguin Decay $b \to s\gamma$*, *Phys.Rev.Lett.* **74** (1995) 2885–2889.

[58] BABAR Collaboration, B. Aubert et al., *Direct CP, Lepton Flavor and Isospin Asymmetries in the Decays $B \to K^{(*)}\ell^+\ell^-$*, *Phys.Rev.Lett.* **102** (2009) 091803, [arXiv:0807.4119].

[59] LHCb Collaboration, R. Aaij et al., *Differential branching fraction and angular analysis of the $B^+ \to K^+\mu^+\mu^-$ decay*, arXiv:1209.4284.

[60] J.-J. Wang, R.-M. Wang, Y.-G. Xu, and Y.-D. Yang, *The Rare decays $B_u^+ \to \pi^+\ell^+\ell^-$, $\rho^+\ell^+\ell^-$ and $B_d^0 \to \ell^+\ell^-$ in the R-parity violating supersymmetry*, *Phys.Rev.* **D77** (2008) 014017, [arXiv:0711.0321].

[61] Belle Collaboration, J.-T. Wei et al., *Search for $B \to \pi\ell^+\ell^-$ Decays at Belle*, *Phys.Rev.* **D78** (2008) 011101, [arXiv:0804.3656].

[62] BABAR Collaboration, B. Aubert et al., *Search for the rare decay $B \to \pi\ell^+\ell^-$*, *Phys.Rev.Lett.* **99** (2007) 051801, [arXiv:hep-ex/0703018].

[63] T. M. Aliev and M. Savci, *Exclusive $B \to \pi\ell^+\ell^-$ and $B \to \rho\ell^+\ell^-$ decays in the two Higgs doublet model*, *Phys.Rev.* **D60** (1999) 014005.

[64] F. Kruger and E. Lunghi, *Looking for novel CP violating effects in $\bar{B} \to K^*\ell^+\ell^-$*, *Phys.Rev.* **D63** (2001) 014013, [arXiv:hep-ph/0008210].

[65] V. Bashiry and K. Zeynali, *Analysis of the $B \to \pi\ell^+\ell^-$ Decay in the Standard Model with Fourth Generation*, *JHEP* **0712** (2007) 055, [arXiv:0710.1401].

[66] Heavy Flavor Averaging Group, Y. Amhis et al., *Averages of b-hadron, c-hadron, and tau-lepton properties as of early 2012*, arXiv:1207.1158.

[67] Belle Collaboration, K. Abe et al., *Observation of $b \to d\gamma$ and determination of $|V_{td}/V_{ts}|$*, *Phys.Rev.Lett.* **96** (2006) 221601, [arXiv:hep-ex/0506079].

[68] BABAR Collaboration, P. del Amo Sanchez et al., *Study of $B \to X\gamma$ decays and determination of $|V_{td}/V_{ts}|$*, *Phys.Rev.* **D82** (2010) 051101, [arXiv:1005.4087].

[69] Lange, D. J., *The EvtGen particle decay simulation package*, *Nucl.Instrum.Meth.* **A462** (2001) 152–155.

[70] A. Ali, E. Lunghi, C. Greub, and G. Hiller, *Improved model independent analysis of semileptonic and radiative rare B decays*, *Phys.Rev.* **D66** (2002) 034002, [arXiv:hep-ph/0112300].

[71] H. Asatrian, H. Asatrian, C. Greub, and M. Walker, *Two loop virtual corrections to $B \to X_s\ell^+\ell^-$ in the standard model*, *Phys.Lett.* **B507** (2001) 162–172, [arXiv:hep-ph/0103087].

[72] C. Bobeth, M. Misiak, and J. Urban, *Photonic penguins at two loops and m_t dependence of $BR[B \to X_s\ell^+\ell^-]$*, *Nucl.Phys.* **B574** (2000) 291–330, [arXiv:hep-ph/9910220].

[73] P. Ball and R. Zwicky, *New results on $B \to \pi, K, \eta$ decay form factors from light-cone sum rules*, *Phys.Rev.* **D71** (2005) 014015, [arXiv:hep-ph/0406232].

[74] C. Bobeth, G. Hiller, and G. Piranishvili, *Theoretical Status of Rare B Decays with Muons*, *PoS* **BEAUTY2009** (2009) 047, [arXiv:0911.4054].

[75] V. Bashiry, *CP-Violation in $b \to s\ell^+\ell^-$ transition Beyond the Standard Model*, *J.Phys.* **G32** (2006) 1073–1079, [arXiv:hep-ph/0605061].

[76] Belle Collaboration, J.-T. Wei et al., *Measurement of the Differential Branching Fraction and Forward-Backword Asymmetry for $B \to K^{(*)}\ell^+\ell^-$*, *Phys.Rev.Lett.* **103** (2009) 171801, [arXiv:0904.0770].

[77] F. Kruger and L. Sehgal, *CP violation in the exclusive decays $B \to \pi e^+e^-$ and $B \to \rho e^+e^-$*, *Phys.Rev.* **D56** (1997) 5452–5465, [arXiv:hep-ph/9706247].

[78] L. Evans and P. Bryant, *LHC Machine*, *J.Instrum.* **3** (2008), no. 08 S08001.

[79] T. Taylor, *Superconducting Magnets and RF Cavities for the LHC*, CERN-LHC-Project-Report-379, 2000.

[80] LHCb Collaboration, A. A. Alves Jr et al., *The LHCb Detector at the LHC*, *J.Instrum* **3** (2008), no. 08 S08005.

[81] *LEP design report.* CERN, Geneva, 1984.

[82] S. Amato et al., *LHCb magnet: Technical Design Report.* Technical Design Report LHCb. CERN, Geneva, 2000.

[83] J. Prisciandaro, F. Blanc, and T. Nakada, *Improved magnetic field map with 2011 measurements for the LHCb dipole magnet*, CERN-LHCb-INT-2012-012, CERN, Geneva, 2012.

[84] A. Jaeger, P. Seyfert, M. De Cian, J. van Tilburg, and S. Hansmann-Menzemer, *Measurement of the track finding efficiency*, CERN-LHCb-PUB-2011-025, CERN, Geneva, 2012.

[85] S. Bachmann et al., *Ageing in the LHCb outer tracker: Phenomenon, culprit and effect of oxygen*, *Nucl.Instrum.Meth.* **A617** (2010), no. 13 202 – 205.

[86] D. Golubkov and V. Egorychev, *Electron particle identication with LHCb calorimeter system for 2011 data taking period*, LHCb-INT-2011-052, 2011.

[87] M. Ferro-Luzzi, *Proposal for an absolute luminosity determination in colliding beam experiments using vertex detection of beam-gas interactions*, *Nucl.Instrum.Meth.* **A553** (2005) 388–399. 17 p.

[88] T. Gys, *The pixel hybrid photon detectors for the LHCb-RICH project*, *Nucl.Instrum.Meth.* **A465** (2001), no. 1 240 – 246.

[89] M. Adinolfi et al., *Performance of the LHCb RICH detector at the LHC*, arXiv:1211.6759.

[90] D. Perego, *The LHCb RICH silica aerogel performance with LHC data*, *Nucl.Instrum.Meth.* **A639** (2011), no. 1 234 – 237.

[91] R. Aaij and J. Albrecht, *Muon triggers in the High Level Trigger of LHCb*, CERN-LHCb-PUB-2011-017, CERN, Geneva, 2011.

[92] R. Fruhwirth, *Application of Kalman filtering to track and vertex fitting*, *Nucl.Instrum.Meth.* **A262** (1987) 444–450.

[93] W. D. Hulsbergen, *Decay chain fitting with a Kalman filter*, *Nucl.Instrum.Meth.* **A552** (2005) 566–575, [arXiv:physics/0503191].

[94] M. Pivk and F. L. Diberder, *$_s$Plot: A statistical tool to unfold data distributions*, *Nucl.Instrum.Meth.* **A555** (2005), no. 12 356 – 369, [arXiv:physics/0402083].

[95] R. Aaij et al., *The LHCb Trigger and its Performance*, arXiv:1211.3055.

[96] T. Skwarnicki, *A study of the radiative cascade transitions between the Upsilon-prime and Upsilon resonances*. PhD thesis, Institute of Nuclear Physics, Krakow, 1986. DESY-F31-86-02.

[97] LHCb Collaboration, R. Aaij et al., *Determination of f_s/f_d for 7 TeV pp collisions and a measurement of the branching fraction of the decay $B_d \to D^- K^+$*, *Phys.Rev.Lett.* **107** (2011) 211801, [arXiv:1106.4435].

[98] BABAR Collaboration, B. Aubert et al., *Branching fraction and charge asymmetry measurements in $B \to J/\psi\,\pi\pi$ decays*, *Phys.Rev.* **D76** (2007) 031101, [arXiv:0704.1266].

[99] W. Verkerke and D. Kirkby, *The RooFit toolkit for data modeling*, in *Statistical Problems in Particle Physics, Astrophysics and Cosmology*, Imperial College Press, 2005. arXiv:physics/0306116.

[100] T. Sjostrand, S. Mrenna, and P. Z. Skands, *PYTHIA 6.4 Physics and Manual*, *JHEP* **0605** (2006) 026, [arXiv:hep-ph/0603175].

[101] GEANT4, S. Agostinelli et al., *GEANT4: A simulation toolkit*, *Nucl.Instrum.Meth.* **A506** (2003) 250–303.

[102] DØ Collaboration, V. Abazov et al., *Study of direct CP violation in $B^\pm \to J/\psi\, K^\pm(\pi^\pm)$ decays*, *Phys.Rev.Lett.* **100** (2008) 211802, [arXiv:0802.3299].

[103] LHCb Collaboration, R. Aaij et al., *First evidence of direct CP violation in charmless two-body decays of B_s^0 mesons*, *Phys.Rev.Lett.* **108** (2012) 201601, [arXiv:1202.6251].

[104] LHCb collaboration, R. Aaij et al., *Measurement of the $D_s^+ - D_s^-$ production asymmetry in 7 TeV pp collisions*, *Phys.Lett.* **B713** (2012) 186–195, [arXiv:1205.0897].

[105] A. Hoecker et al., *TMVA: Toolkit for Multivariate Data Analysis*, *PoS* **ACAT** (2007) 040, [arXiv:physics/0703039].

[106] Y. Li, *Observation of $B_c^+ \to \psi(2S)\pi^+$ decay and measurement of $\mathcal{B}(B_c^+ \to \psi(2S)\pi^+)/\mathcal{B}(B_c^+ \to J/\psi\,\pi^+)$*, CERN-LHCb-ANA-2012-101, 2012.

[107] LHCb Collaboration, R. Aaij et al., *Measurement of $\sigma(pp \to b\bar{b}X)$ at $\sqrt{s} = 7\,\text{TeV}$ in the forward region*, *Phys.Lett.* **B694** (2010) 209–216, [arXiv:1009.2731].

[108] G. Branco, L. Lavoura, and J. Silva, *CP Violation*. Oxford Science Publications, 1999.

[109] V. A. Kostelecky and N. Russell, *Data Tables for Lorentz and CPT Violation*, *Rev.Mod.Phys.* **83** (2011) 11, [arXiv:0801.0287].

[110] OPERA Collaboration, T. Adam et al., *Measurement of the neutrino velocity with the OPERA detector in the CNGS beam*, *JHEP* **1210** (2012) 093, [arXiv:1109.4897].

[111] BABAR Collaboration, J. Lees et al., *Observation of Time Reversal Violation in the B^0 Meson System*, *Phys.Rev.Lett.* **109** (2012) 211801, [arXiv:1207.5832].

[112] J. Bernabeu, F. Martinez-Vidal, and P. Villanueva-Perez, *Time Reversal Violation from the entangled $B^0 - \bar{B}^0$ system*, *JHEP* **1208** (2012) 064, [arXiv:1203.0171].